Title
Heat Generation and Degradation in Electrochemical Capacitors

Author
LIKITCHATCHAWANKUN, AMPOL

Publication Date
2020

Peer reviewed|Thesis/dissertation

UNIVERSITY OF CALIFORNIA

Los Angeles

Heat Generation and Degradation in Electrochemical Capacitors

A dissertation submitted in partial satisfaction
of the requirements for the degree
Doctor of Philosophy in Mechanical Engineering

by

Ampol Likitchatchawankun

2020

ABSTRACT OF THE DISSERTATION

Heat Generation and Degradation in Electrochemical Capacitors

by

Ampol Likitchatchawankun
Doctor of Philosophy in Mechanical Engineering
University of California, Los Angeles, 2020
Professor Laurent G. Pilon, Chair

Electrochemical capacitors (ECs) have drawn significant attention as electrical energy storage systems for high power applications thanks to their high cycle efficiency and long cycle life. However, under high current cycling, they can experience a significant amount of heat generation resulting in excessively high cell temperatures. Elevated temperatures, in turn, can lead to (i) increased self-discharge rates, (ii) accelerated aging of the device, and (iii) electrolyte decomposition and evaporation causing deterioration of their performance and lifetime. In this context, ionic liquid (IL) electrolytes are promising due to their excellent thermal stability over large operating temperature windows. However, most recent calorimetric studies have measured irreversible and reversible heat generation rates in electric double layer capacitors (EDLCs) consisting of activated carbon (AC) electrodes with organic and aqueous electrolytes at room temperature. This doctoral thesis investigates experimentally the heat generation rate in AC electrodes with ILs neat or diluted in an organic solvent electrolytes in the temperature range between 5 and 80 °C. First, a potential window of 1 V was used to compare with past calorimetric studies using aqueous or organic electrolytes. Then a more realistic potential window of 2.5 V was tested for the same temperature range. Endothermic dips were observed in the instantaneous heat generation rate at the negative electrode in diluted IL and grew with increasing temperature due to overscreening

effects, ion desolvation, and/or decomposition of PC. The irreversible heat generation was similar in each half-cell and decreased with increasing temperature due to the increase in the electrolyte conductivity with temperature. The total irreversible heat generation was in good agreement with Joule heating for potential window of 1 V, as also observed with aqueous and organic electrolytes. However, the total irreversible heat generation exceeded Joule heating for potential window of 2.5 V, especially at high temperature and low current. This was attributed to ion desorption and charge redistribution in the porous electrodes. Finally, the reversible heat generation increased with temperature and was larger at the positive than at the negative electrode due to the difference in anion and cation sizes.

Moreover, elevated temperatures associated with high heat generation rates are very concerning for flexible and wearable all-solid-state supercapacitors with gel electrolytes placed in direct contact with the users. Therefore, quantifying the amount of heat generation in such devices is essential for developing thermal management strategy in order to ensure user's comfort and safety. This thesis also investigates heat generation in flexible all-solid-state supercapacitor devices consisting of graphene petals grown on buckypaper electrodes with either conventional (non-redox) or redox-active gel electrolyte. The total irreversible heat generation was equal to Joule heating for both types of devices but was larger in the device with redox-active gel electrolyte due to its larger internal resistance. In addition, the reversible heat generation rate was different at the positive and negative electrodes in each device due to asymmetry in the charging mechanisms caused by a combination of electric double layer (EDL) formation, overscreening effect, and additional redox reactions in the redox-active gel electrolyte. This study further illustrates how *in operando* calorimetry can not only quantify the heat generation rate necessary to device thermal management but also provide insights into the electrochemical phenomena occurring during cycling of ECs.

The dissertation of Ampol Likitchatchawankun is approved.

Adrienne S. Lavine

Bruce S. Dunn

Timothy S. Fisher

Laurent G. Pilon, Committee Chair

University of California, Los Angeles

2020

This dissertation is dedicated to my beloved family.

TABLE OF CONTENT

LIST OF SYMBOLS

a	Effective ion diameter, nm
A	Footprint area of the heat flux sensor, cm^2
c_p	Specific heat, J/(kg·°C)
C_{diff}	Differential capacitance, mF
$C_{diff,m}$	Gravimetric differential capacitance, F/g
C_{int}	Integral capacitance, mF
$C_{int,m}$	Gravimetric Integral capacitance, F/g
D	Diffusion coefficient of ions in electrolyte, m^2/s
e	Elementary charge, $e = 1.602 \times 10^{-19}$ C
f	Frequency, Hz
F	Faraday's constant, $F = eN_A = 9.648 \times 10^4$ C/mol
i	Current density, mA/cm^2
I	Current, mA
k	Thermal conductivity, W/(m·°C)
L	Electrode length, cm
m	Mass loading of active material in electrode, mg
n_c	Cycle number, -
q''	Heat flux, mW/cm^2
$\dot{q}$	Volumetric heat generation rate, mW/cm^3
$\dot{Q}$	Heat generation rate, mW
$\bar{\dot{Q}}$	Time-averaged heat generation rate, mW
R_i	Electric resistance of resistor or electrode "i", Ω
R_s	Internal resistance for entire EC device, Ω or Ω m^2
S	Entropy of the system, J/K
S_i	Heat flux sensor sensitivity at electrode "i", $\mu V/(mW/cm^2)$
S_o	Heat flux sensor sensitivity at 22.5 °C, $\mu V/(mW/cm^2)$

S_c	Heat flux correction factor , μV/[°C $\cdot$(mW/cm^2)]
t	Time, s
t_c^-	Time immediately after the beginning of the discharging step, s
t_c^+	Time at the end of the charging step, s
t_{cd}	Charging-discharging cycle period, s
Δt	Time step (data acquisition time), s
T_c	Cold plate temperature, °C
T_o	Operating temperature, °C
W	Electrode width, cm
ΔV	Voltage difference generated in the heat flux sensor, μV
z	Ion valency, -

Greek symbols

ϵ_0	Vacuum permittivity, F/m
ϵ_r	Dielectric constant of the electrolyte, -
ν	Scan rate, mV/s
σ	Electrical conductivity, mS/cm
$\psi_{s,max}$	Maximum cell potential, V
$\psi_{s,min}$	Minimum cell potential, V
$\psi_s(t)$	Cell potential, V
$\Delta\psi_{eq}$	Equilibrium potential difference, V

Superscripts

c	Refers to charging step

Subscripts

AC	Refers to activated carbon electrode
A or B	Refers to heat flux sensor A or B
c	Refers to charging step
cd	Refers to charging-discharging cycle
C	Refers to the capacitive component

d	Refers to discharging step
dc	Refers to the time-independent DC component
i	Refers to ion species "i"
irr	Refers to irreversible processes
J	Refers to Joule heating
T	Refers to entire cell
rev	Refers to reversible process
$+$ or $-$	Refers to positive or negative electrode

LIST OF FIGURES

LIST OF TABLES

ACKNOWLEDGMENTS

Firstly, I would like to express my sincere gratitude to my advisor, Professor Laurent Pilon, for the continuous support of my Ph.D study and related research works, for his patience, motivation, and immense knowledge. His guidance and encouragement helped me in all the time of research and writing of this thesis. Besides my advisor, I would like to thank the rest of my thesis committee: Professor Bruce Dunn, Professor Timothy Fisher, and Professor Adrienne Lavine, for their insightful comments and encouragement from various perspectives. Furthermore, I would like to express my appreciation to my collaborators Jonathan Lau, Ryan DeBlock, and Grace Whang from Professor Dunn's lab as well as Arpan Kundu from Professor Fisher's lab for providing electrode and electrolyte materials for my research works. I thank my fellow labmates Obaidallah Munteshari, Sun Woong Baek, and Matevž Frajnkovič for their help with the experimental work and the stimulating discussions. I would also like to acknowledge all other lab members Dr. Michal Marszewski, Eylul Simsek, Ali Dashti, Sara Vallejo, Tiphaine Galy, Yucheng Zhou, and Jack Hoeniges. I am also grateful to all my friends who have made my life enjoyable during my study at UCLA. Last but not the least, I would like to thank my family for supporting me spiritually throughout writing this thesis and my life in general.

VITA

2006–2012	Dipl.-Ing Univ. Mechanical Engineering, Technische Universität München, Germany.
2016–present	PhD Student, Mechanical and Aerospace Engineering Department, UCLA.

PUBLICATIONS

A. Likitchatchawankun, A. Kundu, O. Munteshari, T. S. Fisher, L. Pilon, 2019, Heat generation in all-solid-state supercapacitors with graphene electrodes and gel electrolytes, Electrochimica Acta, vol. 303, pp. 341-353.

O. Munteshari, J. Lau, **A. Likitchatchawankun**, B.-A. Mei, C. S. Choi, D. Butts, B. Dunn, L. Pilon, 2019, Thermal signature of ion intercalation and surface redox reactions mechanisms in model pseudocapacitive electrodes, Electrochimica Acta, vol. 307, pp. 512-524.

A. Likitchatchawankun, G. Whang, J. Lau, O. Munteshari, B. Dunn, L. Pilon, 2020, Effect of temperature on irreversible and reversible heat generation rates in ionic liquid-based electric double layer capacitors, Electrochimica Acta, vol. 338, pp. 135802.

O. Munteshari, A. Borenstein, R. H. DeBlock, J. Lau, G. Whang, Y. Zhou, **A. Likitchatchawankun**, R. B. Kaner, B. Dunn, L. Pilon, 2020, In operando calori-

metric measurements for activated carbon electrodes in ionic liquid electrolytes under large potential windows, ChemSusChem, vol. 13, pp. 1-15.

A. Likitchatchawankun, R. H. DeBlock, G. Whang, O. Munteshari, M. Frajnkovič, B. S. Dunn, L. Pilon, 2020, Irreversible and reversible heat generation rates in EDLCs with neat and diluted ionic liquid electrolytes under large potential window between 5 and 80 °C, Journal of Power Sources, (under review).

CHAPTER 1

Introduction

1.1 Introduction

Electrochemical capacitors (ECs), also known as supercapacitors and ultracapacitors, have drawn significant attention as electrical energy storage systems thanks to their large power densities, high cycle efficiency, and long cycle life compared with batteries [1, 2]. They are promising for many applications requiring charging/discharging at high rate such as the electricity grid, factory power backup, and regenerative braking in electric vehicles [3–9]. ECs can be generally divided into three categories (i) electric double layer capacitors (EDLCs) storing charge physically in the electric double layer (EDL) forming at the interface of porous carbon electrodes and the electrolyte; (ii) electrochemical pseudocapacitors storing charge in the EDL and in fast and reversible redox reactions in metal oxides or conducting polymer electrodes; and (iii) hybrid-pseudocapacitors combining one carbon-based electrode and one pseudocapacitive electrode [10, 11]. In fact, pseudocapacitive electrode can be used either as positive or negative electrode when pairing with carbon-based electrode [12, 13].

Moreover, in recent years, the demand for portable consumer electronics and wearable devices has stimulated the need for lightweight, flexible, and reliable energy storage devices [14–17]. In this regard, all-solid-state supercapacitors are promising owing to their favorable properties such as low weight, manufacturing simplicity, and high power density [18–20]. All-solid-state supercapacitors are generally fabricated by sandwiching a piece of flexible gel electrolyte film between two flexible electrodes composed of carbon-based materials [21–23].

1.1.1 Electrode materials for electrochemical capacitors

EDLCs consist typically of two carbon-based electrodes and a separator immersed in concentrated aqueous, organic, or ionic liquid electrolytes [24–26]. The most common electrode material for EDLCs is activated carbon (AC) as it is readily available, inexpensive, and environmentally friendly [24–26]. In addition, AC offers large surface area and pore with optimum size accessible to ions in the electrolyte to maximize charge storage [24–26]. Carbon nanotubes (CNTs) have also been investigated as electrode materials for supercapacitors but it has not been commercialized due to theirs high cost [27, 28]. Furthermore, graphene has attracted great interest for flexible EDLC electrode due to its high specific surface area and electronic conductivity as well as its good mechanical strength and flexibility [27, 28].

Unlike in battery materials, redox reactions in pseudocapactive electrodes are fast, highly reversible, and exhibit no phase transformation under galvanostatic cycling [1]. Transition metal oxides such as MnO_2, MoO_2, Nb_2O_5, V_2O_5, and Fe_3O_4 [12, 13, 29–32] and conductive polymers including polyaniline (PANI) and polypyrrole (PPy) [33–36] have been considered as pseudocapacitive electrode materials due to their high theoretical capacity, high redox reaction reversibility, and chemical stability.

1.1.2 Electrolytes for electrochemical capacitors

Besides the electrode materials, electrolyte is a major component of ECs as physicochemical phenomena occur mainly at or near the electrode/electrolyte interface [10, 11]. Electrolytes consists of a salt dissolved in a solvent providing ionic conductivity and facilitating charge compensation at each electrode of the cell [10, 11]. In general, electrolytes for ECs are mainly classified as (1) liquid electrolytes and (2) solid/quasi-solid-state electrolytes, and (3) redox-active elec-

trolytes [10, 11].

First, liquid electrolytes include (i) aqueous electrolytes, (ii) organic electrolytes, and (iii) ionic liquids in neat form or mixed with an organic solvent [10, 11]. Aqueous electrolytes include strong acids or bases or neutral salt dissolved in water such as sulfuric acid H_2SO_4, potassium hydroxide KOH, or sodium sulfate Na_2SO_4. They typically are inexpensive, easy to prepare, and exhibit high ionic conductivity ($\sim$ 800 mS/cm for 1 M H_2SO_4 at 25 °C [10]). Their use in EDLCs results in large capacitance but relatively low energy density due to their narrow operating cell voltage windows ($\sim$ 1 V) [10, 11, 37]. Organic electrolytes have been used for their large operating potential window $\Delta\psi_s$ reaching up to 3 V. Indeed, the energy density E (in J/m^2) of ECs can be expressed as [1],

$$E = \frac{1}{2} C \ \Delta\psi_s^2 \tag{1.1}$$

where C is the specific capacitance of the cell (in F/m^2) and $\Delta\psi_s$ is the potential window (in V). Organic electrolytes include tetraethylammonium tetrafluoroborate ($TEABF_4$) salt disolved in organic solvent such as propylene carbonate (PC) or acetonitrile (ACN). However, ECs using organic electrolytes usually have a higher cost, a lower ionic conductivity (15 mS/cm or 60 mS/cm for 1 M $TEABF_4$ in PC or ACN, respectively, at 25 °C [38]), a smaller specific capacitance, and raise several safety concerns including toxicity, volatility, and flammability [10, 11, 37]. Alternatively, neat ionic liquids (ILs) offer a larger operating potential window than organic electrolytes up to 4 V [39]. Ionic liquids include N-butyl-N-methyl-pyrrolidinium bis(trifluoromethane sulfonyl)imide ($Pyr_{14}TFSI$) or 1-ethyl-3-methylimidazolium tetrafluoroborate ($EMIMBF_4$) [10, 11]. However, they have a much lower ionic conductivity ($\sim$ 2.0 mS/cm for neat $Pyr_{14}TFSI$ at 20 °C [40,41]) and higher viscosity than aqueous or organic electrolytes [10,39]. Nevertheless, their ionic conductivity increases while their viscosity decreases strongly

with increasing temperature [42–46]. Another way to increase the ionic conductivity of ILs is to dilute them in (i) carbonate-based organic solvents such as propylene carbonate (PC) or a mixture of ethylene carbonate (EC) and dimethyl carbonate (DMC) as well as in (ii) nitrile-based solvent such as acetonitrile (ACN) [42,47,48]. The increase in ionic conductivity and the associated decrease in viscosity in diluted ILs are due to the reduction in ion pairing via solvation [48]. However, diluted ILs tend to be less electrochemically and thermally stable than their neat IL counterpart [48]. In addition, despite the wide theoretical potential window of ILs, they may react with the carbonaceous electrode surface as a result of catalytic activity [49, 50]. Moreover, elevated temperature can shorten the operating potential window due to solvent decomposition [51]. Furthermore, ILs also have similar safety concerns as organic electrolytes requiring sophisticated purification procedures under a well-controlled atmosphere, such as in a glove box, to avoid exposure to moisture and oxygen [10, 11].

Second, ECs with solid-state electrolytes do not suffer from electrolyte leakage and can be assembled without using rigid closed containers [10, 11]. For these reasons, all-solid-state ECs are promising for lightweight, portable, flexible, and wearable energy storage devices [14–17]. However, they suffer from low ionic conductivity due to the fact that the ions mobility is much smaller in solid-state gels than in liquid electrolytes [10, 11]. Solid/quasi-solid-state electrolytes can be found in (i) dry solid state polymer such as LiCl salt in polyethylene oxide (PEO) without any solvents, (ii) gel polymers such as H_2SO_4+H_2O in polyvinyl alcohol (PVA) host polymer, and (iii) inorganic electrolytes such as Li_2S-P_2S_5 glass-ceramic electrolyte [10, 11]. Inorganic solid-state electrolytes are generally not bendable nor flexible but they are thermally stable and mechanically robust [10, 11].

Finally, redox-active electrolytes consist of redox-active species dissolved in a solvent [52]. They can exist as (i) aqueous or (ii) organic electrolytes, (iii)

ionic liquids, and (iv) gel electrolytes [10, 11]. The most common redox-active species include potassium iodide (KI) [53,54], potassium ferricyanide ($K_3Fe(CN)_6$) [55, 56], sodium molybdate (Na_2MoO_4) [57], 1-ethyl-3-methylimidazolium iodide (EMIMI) [10], and hydroquinone [58, 59], to name a few. Ion species present in these electrolytes undergo oxidation and reduction at the positive and negative electrodes during charging, thus producing pseudocapacitance and increasing capacitance [53, 55, 60]. For example, capacitance was reported to increase by 74% upon addition of KI [53] and by 212% with $K_3Fe(CN)_6$ [55] added to KOH in PVA gel electrolyte in supercapacitors with activated carbon electrodes. In general, reversible redox reactions occurring in the electrolyte may be exothermic or endothermic. In the specific case of ferricyanide/ferrocyanide redox pair, the redox reaction can be expressed as

$$Fe(CN)_6^{3-} + e^- \overset{reduction}{\underset{oxidation}{\rightleftharpoons}} Fe(CN)_6^{4-}. \tag{1.2}$$

Here, the reduction reaction is exothermic while the oxidation is endothermic [61].

1.2 Thermal considerations for electrochemical capacitors

1.2.1 Effect of temperature on electrochemical capacitors

Numerous studies have investigated the effect of temperature on the performance of ECs with various electrolytes [51, 62–74]. Electrochemical measurement methods such as galvanostatic charge-discharge cycling (GCD), cyclic voltammetry (CV), and electrochemical impedance spectroscopy (EIS) were performed within the temperature range of -40 to 100 °C on (i) test cells in three-electrode setup [70] and two-electrode cells [62,65,67,74] and on (ii) commercial EC devices and module [51, 62, 63, 66, 68, 69]. The specific capacitance was found to increase with increasing temperature as a result of increasing ion mobility [62,65,69,70,75]. For

the same reason, the cell internal resistance R_s decreased with increasing temperature in organic [63,65,69] as well as in ILs [62,76] electrolytes. However, increasing the operating temperature can have a negative effect on the self-discharge rate of ECs [77–79]. In fact, at high temperatures, ions feature higher desorption rates leading to device self-discharge [63,74,80]. Moreover, high operating temperatures and/or high applied voltages can lead to accelerated aging of ECs due to thermal and electrochemical degradation of the electrolyte and/or of the electrode materials [51,64,81]. First, for temperatures larger than the onset of decomposition temperature, electrolytes may decompose to produce gases such as carbon monoxide (CO), hydrogen (H_2), and other organic byproducts, as previously discussed [81]. These gases can lead to pressure rise inside the cell leading potentially to explosions [82]. The gases generated can also block access to the pores in the electrodes to the liquid electrolyte, leading to an increase in cell resistance and a decrease in the device capacitance [51, 81]. High temperatures can also accelerate decomposition reactions in the electrolyte and/or in the electrode by oxidation/reduction reactions producing solid byproducts [83]. These byproducts can attach onto the electrode/electrolyte interface thus reducing the electrode active surface area [83].

1.2.2 Heat generation of electrochemical capacitors

Electrochemical capacitors do not perform at 100% cycle efficiency, the difference between the electrical energy necessary to charging and that recovered during discharging is lost in the form of heat [5]. The instantaneous heat generation rate $\dot{Q}_i(t)$ in each electrode can be decomposed as the sum of the irreversible $\dot{Q}_{irr,i}(t)$ and reversible $\dot{Q}_{rev,i}(t)$ heat generation rates, i.e., $\dot{Q}_i(t) = \dot{Q}_{rev,i}(t) + \dot{Q}_{irr,i}(t)$ [87, 88]. Here, subscript "i" refers to either the positive "+" or negative "−" electrode [87, 88]. The irreversible heat generation is always positive and cannot be recovered over a charging-discharging cycle [84, 85]. By contrast, reversible heat generation can be either positive or negative depending on its charg-

ing mechanism in either charging or discharging step [84, 85]. Both irreversible and reversible heat generation rates cannot be identified by conventional electrochemical analysis but they can be quantified using calorimetric methods [86, 87]. Finally, the total instantaneous heat generation rate in the entire full-cell device $\dot{Q}_T(t)$ can be written as the sum of the heat generation rates in the positive $\dot{Q}_+(t)$ and negative $\dot{Q}_-(t)$ half-cells, i.e., $\dot{Q}_T(t) = \dot{Q}_+(t) + \dot{Q}_-(t)$ [87, 88].

Irreversible heat generation

Irreversible heat generation in EDLCs has been attributed mainly to Joule heating resulting from the charge transport across the resistive paths of the carbon particles network in the porous electrode and the liquid electrolyte confined in it [77, 86]. The heat generation rate associated with Joule heating can be expressed as $\dot{Q}_J(t) = R_s I^2$ where R_s is the internal resistance of the device and I is the imposed current. The internal resistance R_s of the device can be obtained from the IR-drop in galvanostatic charge-discharge cycling (GCD) or from electrochemical impedance spectroscopy (EIS) [87, 89]. Furthermore, Joule heating can be quantified by directly measuring irreversible heat generation rate of the device using an *in operando* calorimeter. In fact, the total irreversible heat generation rate was equal to Joule heating, obtained from $\bar{\dot{Q}}_J = R_s I^2$, for AC-based EDLC with aqueous and organic electrolytes operating at potential window $\Delta\psi_s \leq 1$ V [87, 88]. However, for AC-based EDLC with IL-based electrolytes operating at potential window $\Delta\psi_s \geq 1$, the total irreversible heat generation rate exceeded Joule heating [90].

By contrast, for pseudocapacitive electrodes, the irreversible heat generation rate was numerically found to exceed Joule heating due to (i) irreversible Faradaic heat generation (polarization heating) and (ii) hysteretic EDL formation [1, 84]. The irreversible Faradaic heat generation is defined as the product of current I and overpotential η [84]. Moreover, redox reactions at the pseudocapacitive

electrode surface compete with EDL formation resulting in hysteresis in the ion concentrations during charging and discharging. Therefore, the time-averaged heat generation associated with EDL formation over a cycle did not yield zero (i.e., reversible) but strictly positive (i.e., irreversible) [84]. This was confirmed experimentally in hybrid-pseudocapacitors consisting of a AC-based electrode and a pseudocapacitive electrode of either molybdenum dioxide (MoO_2) nanoparticles on reduced graphene oxide (rGO) or manganese oxide (MnO_2) nanoparticles on graphene (G) in organic or aqueous electrolytes [91]. In all cases, the irreversible heat generation rate at the AC electrode was proportional to I^2 and attributed to Joule heating, similar to those in EDLCs. However, the total irreversible heat generation rates measured in the pseudocapacitive electrodes exceeded Joule heating due to irreversible heat generation associated with redox reactions, polarization heating, and hysteresis in EDL formation/dissolution [91].

Reversible heat generation

Reversible heat generation can be attributed to reversible processes such as ion diffusion, steric effects, ion desolvation, entropy of mixing in EDLC electrodes, and reversible redox reactions in pseudocapacitive electrodes [92]. Indeed, upon charging, ions migrate to the electrode in the direction of decreasing electric potential energy to form the EDLs and thus released thermal energy [92]. Upon discharging, the ions diffuse to the bulk electrolyte driven by ion concentration gradient and steric repulsion in the direction of increasing electric potential energy and thermal energy was absorbed [92]. Furthermore, ion motion during charging or discharging affects also the entropy in the electrolyte domain for both EDLC and pseudocapacitive electrodes, as illustrated in Figure 1.1. During ion adsorption, ions migrate to the electrode/electrolyte interface to form the electric double layer. Then, the electrolyte system containing ions changes from a disordered to an ordered state and must lower its entropy S (i.e., $\mathrm{d}S/\mathrm{d}t < 0$). Under the

isothermal conditions imposed by the calorimeter, the heat generation rate can be expressed as $\dot{Q}_{rev} = T\mathrm{d}S/\mathrm{d}t$. Thus, ion adsorption is an exothermic process, i.e., $\dot{Q}_{rev} < 0$. By contrast, during ion desorption, ions redisperse into the bulk electrolyte such that the electrolyte system increases its entropy (i.e., $\mathrm{d}S/\mathrm{d}t > 0$) by absorbing thermal energy. Therefore, ion desorption is an endothermic process, i.e., with $\dot{Q}_{rev} > 0$. In addition, the reversible heat generation rate was directly proportional to the imposed current [77].

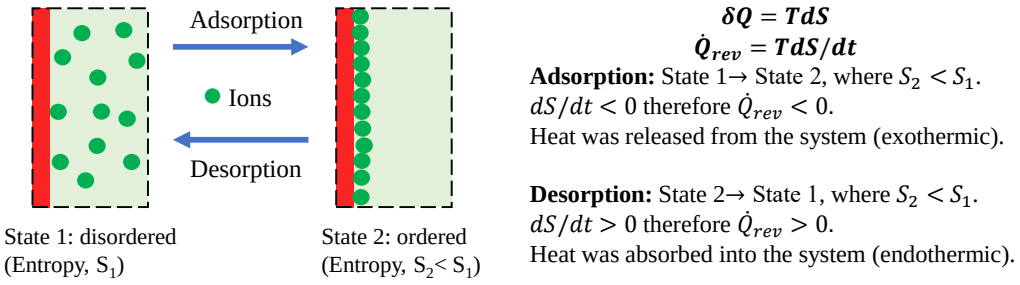

Figure 1.1: Schematic of the change of ions in an electrolyte between disordered and ordered states and the corresponding change in entropy during adsorption and desorption of ions.

1.3 Motivation of the present study

As previously mentioned, electrochemical capacitors (ECs) serve as promising electrical energy storage systems for high power applications [1]. However, under high current cycling, they can experience a significant amount of heat generation leading to excessively high temperature in the device [5, 6, 77, 78]. Elevated temperatures, in turn, can cause (i) increased self-discharge rates, (ii) accelerated aging of the device, and (iii) electrolyte decomposition and evaporation resulting in deterioration of their lifetime and performance [5, 6, 63, 64, 77–79]. In addition, the operating temperature and the cell degradation can affect charging mechanisms and therefore the associated heat generation. In this context, ionic liquid (IL) electrolytes are promising due to their excellent thermal and electrochemical

stabilities over a large operating temperature window and under large potential window. However, most recent calorimetric studies have measured irreversible and reversible heat generation rates in electric double layer capacitors (EDLCs) consisting of activated carbon (AC) electrodes with organic and aqueous electrolytes at room temperature.

Furthermore, many new electrode materials and electrolytes have been developed to achieve higher capacitance and to operate at large potential window without considering the thermal consequences of such improved performance on the device. This is even more concerning when considering comfort and safety of flexible and wearable all-solid-state supercapacitors with gel electrolytes in direct contact with the users. Understanding and quantifying the contributing phenomena to heat generation in EDLCs and pseudocapacitors are essential in order to predict the temperature evolution in those devices and to develop thermal management strategies. Moreover, calorimetric measurements can provide insights into the electrochemical phenomena occurring in the ECs during cycling [87, 88].

1.4 Objectives of the present study

The present study aims to investigate the effect of temperature and potential window on the heat generation and the associated electrochemical phenomena occurring in EDLCs consisting of AC electrodes with IL-based electrolytes for a temperature range between 5 and 80 °C using *in operando* calorimetry technique in addition to conventional electrochemical analysis.

Furthermore, quantifying heat generation and predicting temperature rise in flexible and wearable all-solid-state supercapacitors with gel electrolytes is of utmost importance for thermal management strategy in order to guarantee user's safety and comfort. The study also aims to investigate heat generation in flexible all-solid-state supercapacitor devices consisting of graphene petals grown on

buckypaper electrodes with either conventional non-redox or with redox-active gel electrolyte to assess the effect of electrolyte composition in gel electrolytes using an *in operando* isothermal calorimeter.

The study also aims to identify the thermal signatures of electrochemical phenomena occurring in EC devices during cycling for different electrode materials, electrolytes and under the various operating temperatures and potential windows considered in the previously mentioned applications. To do so, the instantaneous heat generation rate was measured in each individual electrode using a recently developed *in operando* isothermal calorimeter. The heat generation rate at each electrode was analyzed in term of irreversible and reversible heat generation rates.

1.5 Organization of the document

Chapter 2 provides background information relevant to this PhD thesis including (i) existing thermal models and (ii) previous experimental heat generation measurements in EDLCs and hybrid pseudocapacitors. Chapter 3 assesses the effect of temperature on irreversible and reversible heat generation rates in ionic liquid-based EDLCs under potential window of 1 V so as to compare the thermal signatures to those in EDLCs with aqueous and organic electrolytes at room temperature. Chapter 4 extends the previous investigation in Chapter 3 to a larger potential window of 2.5 V and investigates the effect of temperature ranging from 5 to 80 °C on the heat generation and the associated electrochemical phenomena occurring in IL-based EDLCs including comparing its thermal signatures between neat and diluted ionic liquid electrolytes in EDLCs. Chapter 5 investigates the instantaneous heat generation rate in all-solid-state supercapacitors using graphene petals grown on buckypaper electrodes and either non-redox gel or redox-active gel electrolytes, considered for flexible and wearable energy storage devices. Finally, Chapter 6 summarizes the finding of this PhD thesis and

provides recommendations for future research.

CHAPTER 2

Background

This chapter summarizes useful information and findings from the literature concerning (i) thermal models developed to account for transport and interfacial phenomena in ECs and (ii) experimental measurements of heat generation in ECs with different electrolytes and electrode compositions.

2.1 Thermal models of electrochemical capacitors

2.1.1 EDLCs

Several thermal models have been proposed in the literature to predict the temperature evolution in EDLCs using numerical or analytical methods [6, 77–79, 84–86, 93]. Many of these models solved the transient energy conservation equation with heat generation accounting only for Joule heating [6, 78, 79]. By contrast, Schiffer et al. [77] developed a thermal model for EDLCs including irreversible Joule heating and reversible heat generation due to changes in entropy of the electrolyte during EDL formation at the electrode/electrolyte interface (entropy of mixing).

More recently, d'Entremont and Pilon [93] developed a first-order time-dependent thermal model for EDLCs based on the lumped-capacitance approximation and accounting for both irreversible Joule heating and reversible heat generation rates. The latter was also modeled as linearly proportional to the imposed current during galvanostatic cycling [93]. The temporal temperature evolution predicted was in good agreement with experimental data acquired from commercial EDLCs and reported in the literature [77–79]. Furthermore, the same authors developed a

more refined physical model based on first principles by coupling (i) the modified Poisson-Nernst-Planck (MPNP) model with (ii) the energy conservation equation to derive expressions for both the irreversible and reversible heat generation rates in EDLCs with symmetric [84] or asymmetric [85] binary electrolytes for different ion diameters and diffusion coefficients. The two main contributions of heat generation rate in EDLCs arise from (i) ions decreasing their electrical potential energy and (ii) ion transport towards states of smaller entropy (heat of mixing) [85]. The former can be decomposed into three different contributions namely Joule heating, ion diffusion, and steric repulsion [85]. In addition, the heat of mixing arises from concentration and temperature gradients [85]. In all cases, the source of irreversible heat generation was exclusively Joule heating [84, 85]. In addition, larger ion concentrations, diffusion coefficients and/or ion valencies led to smaller irreversible heat generation rate due to an increase in electrolyte electrical conductivity [85]. On the other hand, the instantaneous reversible heat generation was attributed to ion diffusion, steric effects, and entropy changes during charging and discharging [84, 85]. It was found to be exothermic during charging and endothermic during discharging [84, 85]. For binary asymmetric electrolytes, the reversible heat generation rate was different at the positive and negative electrodes [85]. In fact, the reversible heat generation rate at a given electrode increased with increasing valency and decreasing diameter of the counterion but was independent of ion diffusion coefficients [85].

2.1.2 Hybrid pseudocapacitors

D'Entremont and Pilon [92] extended their thermal model of EDLCs to hybrid pseudocapacitor devices. These devices consisted of (i) a carbon-based negative electrode and (ii) a pseudocapacitive positive electrode in an electrolyte domain modeled as 1 M lithium perchlorate ($LiClO_4$) in propylene carbonate (PC) [92]. The authors assumed (i) reversible reaction of Li^+ cations with pseudocapaci-

tive electrode within the Stern layer and (ii) intercalation of Li^+ cations in the electrode caused by a diffusion process [92]. During charging of pseudocapacitive electrode, two main regimes were identified namely (i) Faradaic regime, where redox reactions dominate at low current densities and (ii) capacitive regime, where EDL formation dominates at high current densities [92]. The total irreversible heat generation at the pseudocapacitive electrode was mainly contributed to (i) Joule heating, (ii) irreversible Faradaic heat generation (also called polarization heating), and (iii) irreversible heat generation caused by hysteretic EDL formation [92]. By contrast, the total irreversible heat generation at the carbon-based electrode was due to Joule heating only [92]. In the Faradaic regime, the total irreversible heat generation rate exceeded Joule heating due to the much larger irreversible heat generation rates associated with Faradaic redox reaction and EDL formation and it was proportional to the square of imposed current density i [92]. By contrast, in the capacitive regime, Joule heating dominated and the total irreversible heat generation rate was also proportional to i^2 [92]. Finally, at the pseudocapacitive electrode, the predicted reversible heat generation rate was endothermic during charging by deintercalation while it was exothermic during discharging by intercalation in Faradaic regime [92]. By contrast, in the capacitive regime, the heat generation rate featured both endothermic and exothermic during the charging as well as discharging steps [92]. In addition, at the carbon-based electrode, the predicted reversible heat generation rate was strictly exothermic during charging and endothermic during discharging [92].

2.2 Calorimetry measurements

2.2.1 Apparatus and methods

Few experimental studies have investigated heat generation in ECs [86–88, 91]. Dandeville et al. [86] developed an electrochemical calorimeter to measure time-

dependent temperature profile of (i) an EDLC device consisting of two identical activated carbon electrodes and (ii) a hybrid pseudocapacitor device consisting of one activated carbon (AC) negative electrode and one MnO_2 positive electrode using thermocouples [86]. Both devices were assembled in 0.5 M K_2SO_4 aqueous electrolyte and cycled under galvanostatic cycling [86]. In addition, the total instantaneous heat generation in each device was calculated by deconvoluting the measured time-dependent cell temperature during cycling [86]. In the EDLC device, the instantaneous heat generation rate at each AC electrode half cell was assumed to be identical and equal to half of the total heat generation rate of the entire device [86]. Furthermore, the instantaneous heat generation was decomposed into (i) irreversible heat generation caused by Joule heating and (ii) reversible heat generation. Subsequently, the instantaneous heat generation rate of the MnO_2 electrode half cell was estimated by subtracting that of one AC electrode half cell from the total heat generation rate of the entire hybrid pseudocapacitor device [86].

More recently, Munteshari et al. [87, 91] developed an *in operando* isothermal calorimeter to measure the time-dependent irreversible and reversible heat generation rates in hybrid pseudocapacitors at each electrode separately using two thermoelectric heat flux sensors. Figure 2.1 shows schematic of the experimental setup consisting of (i) two thermoelectric heat flux sensors (gSKIN-XP, greenTEG) connected to (ii) a data acquisition (DAQ) system (34972A LXI, Keysight Technology), (iii) two identical instrumented cold plates fed with deionized water as circulating coolant (Dynalene HC-50, Dynalene Inc.) from (iv) a temperature-controlled chiller (Polystat, Cole-Parmer), (v) two flow meters (FLR-1012, Omega), and (vi) an electrochemical test section containing a two-electrode cell immersed in an electrolyte and connected to (vii) a potentiostat/galvanostat (SP 150, Bio-Logic Science Instruments) [87].

Figure 2.2 shows (a) an exploded view of the apparatus, (b) an enlarged view

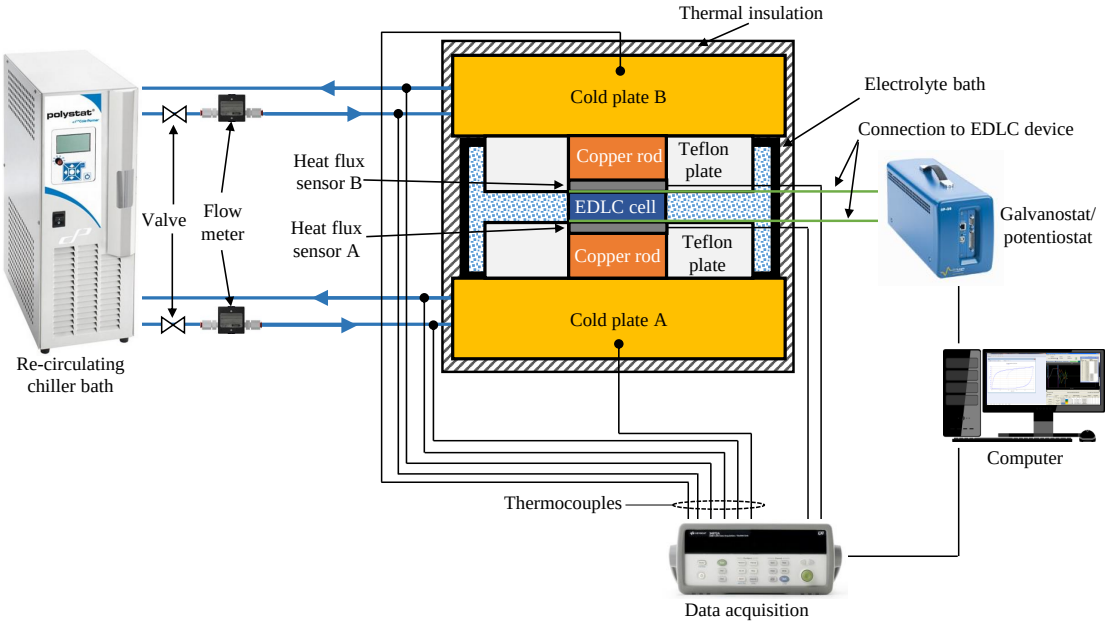

Figure 2.1: Schematic of an *in operando* calorimeter apparatus designed and fabricated in the present study to measure heat generation rate in EDLCs.

of the sensing area, (c) photograph of an activated carbon electrode with 1×1 cm^2 footprint area supported by a 316 stainless steel current collector, and (d) a cross-sectional view of a heat flux sensor plate with the corresponding dimensions [87]. The *in operando* isothermal calorimeter consisted of two heat flux sensor plates and a cylindrical container made of polytetrafluoroethylene (PTFE). Here, PTFE or so-called Teflon provides several benefits including (i) chemical resistance to strong acidic and basic electrolytes, (ii) low thermal conductivity of 0.25 W/(m·K), and (iii) mechanical and thermal stabilities over a wide range of temperature (i.e., -200 °C to 260 °C) [87]. Each heat flux sensor plate consisted of (i) 10×10 mm^2 thermoelectric heat flux sensor (gSKIN-XP, greenTEG) with the thickness of 0.5 mm in thermal contact with (ii) a cylindrical copper rod, 15.9 mm in diameter and 19.5 mm in length, embedded in the center of (iii) a PTFE disc and flush with its surfaces. The diameter and thickness of the PTFE disc were 85 mm and 20 mm, respectively [87]. The copper rod was used to conduct the heat generated in the electrode through the heat flux sensor to the cold plate, maintained at constant

temperature [87].

According to the thermal analysis of a single electrode (see Supplementary Materials), the instantaneous heat generation rate $\dot{Q}_i(t)$ (in mW) at each electrode is equal to the heat transfer rate $q_i''(t)$ passing through the thermoelectric heat flux sensor placed in thermal contact with the current collector, such that [87],

$$\dot{Q}_i(t) = q_i''(t)A_i = \frac{\Delta V_i(t)}{S_i}A_i \qquad \text{with } i = \ + \text{ or } - \tag{2.1}$$

where A_i denotes the footprint area of the electrode (in cm^2) and S_i is the temperature-dependent sensitivity of the heat flux sensor provided by the manufacturer (in $\mu\text{V}/(\text{W}/\text{m}^2)$). Here, the subscript "$i$" refers to either the positive "+" or negative "−" electrode. Here, $\Delta V_i(t)$ is the voltage difference measured within each thermoelectric heat flux sensor in thermal contact with electrode "i". The instantaneous total heat generation rate in the entire device (denoted by subscript "T") can be expressed as $\dot{Q}_T(t) = \dot{Q}_+(t) + \dot{Q}_-(t)$.

The instantaneous heat generation rate $\dot{Q}_i(t)$ can be decomposed as the sum of the irreversible $\dot{Q}_{irr,i}(t)$ and reversible heat generation rates $\dot{Q}_{rev,i}(t)$, i.e., $\dot{Q}_i(t)$ $= \dot{Q}_{irr,i}(t) + \dot{Q}_{rev,i}(t)$ [87]. The time-averaged heat generation rate over a cycle period t_{cd} corresponds to the time-averaged irreversible heat generation rate $\bar{\dot{Q}}_{irr,i}$ at electrode "i", i.e. [87],

$$\bar{\dot{Q}}_{irr,i} = \frac{1}{t_{cd}} \int_{(n_c-1)t_{cd}}^{n_c t_{cd}} \dot{Q}_i(t)\, dt \qquad \text{with } i = \ + \text{ or } \ - \,. \tag{2.2}$$

Here, n_c is the cycle number, chosen to be sufficiently large so that $\dot{Q}_i(t)$ has reached oscillatory steady state. Indeed, by definition, time-averaging of the reversible heat generation rate $\dot{Q}_{rev,i}(t)$ at electrode "i" over a complete charging-discharging cycle yields $\bar{\dot{Q}}_{rev,i} = 0$.

Finally, in the interest of comparing the reversible heat generation rate at each

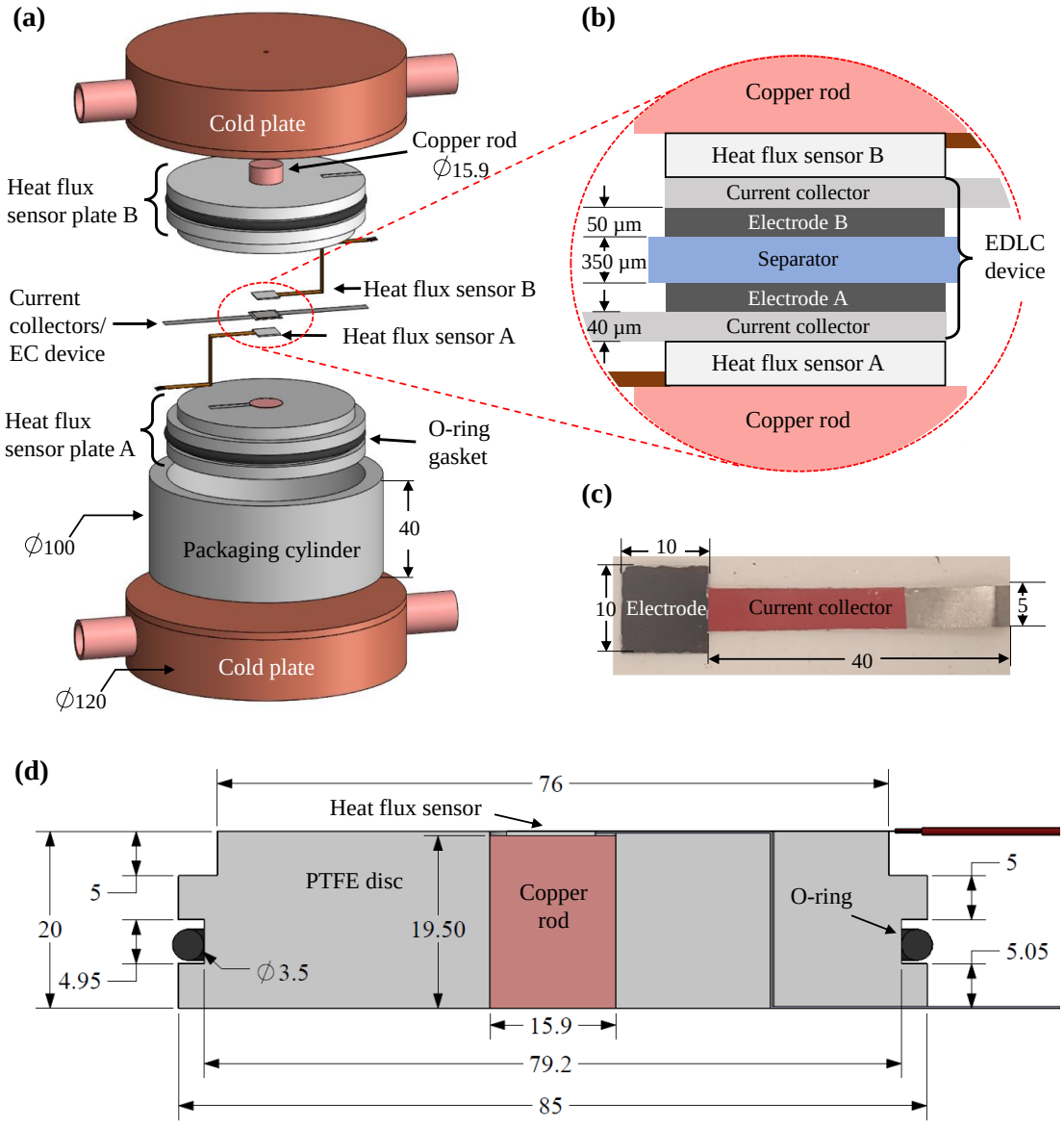

Figure 2.2: (a) Exploded and (b) enlarge view of the test area, (c) photograph of a 1×1 cm^2 activated carbon electrode supported by a 316 stainless steel current collector, and (d) cross-section view of a heat flux sensor plate with corresponding dimensions (all dimensions in mm).

electrode, the instantaneous reversible heat generation rate $\dot{Q}_{rev,i}(t)$ was averaged only over a charging period t_c of galvanostatic cycling [87],

$$\bar{\dot{Q}}^{c}_{rev,i} = \frac{1}{t_c} \int_{(n_c-1)t_{cd}}^{(n_c-1)t_{cd}+t_c} \dot{Q}_{rev,i}(t)\ dt \qquad \text{with } i = T,\ +,\ \text{or}\ -\,. \tag{2.3}$$

2.2.2 Heat generation in EDLCs

Munteshari et al. [87, 88] investigated EDLC cells consisting of two identical AC-based electrodes immersed in different organic or aqueous liquid electrolytes under cycling at constant current I [87,88]. For all aqueous and organic electrolytes tested, the irreversible heat generation rate at each electrode was found to be proportional to I^2 under constant current cycling with a potential window of 1 V. The total irreversible heat generation in the cell was equal to Joule heating expressed as $\bar{\dot{Q}}_J = R_s I^2$ where R_s is the internal resistance of the device measured from IR drop and found to be independent of current I [87]. Irreversible heat generation was the smallest in aqueous electrolytes as they typically have the largest ionic conductivity [38, 94]. Furthermore, reversible heat generation rate at the positive electrode was (i) exothermic during charging due to ion adsorption and (ii) endothermic during discharging due to ion desorption, as predicted theoretically [84, 85]. By contrast, at the negative electrode, the reversible heat generation rate was first endothermic and then exothermic during charging [87]. This was shown to be caused by negatively charged functional groups associated with carboxymethyl cellulose (CMC) binder forming at the negative electrode and responsible for the overscreening effect [88]. Indeed, the CMC binder consisted of carboxymethyl ($-CH_2COONa$) and hydroxyl ($-OH$) functional groups [88]. These groups dissociated in 1 M $LiPF_6$ in EC:DMC organic electrolyte forming negatively charged functional groups ($-CH_2COO^-$) and ($-O^-$) that attracted cations (e.g., Li^+), leading to overscreening of the electrode surface, illustrated in

Figure 2.3 [88, 95]. In order to balance the charge of the inner Helmholtz layer in the electrolyte, an additional layer of anions was required [88, 95]. Therefore, the negative electrodes containing CMC was first charged by repelling this anion layer (endothermic) followed by cations adsorption (exothermic) [88, 96].

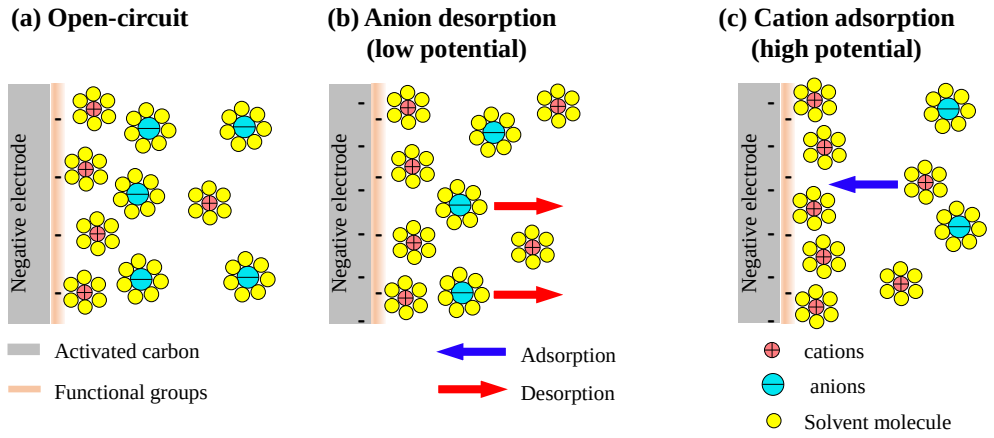

Figure 2.3: Schematic of ion displacement with negatively charged functional groups on negative electrode representing overscreening effect during (a) open-circuit (b) anion desorption and (c) cation adsorption.

2.2.3 Heat generation in hybrid pseudocapacitors

As previously mentioned, Dandeville et al. [86] investigated the heat generation in a hybrid pseudocapacitor consisting of an AC negative electrode and a MnO_2 positive electrode. The results indicated that (i) the irreversible heat generation rate at each electrode of the hybrid supercapacitor was due only to Joule heating, (ii) the reversible heat generation rate at the AC electrode was exothermic during charging and endothermic during discharging, and (iii) the reversible heat generation rate in the MnO_2 positive electrode was endothermic during charging and exothermic during discharging due to redox reactions [86], as observed numerically for both carbon-based and pseudocapacitive electrodes in the previously

mentioned hybrid psuedocapacitor model [92]. Munteshari et al. [87, 91] investigated a full-cell hybrid pseudocapacitive device consisting of MnO_2 nanoparticles on graphene (MnO_2-G) positive electrode and AC negative electrode in 0.5 M Na_2SO_4 aqueous electrolyte [91]. The device was cycled galvanostatically with constant current ranging from 2 to 6 mA under the potential window ranging between $\psi_{s,min} = 0.4$ V and $\psi_{s,max} = 1.4$ V. Here, the time-averaged irreversible heat generation rate at the negative AC electrode was to be proportional to I^2, where I was imposed current. Similar results were found experimentally for AC electrodes in EDLCs with various electrolytes [77, 86–88, 97] and numerically for carbon-based electrodes in EDLCs [84] and in hybrid pseudocapacitors [92]. In addition, the total irreversible heat generation rate in the entire device exceeded Joule heating expressed as $\bar{\dot{Q}}_J = R_s I^2$ where R_s is the internal resistance of the device measured from IR drop and found to be independent of current I [91]. This additional heat generation rate was attributed to irreversible heat generation rates due to (i) Faradaic reaction, termed as polarization heating, and (ii) EDL formation hysteresis at pseudocapacitive electrode surface [92]. Furthermore, the reversible heat generation rate at AC negative electrode was (i) exothermic during charging due to Na^+ cation adsorption and (ii) endothermic during discharging due to Na^+ cation desorption, as predicted theoretically [84, 85]. By contrast, the reversible heat generation rate at pseudocapacitive MnO_2-G positive electrode was (i) endothermic during charging due to fast surface redox of non-spontaneous Na^+ desorption accompanied by the change in oxidation state from Mn^{3+} to Mn^{4+} and (ii) exothermic during discharging due to Na^+ adsorption with the change in oxidation state from Mn^{4+} to Mn^{3+} [91].

2.3 Neat and diluted Pyr_{14}TFSI ionic liquid-based electrolytes

Ionic liquid Pyr_{14}TFSI and its mixtures with organic solvents have been used widely as electrolytes in ECs due to their exceptional thermal, electrochemical,

and cycling stability [98–102]. In fact, the operating potential window of neat $Pyr_{14}TFSI$ can be as high as $\sim$ 3.5 V in the temperature range of 20 to 60 °C [39] compared with $\leq$ 3 V for organic electrolytes (e.g., ACN) and $\sim$ 1 V for aqueous electrolytes [37]. The maximum potential windows of $Pyr_{14}TFSI$ mixtures in PC or ACN were recommended to be up to 3.5 V at 20 °C [39]. In addition, $Pyr_{14}TFSI$-based electrolytes show larger power and/or energy densities and better capacitance retention compared to the widely used organic electrolyte tetraethylammonium tetrafluoroborate ($TEABF_4$) in PC or ACN [98,103]. Furthermore, leakage current was about three times smaller in activated carbon (AC)-based EDLCs with $Pyr_{14}TFSI$, neat or diluted in PC, than with $TEABF_4$ in PC [104]. Indeed, the ionic conductivity of neat $Pyr_{14}TFSI$ is as low as $\sim$ 2.0 mS/cm at 20 °C [40, 41]. Nevertheless, it depends strongly on temperature and increases to $\sim$ 7.0 mS/cm at 60 °C [101, 105]. In addition, the ionic conductivity of 1 M $Pyr_{14}TFSI$ diluted in PC increased to 10.3 mS/cm at 25 °C [98]. However, the potential window and the operating temperature may be further limited by the solvent decomposition [49]. Furthermore, unlike neat ILs, for ILs dissolved in organic solvents, solvated ions must be fully or partially desolvated in order to enter the pores and to form EDL at the electrode/electrolyte interface during charging [9,106]. Desolvation is an endothermic process since the enthalpy of solvation is always positive (exothermic) due to Van der Waals forces controlling the interaction between the ions and the solvent molecules [94, 107, 108].

CHAPTER 3

Heat Generation in Diluted Ionic Liquid-Based EDLCs for 1 V Potential Window Between 20 and 60 °C

This chapter reports for the first time, isothermal calorimetric measurements of the instantaneous heat generation rate at each electrode of ionic liquid-based electric double layer capacitors (EDLCs) at three different temperatures, 20 °C, 40 °C, and 60 °C, under galvanostatic cycling using an *in operando* isothermal calorimeter. Here, the ionic liquid-based electrolyte consists of 1 M N-butyl-n-methylpyrrolidinium bis(trifluoromethane sulfonyl)imide ($Pyr_{14}TFSI$) dissolved in propylene carbonate (PC). The potential window was limited to 1 V to compare with results from similar devices using aqueous or organic electrolytes.

3.1 Materials and methods

3.1.1 Electrode and device fabrication

Activated carbon slurries were prepared by mixing activated carbon (YP-50F, Kuraray Chemical), TX-100 surfactant (DOW Chemical), carboxymethyl cellulose (CMC, DOW Chemical) as a thickening agent/binder, and styrene-butadiene rubber (SBR, MTI Corp.) as a binder, in DI water in an 80:5:1.5:13.5 weight ratio. The slurry was drop casted onto carbon-coated aluminum current collector sheets (MTI Corp.) with 1 × 1 cm^2 footprint area. The current collectors had been previously treated by oxygen plasma to enhance their hydrophilicity and ensure uniform spreading of the slurry. The electrodes were dried in a vacuum oven at 120 °C for 24 h before being placed in a glove box under argon (Ar) atmosphere (< 1 ppm H_2O/O_2). The mass loading on each electrode was 2.5 mg (2.0 mg of

AC) corresponding to an electrode thickness of about 60 μm.

The EDLC cell consisted of two identical activated carbon electrodes separated by a 1 mm-thick chemical-resistant polypropylene mesh separator with electrolyte made of 1 M Pyr_{14}TFSI ionic liquid electrolyte dissolved in PC. Here, PC was used to dilute the ionic liquid Pyr_{14}TFSI in order to increase the ionic conductivity of the electrolyte and improve the wetting of the AC electrodes without sacrificing thermal stability since the boiling temperature of PC is around 240 °C [48]. In addition, the concentration of 1 M Pyr_{14}TFSI in PC was selected in this experiment because it corresponds to the maximum ionic conductivity of about 8.3 mS/cm and its lowest viscosity around 5 mPa.s at 20 °C [109]. Finally, the device was assembled and placed in the calorimeter compartment inside the glove box under Ar atmosphere before being taken out for isothermal calorimetric measurements at temperature between 20 °C and 60 °C.

3.1.2 Device characterization

The device's gravimetric integral capacitance $C_{int,m}$ (in F/g) was evaluated from cyclic voltammetry (CV) curve as a function of scan rate ν according to [110],

$$C_{int,m}(\nu) = \frac{1}{m(\psi_{s,max} - \psi_{s,min})} \oint \frac{I(\psi_s)}{2\nu} \mathrm{d}\psi_s \tag{3.1}$$

where ν is the scan rate varying from 5 to 30 mV/s. Here, m is the total mass loading of AC ($m = 4.0$ mg) in both electrodes while $I(\psi_s)$ is the measured current at cell potential ψ_s over the potential window ranging between $\psi_{s,min} = 0$ V and $\psi_{s,max} = 1$ V. This potential window may appear narrow for IL-based EDLCs but it was selected (i) to facilitate comparison with previous experimental studies measuring the heat generation rate at 20 °C in EDLCs using aqueous and organic electrolytes [87, 88] and (ii) to avoid parasitic phenomena occurring under larger potential window range including potential ion intercalation in AC [50] and/or

electrochemical decomposition of solvent PC [49]. Subsequently, galvanostatic cycling was performed on the device with constant current I ranging from 2 to 6 mA and at temperature of 20 °C, 40 °C, or 60 °C. Here, fifteen consecutive cycles were performed for each value of current I to ensure that oscillatory steady state had been reached in the calorimetric measurements. The gravimetric differential capacitance $C_{diff,m}$ (in F/g) can be estimated from galvanostatic cycling according to [110],

$$C_{diff,m}(I) = \frac{I}{m|\mathrm{d}\psi_s/\mathrm{d}t|} \tag{3.2}$$

where $|\mathrm{d}\psi_s/\mathrm{d}t|$ was estimated for each cycle, at the end of the discharging and charging steps.

Furthermore, the internal resistance R_s was calculated from the IR drop at the charging/discharging transitions under galvanostatic cycling at current I [89, 111–113],

$$R_s(I) = \frac{\psi_s(t_c^+) - \psi_s(t_c^-)}{2I} \tag{3.3}$$

where $\psi_s(t_c^+)$ and $\psi_s(t_c^-)$ denote the potentials across the cell at the end of the charging step and immediately after the beginning of the discharging step, respectively. The IR drop, $\psi_s(t_c^+) - \psi_s(t_c^-)$, was obtained by estimating the cell potential $\psi_s(t_c^-)$ 10 ms after the beginning of the discharging step (i.e., $t_c^+ - t_c^- = 10$ ms), as suggested for supercapacitors by Zhao et al. [112] and successfully used in our previous studies [87, 88].

3.1.3 Isothermal Calorimeter

In this study, the instantaneous heat generation rate at each electrode of the device was measured under galvanostatic cycling at constant temperature of 20 °C, 40 °C, and 60 °C using an *in operando* calorimeter described in Background. According to the thermal analysis of a single electrode (see Supplementary Materials), the instantaneous heat generation rate $\dot{Q}_i(t)$ (in mW) at each electrode is equal to

the heat transfer rate $q_i''(t)$ passing through the thermoelectric heat flux sensor placed in thermal contact with the current collector, such that [87],

$$\dot{Q}_i(t) = q_i''(t) A_i = \frac{\Delta V_i(t)}{S_i} A_i \qquad \text{with } i = \ + \text{ or } - \tag{3.4}$$

where A_i refers to the footprint area of the electrode (in cm^2) and S_i denotes the temperature-dependent sensitivity of the heat flux sensor provided by the manufacturer (in $\mu\mathrm{V}/(\mathrm{W}/\mathrm{m}^2)$). Here, subscript "$i$" refers to either the positive "+" or negative "−" electrode. In addition, $\Delta V_i(t)$ refers to the voltage difference measured within each thermoelectric heat flux sensor in thermal contact with electrode "i". The instantaneous total heat generation rate in the entire device (denoted by subscript "T") can be written as $\dot{Q}_T(t) = \dot{Q}_+(t) + \dot{Q}_-(t)$.

In addition, the instantaneous heat generation rate $\dot{Q}_i(t)$ in each electrode can be decomposed as the sum of the irreversible $\dot{Q}_{irr,i}(t)$ and reversible $\dot{Q}_{rev,i}(t)$ heat generation rates, i.e., $\dot{Q}_i(t) = \dot{Q}_{irr,i}(t) + \dot{Q}_{rev,i}(t)$ [87, 88]. By definition, time-averaging of the reversible heat generation rate $\dot{Q}_{rev,i}(t)$ at electrode "i" over a complete charging-discharging cycle yields $\bar{\dot{Q}}_{rev,i} = 0$. Therefore, the time-averaged heat generation rate $\dot{Q}_i(t)$ over a cycle period t_{cd} is equal to the time-averaged irreversible heat generation rate $\bar{\dot{Q}}_{irr,i}$ at electrode "i", i.e. [87, 88],

$$\bar{\dot{Q}}_{irr,i} = \frac{1}{t_{cd}} \int_{(n_c-1)t_{cd}}^{n_c t_{cd}} \dot{Q}_i(t)\, dt \qquad \text{with } i = \ + \text{ or } \ - \,. \tag{3.5}$$

Here, n_c is the cycle number, chosen to be sufficiently large for $\dot{Q}_i(t)$ to reach oscillatory steady state. Finally, in the interest of comparing the reversible heat generation rate at each electrode, the instantaneous reversible heat generation rate

$\dot{Q}_{rev,i}(t)$ was time-averaged solely over a charging period t_c according to [87, 88],

$$\bar{\dot{Q}}^{c}_{rev,i} = \frac{1}{t_c} \int_{(n_c-1)t_{cd}}^{(n_c-1)t_{cd}+t_c} \dot{Q}_{rev,i}(t)\ dt \qquad \text{with } i = T,\ +,\ \text{or}\ -\,. \tag{3.6}$$

3.2 Results and discussion

3.2.1 Cyclic voltammetry and gravimetric integral capacitance

Figure 3.1(a) shows the measured CV curves of the device at 20 °C for five different scan rates ν between 5 and 30 mV/s. All curves featured a nearly rectangular and symmetrical shape characteristic of ideal EDLCs. Figure 3.1(b) shows CV curves of the device at different temperatures for scan rate $\nu = 20$ mV/s. Here, the CV curves were also rectangular at all temperatures and expanded slightly from 20 to 60 °C. This was likely due to the increase in electrical conductivity of the electrolyte with increasing temperature, as previously discussed. Similar results were observed at all scan rates (see Supplementary Materials).

Figure 3.2 plots the gravimetric integral capacitance $C_{int,m}$ of the device investigated [Equation (3.1)] as a function of scan rate ν for the three different temperatures. Here, $C_{int,m}$ was around 15 to 25 F/g, a typical value for carbon-based electrodes with organic or IL-based electrolytes for the range of scan rate considered [88, 114–116]. Figure 3.2 also indicates that the gravimetric integral capacitance $C_{int,m}$ decreased slightly with increasing scan rate ν for all three temperatures, as generally observed in various AC-based [87, 117, 118] and graphene-based [114] EDLCs. This can be attributed to ion-diffusion limitations in the porous electrodes [119]. Finally, Figure 3.2 establishes that the gravimetric integral capacitance $C_{int,m}$ increased with increasing temperature for any given scan rate. For example, $C_{int,m}$ at $\nu = 20$ mV/s was 17 F/g at 20 °C and 21 F/g at 60 °C. This was due to better ion mobility at higher temperature.

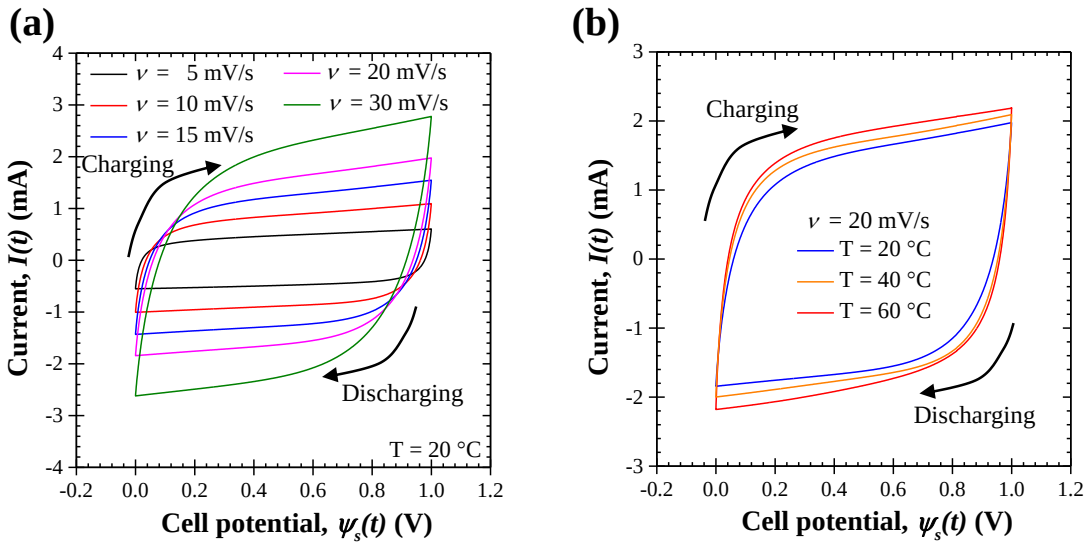

Figure 3.1: Cyclic voltammogram from a two AC-electrode cell with 1 M $Pyr_{14}TFSI$ in PC electrolyte (a) at 20 °C for scan rates ν between 5 and 30 mV/s, and (b) for scan rate $\nu = 20$ mV/s at temperature between 20 °C and 60 °C.

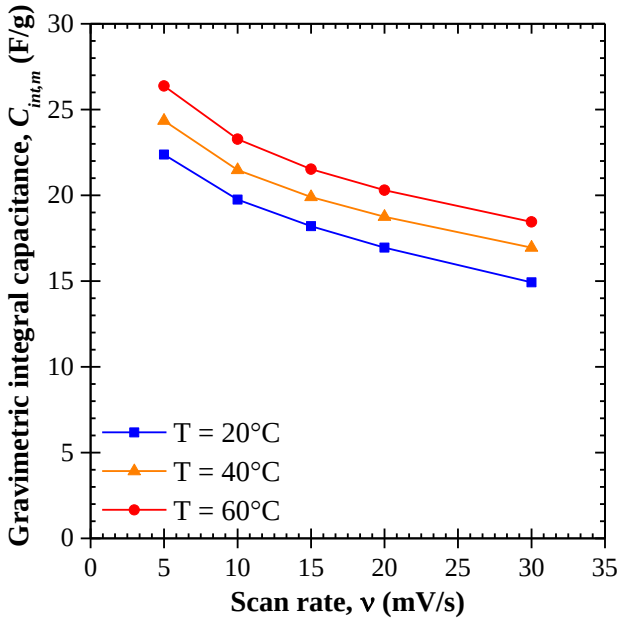

Figure 3.2: Gravimetric integral capacitance $C_{int,m}$ obtained from CV curves of an AC-based EDLC cell with 1 M $Pyr_{14}TFSI$ in PC electrolyte for three different temperatures 20 °C, 40 °C, and 60 °C for scan rate ν between 5 and 30 mV/s.

3.2.2 Galvanostatic cycling

Figure 3.3(a) shows galvanostatic charge-discharge curves plotting the cell potential $\psi_s(t)$ as a function of time t at 20 °C for five different values of imposed current I ranging from 2 to 6 mA. The cell potential $\psi_s(t)$ varied almost linearly with time t between the minimum $\psi_{s,min}$ and maximum $\psi_{s,max}$ potentials, except for the IR drop. These results confirm the near ideal EDLC behavior of the device also observed in CV curves. Figure 3.3(a) indicates that as expected the IR drop $\psi_s(t_c^+) - \psi_s(t_c^-)$ increased with increasing current I [87, 88, 97]. In addition, Figure 3.3(b) shows the galvanostatic charge-discharge curves obtained at current $I = 4$ mA for different temperatures. Here, the IR drop was the largest at 20°C and decreased with increasing temperature. This was due to the increasing electrolyte ionic conductivity with increasing temperature. In addition, the charging-discharging time t_{cd} increased with increasing temperature from 25 s at 20 °C to 34 s at 60 °C, as also observed in Refs. [62, 65, 70, 75]. This increase in capacitance can be attributed to (i) the decrease in the electrolyte viscosity resulting in better infiltration of the electrolyte in the porous electrode [120–122] and to (ii) the increase in ion mobility in the electrolyte [62,65,69,70,75]. Similar results were obtained for different currents (see Supplementary Materials).

Figure 3.4(a) shows the internal resistance R_s obtained from the IR drop [Equation (3.3)] as a function of galvanostatic cycle number n_c. Here, R_s was plotted for fifteen galvanostatic cycles at 20 °C, 40 °C, and 60 °C for each value of current I ranging from 2 to 6 mA. Here, the internal resistance R_s was fairly constant throughout $5 \times 15 = 75$ cycles for each temperature considered. In addition, Figure 3.4(b) shows the average internal resistance $\bar{R}_s$ as a function of imposed current I for 20 °C, 40 °C, and 60 °C. Here, the average internal resistance $\bar{R}_s$ was relatively constant and independent of imposed current I. It is evident that both R_s and $\bar{R}_s$ decreased with increasing temperature from around $\bar{R}_s = 26.0 \pm 0.3\ \Omega$ at 20 °C down to $17.9 \pm 0.2\ \Omega$ at 40 °C, and $13.8 \pm 0.2\ \Omega$ at 60 °C due to

enhanced ions mobility.

Figure 3.5(a) shows the gravimetric differential capacitance $C_{diff,m}$ as a function of galvanostatic cycle number n_c calculated by Equation (3.2). Here, $C_{diff,m}$ was plotted for fifteen cycles at 20 °C, 40 °C, and 60 °C for five different values of imposed current ranging from 2 to 6 mA. First, Figure 3.5(a) indicates that $C_{diff,m}$ decreased with increasing current I. This could be due to ion diffusion limitation through the porous electrode under high current and fast charging time. In addition, $C_{diff,m}$ increased with increasing temperature for any given current I. For example, for $I = 4$ mA, $C_{diff,m}$ was 15.0 F/g at 20°C and increased by 15% and 24% at 40 °C and 60 °C, respectively. Furthermore, $C_{diff,m}$ was only slightly larger during charging than during discharging for any current imposed I and at any temperature, suggesting high energy efficiency. In fact, Figure 3.5(b) shows the coulombic efficiency defined as the ratio of the discharging time t_d to the charging time t_c, i.e., $CE = t_d/t_c$ where t_c and t_d are the duration of the charging and discharging steps, respectively (Figure 3.3). Here, CE was about 98% for the first cycle at each current I and reached nearly 100% in subsequent cycles indicating highly reversible capacity and good stability of the device even at 60 °C.

3.2.3 Instantaneous and time-averaged heat generation rates

Figures 3.6(a) to 3.6(c) show the temporal evolution of the heat generation rates $\dot{Q}_+(t)$ and $\dot{Q}_-(t)$ measured at the positive and negative electrodes and $\dot{Q}_T(t) = \dot{Q}_+(t)+\dot{Q}_-(t)$ as functions of dimensionless time t/t_{cd} for five consecutive galvanostatic cycles under constant current $I = 4$ mA and constant temperature of (a) 20 °C, (b) 40 °C, and (c) 60 °C. The corresponding time-averaged heat generation rates $\bar{\dot{Q}}_{irr,+}$, $\bar{\dot{Q}}_{irr,-}$, and $\bar{\dot{Q}}_{irr,T}$ are also shown. The results indicate that the heat generation rates, for all temperatures considered, were repeatable cycle after cycle. The heat generation rate at the negative electrode $\dot{Q}_-(t)$ oscillated with smaller

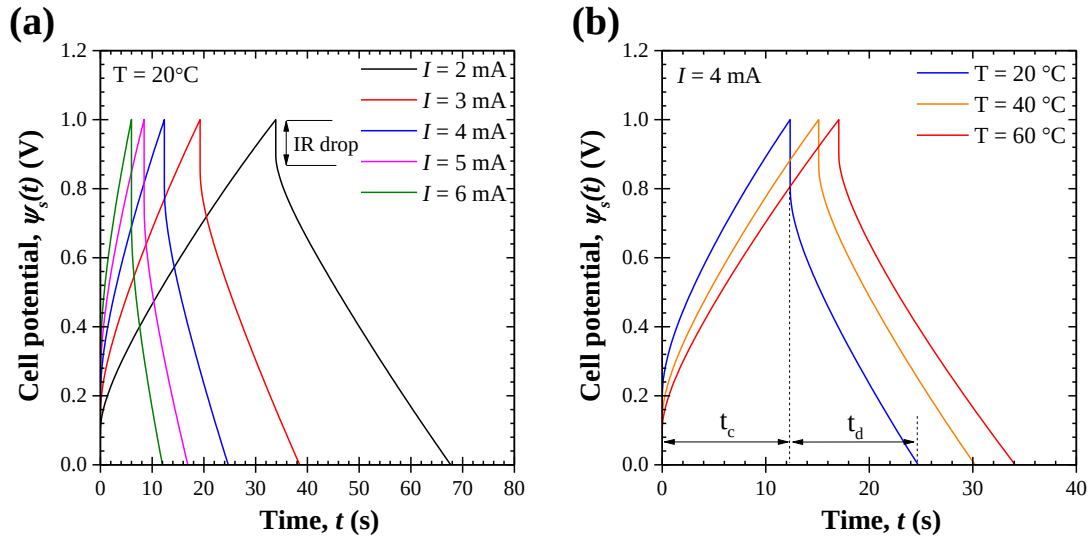

Figure 3.3: Cell potential under galvanostatic cycling (a) at 20 °C under imposed current I ranging between 2 and 6 mA, and (b) under imposed current $I = 4$ mA at 20 °C, 40 °C, and 60 °C.

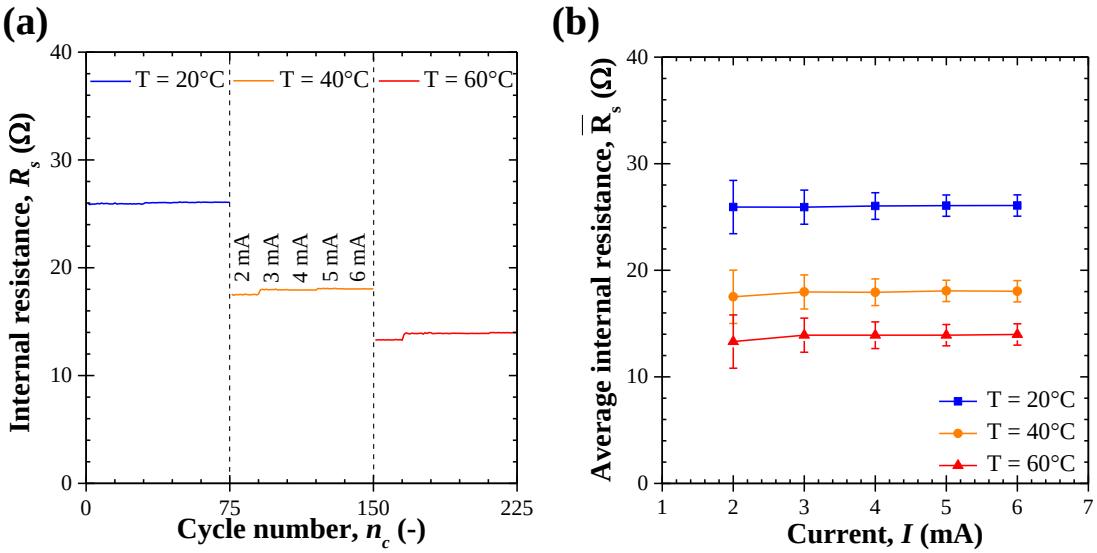

Figure 3.4: (a) Internal resistance R_s of the IL-based EDLC cell investigated and retrieved from galvanostatic cycling at three different temperatures 20 °C, 40 °C, and 60 °C and under imposed current I ranging from 2 to 6 mA. (b) Average internal resistance $\bar{R}_s$ as a function of imposed current I at 20 °C, 40 °C, and 60 °C.

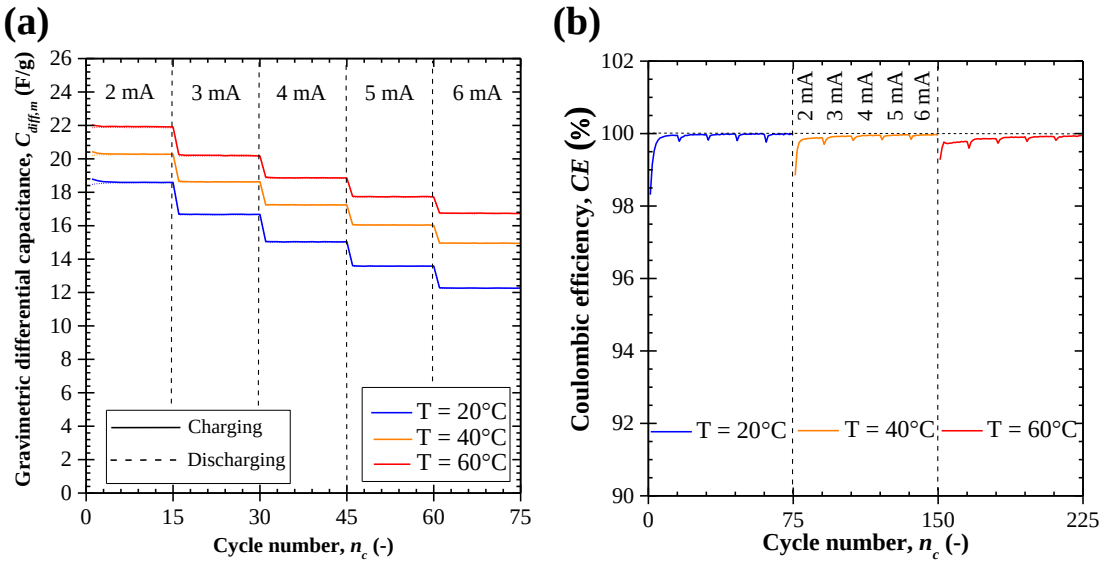

Figure 3.5: (a) Gravimetric differential capacitance $C_{diff,m}$ of the IL-based EDLC cell investigated as a function of constant current cycle number during the charging and discharging steps and (b) coulombic efficiency CE for consecutive cycles at temperatures 20 °C, 40 °C, and 60 °C and for current I ranging from 2 to 6 mA.

amplitude than that at the positive electrode $\dot{Q}_+(t)$ at 20 °C. This difference between electrodes, however, vanished at 60 °C, as explained when considering the reversible heat generation rate at each electrode. In addition, the amplitude of oscillations in both $\dot{Q}_+(t)$ and $\dot{Q}_-(t)$ increased with increasing temperature, as discussed later.

Figures 3.6(d) to 3.6(f) show the corresponding time-averaged irreversible heat generation rates $\bar{\dot{Q}}_{irr,+}$, $\bar{\dot{Q}}_{irr,-}$, and $\bar{\dot{Q}}_{irr,T}$ [Equation (3.5)] under galvanostatic cycling as functions of I^2 for constant current I ranging from 2 to 6 mA at (d) 20 °C, (e) 40 °C, and (f) 60 °C. The error bars correspond to two standard deviations or 95% confidence interval estimated by evaluating $\bar{\dot{Q}}_{irr,i}$ for five consecutive cycles. Figures 3.6(d) to 3.6(f) also show predictions for the heat generation rate due to Joule heating expressed as $\bar{\dot{Q}}_J = \bar{R}_s(T)I^2$ where $\bar{R}_s(T)$ is the average internal resistance reported in Figure 3.4(b). These results established that the measured total irreversible heat generation rate $\bar{\dot{Q}}_{irr,T}$ under galvanostatic cycling was in excellent agreement with predictions of Joule heating $\bar{\dot{Q}}_J$ for all three temperatures

considered. In other words, Joule heating was the main cause of irreversible heat generation in the EDLC cell investigated, for the potential window of 1 V. Similar results were obtained previously with EDLCs consisting of AC-based electrodes with aqueous or organic electrolytes under the same cycling conditions as in the present study [87, 88].

Furthermore, for all temperatures, the time-averaged irreversible heat generation rates $\bar{\dot{Q}}_{irr,-}$ and $\bar{\dot{Q}}_{irr,+}$ at the negative and positive half-cells were linearly proportional to I^2 and the coefficient of proportionality corresponded to their respective resistances R_- and R_+. It is interesting to note that, at all temperatures, R_- and R_+ were very similar and that their sum was equal to the internal resistance R_s, i.e., $R_- \approx R_+$ and $R_- + R_+ \approx R_s$. Here, each half-cell resistance R_+ and R_- can be considered as the resistance of the electrode and electrolyte in series. First, the positive and negative electrodes were synthesized in the same manner and should be nearly identical. Second, the diffusion coefficients of Pyr_{14}^+ cations and $TFSI^-$ anions were similar when 1 M of $Pyr_{14}TFSI$ is dissolved in PC, i.e., $D_+ \approx D_-$ [105, 123]. Therefore, the ionic conductivities of the electrolyte in each half cell should also be similar, as observed in Figure 3.6, for all temperatures. Finally, Figure 3.6 establishes that both R_+ and R_- decreased with increasing temperature due to the corresponding increase in ion mobility [48].

3.2.4 Reversible heat generation rates

Joule heating was shown previously to dominate irreversible heat generation in EDLCs (Figure 3.6). Thus, under constant current cycling, the instantaneous irreversible heat generation rate was independent of time, i.e., $\dot{Q}_{irr,i}(t) = \bar{\dot{Q}}_{irr,i} = R_i I^2$. Then, the instantaneous reversible heat generation rate $\dot{Q}_{rev,i}(t)$ at electrode "i" can be estimated by subtracting the irreversible heat generation rate $\bar{\dot{Q}}_{irr,i}$ from

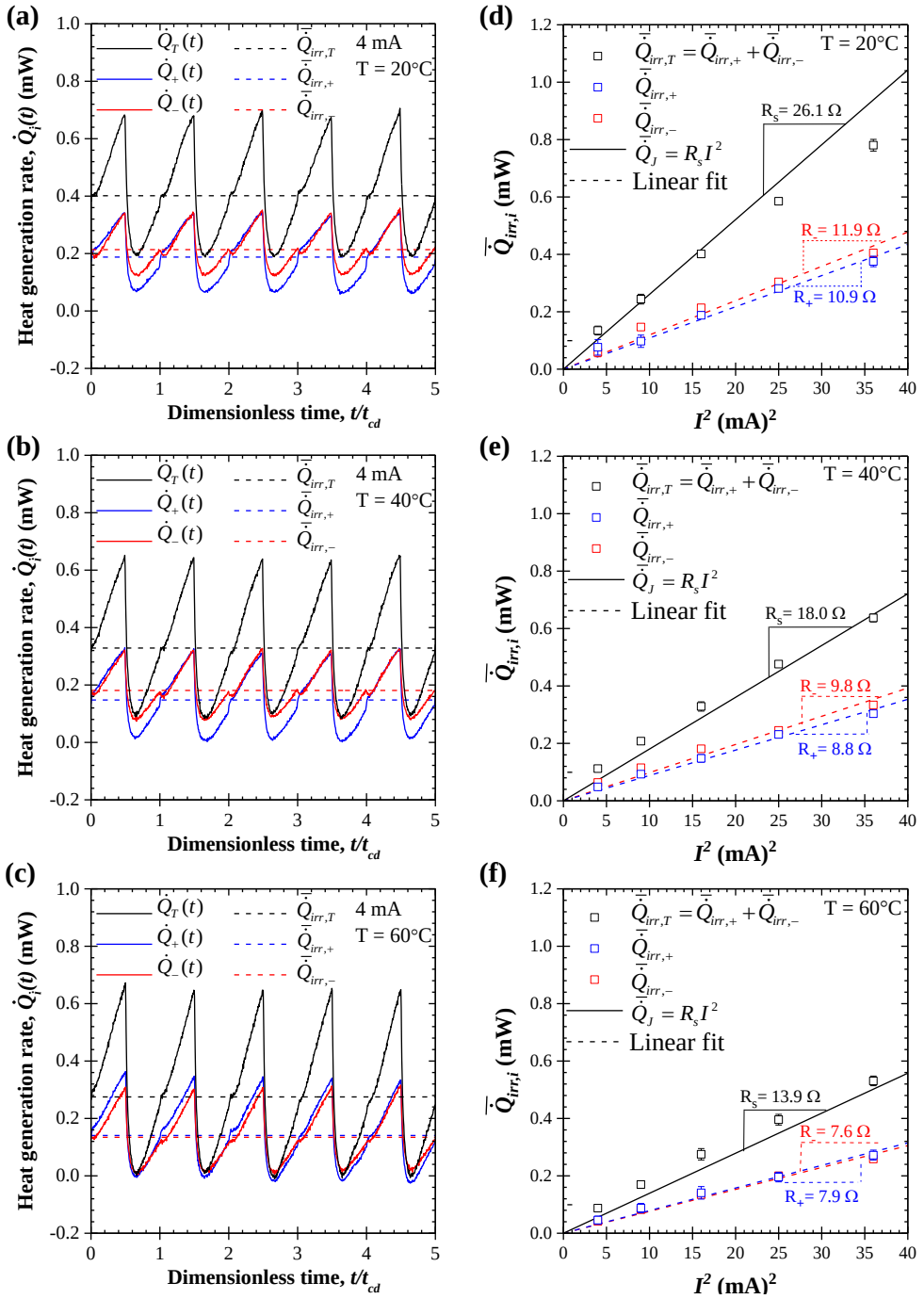

Figure 3.6: Instantaneous heat generation rates $\dot{Q}_+(t)$ at the positive electrode, $\dot{Q}_-(t)$ at the negative electrode, and $\dot{Q}_T(t)$ in the entire cell as functions of the dimensionless time t/t_{cd} for current $I = 4$ mA at constant temperature of (a) 20 °C, (b) 40 °C, and (c) 60 °C. Time-averaged heat generation rates $\bar{\dot{Q}}_{irr,+}$, $\bar{\dot{Q}}_{irr,-}$, and $\bar{\dot{Q}}_{irr,T}$ under galvanostatic cycling as functions of I^2 for current I ranging between 2 and 6 mA at (d) 20 °C, (e) 40 °C, and (f) 60 °C.

the instantaneous heat generation rate $\dot{Q}_i(t)$ to yield [87, 88],

$$\dot{Q}_{rev,i}(t) = \dot{Q}_i(t) - \bar{\dot{Q}}_{irr,i} \qquad \text{with } i = \ + \text{ or } \ - \,. \tag{3.7}$$

Figure 3.7 plots the instantaneous reversible heat generation rates (a) $\dot{Q}_{rev,+}(t)$ at the positive electrode, (b) $\dot{Q}_{rev,-}(t)$ at the negative electrode, and (c) $\dot{Q}_{rev,T}(t)$ in the entire cell as functions of the dimensionless time t/t_{cd} for current $I = 4$ mA at constant temperature of 20 °C, 40 °C, and 60 °C under oscillatory steady state. Here, two different cycles were plotted for each temperature, namely cycle number $n_c = 11$ and 15. Figures 3.7(a) to 3.7(c) establish that $\dot{Q}_{rev,+}(t)$, $\dot{Q}_{rev,-}(t)$, and $\dot{Q}_{rev,T}(t)$ were repeatable from cycle to cycle and featured a similar behavior for all temperatures considered. In addition, the magnitude of the reversible heat generation rates $\dot{Q}_{rev,+}(t)$, $\dot{Q}_{rev,-}(t)$, and $\dot{Q}_{rev,T}(t)$ increased slightly with temperature. The same observations were made for different currents (see Supplementary Materials). This could be due to the fact that a larger number of ions were adsorbed at the electrode/electrolyte interface at higher temperature, as suggested by the larger capacitance [Figure 3.5(a)]. Moreover, $\dot{Q}_{rev,+}(t)$ was slightly larger than $\dot{Q}_{rev,-}(t)$ for any value of temperature and current considered. Based on our previous first principle thermal model [85], this could be attributed to the fact that smaller $TFSI^-$ anions (~ 0.7 nm) were adsorbed at the positive electrode during charging thus generating more heat than adsorption of larger Pyr_{14}^+ cations (~ 1.1 nm) [105, 109]. In addition, the difference between $\dot{Q}_{rev,+}(t)$ and $\dot{Q}_{rev,-}(t)$ became smaller as temperature increased. This could be due to the fact that higher temperatures (i) facilitate the desolvation of large and solvated Pyr_{14}^+ cations and (ii) accelerate the desorption process of sub-layer anions in overscreening effect at the negative electrode due to better ion mobility. The reversible heat generation rates $\dot{Q}_{rev,+}(t)$ and $\dot{Q}_{rev,-}(t)$ at the positive and negative electrodes were both mostly (i) exothermic during charging due to ion adsorption and (ii) endothermic dur-

ing discharging due to ion desorption. This was also consistent with results from numerical simulations [84, 85]. Note that, $\dot{Q}_{rev,-}(t)$ featured a small endothermic dip at the beginning of the charging step that was not observed in $\dot{Q}_{rev,+}(t)$. This could be attributed to overscreening effect due to negatively charged functional groups of CMC binder, as observed also with organic and aqueous electrolytes [88]. Alternatively, it could be due to complete or partial endothermic desolvation of Pyr_{14}^{+} cations of their PC solvation shell while moving into the AC pores to form an EDL during charging [9, 94, 106]. In fact, PC molecules are more likely to interact with Pyr_{14}^{+} cations forming solvated PC$-Pyr_{14}^{+}$ cations [124] while $TFSI^{-}$ anions were found not to be significantly solvated by PC [125].

Finally, Figure 3.7 shows the time-averaged reversible heat generation rates during a charging step (d) $\bar{\dot{Q}}^{c}_{rev,+}$ at the positive electrode, (e) $\bar{\dot{Q}}^{c}_{rev,-}$ at the negative electrode, and (f) $\bar{\dot{Q}}^{c}_{rev,T}$ in the entire cell as functions of current I ranging from 2 to 6 mA for temperature T of 20 °C, 40 °C, and 60 °C. It indicates that $\bar{\dot{Q}}^{c}_{rev,+}$, $\bar{\dot{Q}}^{c}_{rev,-}$, and $\bar{\dot{Q}}^{c}_{rev,T}$ increased slightly with increasing temperature while $\bar{\dot{Q}}^{c}_{rev,+}$ was larger than $\bar{\dot{Q}}^{c}_{rev,-}$ for any given current I, as expected from analyzing Figures 3.7(a)− 3.7(c). In addition, $\bar{\dot{Q}}^{c}_{rev,+}$, $\bar{\dot{Q}}^{c}_{rev,-}$, and $\bar{\dot{Q}}^{c}_{rev,T}$ increased linearly with imposed current I for all temperatures considered. This was consistent with previous experimental results for EDLC cells consisting of AC-electrodes with organic or aqueous electrolytes [86–88] and with numerical simulations of EDLCs [84].

During operation of commercial EDLCs, heat generation can result in significant temperature rise [5, 6, 77–79]. Thus, thermal management measures should be taken to prevent overheating. To do so, several strategies have been proposed including heat removal from EDLC modules by forced convection air-cooling [79], by circulating coolant, and by using phase change material [126]. The results of the present study could facilitate (i) the definition of safe modes of operation, (ii) the development of effective thermal management strategies, and (iii) the improvement of existing thermal model predicting the temperature evolution during

operation.

3.3 Chapter summary

This chapter measured, for the first time, the effects of operating temperature and the use of ionic liquid in organic solvent on the irreversible and reversible heat generation rates at each electrode of AC-based EDLCs. The electrolyte was 1 M $Pyr_{14}TFSI$ in PC and the temperature varied between 20 and 60 °C while the potential window was limited to 1 V to facilitate comparison with previous studies on similar devices but using aqueous or organic electrolytes. The results establish that Joule heating was the main source of irreversible heat generation for the operating conditions considered. Similar results have been obtained previously with aqueous or organic electrolytes for similar devices and operating conditions at 20 °C. The internal resistance R_s and, consequently, the irreversible heat generation rate decreased with increasing temperature due to enhanced ion mobility in the IL-based electrolyte. In addition, the irreversible heat generation rates at the positive and negative electrodes were similar. Furthermore reversible heat generation rates at the positive and negative electrodes were mostly exothermic during charging and endothermic during discharging due to the change in entropy of the electrolyte system. It increased slightly with increasing temperature and was larger at the positive electrode due to the fact that adsorbing $TFSI^-$ anions were smaller than Pyr_{14}^+ cations. The reversible heat generation rate at the negative electrode featured a small endothermic dip at the beginning of the charging step potentially due to overscreening effect and/or endothermic desolvation of PC molecules from Pyr_{14}^+ cations.

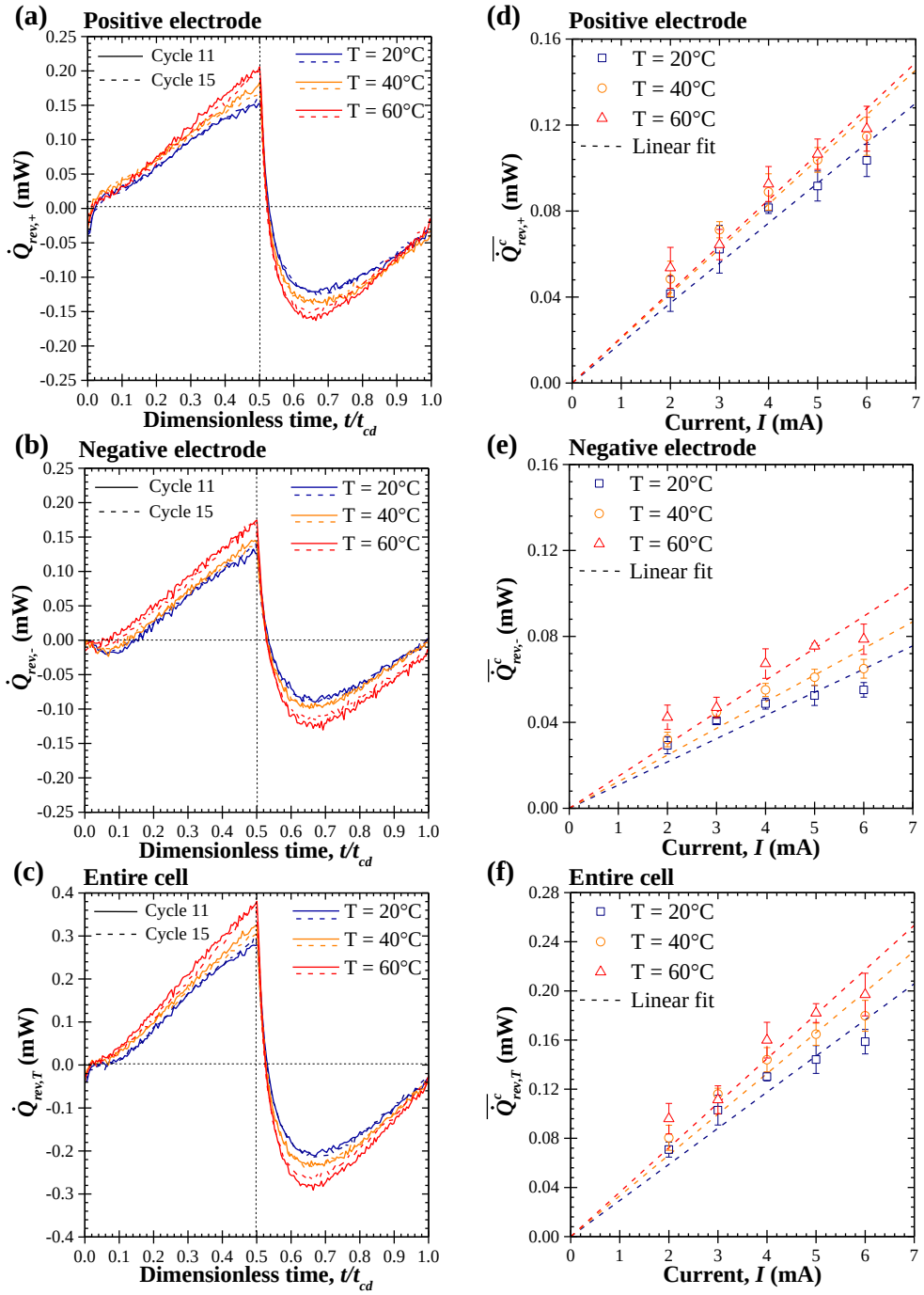

Figure 3.7: Reversible heat generation rates (a) $\dot{Q}_{rev,+}(t)$ at the positive electrode, (b) $\dot{Q}_{rev,-}(t)$ at the negative electrode, and (c) $\dot{Q}_{rev,T}(t)$ in the entire cell as functions of the dimensionless time t/t_{cd} for two galvanostatic cycles under current $I = 4$ mA for temperature of 20 °C, 40 °C, and 60 °C. Time-averaged reversible heat generation rates during the charging step (d) $\bar{\dot{Q}}^{c}_{rev,+}$ at the positive electrode, (e) $\bar{\dot{Q}}^{c}_{rev,-}$ at the negative electrode, and (f) $\bar{\dot{Q}}^{c}_{rev,T}$ in the entire cell as functions of current I ranging between 2 and 6 mA for temperature of 20 °C, 40 °C, and 60 °C.

CHAPTER 4

Heat Generation in Neat and Diluted Ionic Liquid-Based EDLCs for 2.5 V Potential Window Between 5 and 80 °C

This chapter investigates the effect of temperature on the heat generation and the associated electrochemical phenomena occurring in IL-based EDLCs. The EDLCs consisted of two identical activated carbon electrodes with neat $Pyr_{14}TFSI$ or $Pyr_{14}TFSI$ diluted in propylene carbonate (PC) as electrolytes. The instantaneous heat generation rate at each electrode was measured by isothermal calorimetry between 5 and 80 °C under constant current cycling and potential window of 2.5 V. First, the instantaneous heat generation rate was similar at each electrode in neat IL. However, it was smaller at the negative electrode in diluted IL and featured endothermic dips growing with increasing temperature > 40 °C due to overscreening effects, ion desolvation, and/or decomposition of PC. The irreversible heat generation was similar in each half-cell and decreased with increasing temperature due to the reduction in internal resistance, particularly with neat IL. The irreversible heat generation exceeded Joule heating in all cases, especially at high temperature and low current. This was attributed to ion desorption and charge redistribution in the porous electrodes. Finally, the reversible heat generation for both electrolytes was larger at the positive than at the negative electrode due to the difference in anion and cation sizes.

4.1 Background

4.1.1 Effect of potential window

As previously discussed, the operating potential window is an essential parameter for improving the specific energy of EDLCs. However, the operating potential window may be limited by the electrochemical stability window (ESW) of the electrolyte at a given temperature. Leyva-Garcia et al. [49] investigated the effect of potential window on the electrochemical performance of porous activated carbon (AC) electrodes with (i) neat $Pyr_{14}TFSI$ or (ii) 1 M $Pyr_{14}TFSI$ in PC electrolytes at 20 °C. The authors observed a redox peak in the CV curves at the negative electrode in 1 M $Pyr_{14}TFSI$ in PC electrolyte whereas no redox peak was observed in neat $Pyr_{14}TFSI$. They attributed this redox peak to PC solvent decomposition at the negative electrode under large potential [49]. Indeed, under large potential windows, PC decomposes (i) at the cathode to produce propane and hydrogen gases due to PC reduction or (ii) at the anode to produce carbon dioxide, propylene oxide, and other byproducts due to PC oxidation [49,127,128].

Moreover, Borenstein et al. [50] reported that a significant amount of FSI^- anions intercalated in the positive electrode of an AC-based EDLC with neat $Pyr_{14}FSI$ ionic liquid electrolyte after 3,000 galvanostatic cycles at $\Delta\psi_s = 3.4$ V [50]. This finding was confirmed by scanning electron microscopy and energy dispersive X-ray spectroscopy (SEM-EDX) measurements.

More recently, Munteshari et al. [90] studied the effects of potential window ranging from 1 to 4 V on the heat generation rate in cells consisting of two identical porous AC electrodes with either neat $Pyr_{14}TFSI$ or 1 M $Pyr_{14}TFSI$ in PC electrolytes using *in operando* isothermal calorimeter at 20 °C. For devices with neat $Pyr_{14}TFSI$ electrolyte, an endothermic dip appeared in the instantaneous heat generation rate at the positive electrode for cell potential window of 4.0 V as a result of $TFSI^-$ intercalation, as confirmed by EDX spectroscopy [90]. On the

other hand, for devices with 1 M Pyr_{14}TFSI in PC electrolyte, an endothermic dip appeared in the instantaneous heat generation rate at the negative electrode starting from cell potential window of 3.0 V as a result of PC decomposition [90]. In addition, the irreversible and reversible heat generation rates at both electrodes increased with increasing potential window for given current in both neat and diluted Pyr_{14}TFSI electrolytes [90]. For 1 M Pyr_{14}TFSI in PC electrolyte, the irreversible heat generation rate increased sharply as the potential window increased from 3.0 V to 3.5 V due to PC decomposition at potential window of 3.5 V [90]. Furthermore, unlike previous studies [87,88] with cell potential window $\Delta\psi_s \leq 1$ V, the total irreversible heat generation rate of the entire cell exceeded Joule heating for $\Delta\psi_s > 1$ V in both neat and diluted Pyr_{14}TFSI electrolytes [90]. This additional irreversible heat generation rate was attributed to the heat generation associated with charge redistribution in the porous carbon electrode and identified as the leakage current dissipated through the pore resistance [90].

4.1.2 Effect of temperature

In Chapter 3, we investigated the effect of operating temperature on irreversible and reversible heat generation rates in a full-cell device consisting of two identical porous AC electrodes with 1 M Pyr_{14}TFSI in PC electrolyte cycled with a potential window of 1 V [76]. The instantaneous heat generation rate at each electrode was measured at temperatures ranging from 20 to 60 °C [76] using an *in operando* isothermal calorimeter [87]. The measurement were similar at both electrodes and proportional to I^2. Their sum was equal to Joule heating given by $\bar{\dot{Q}}_J(T) = R_s(T)I^2$ where $R_s(T)$ is the internal resistance of the device measured at temperature T and I is the imposed current. The internal resistance $R_s(T)$ and thus $\bar{\dot{Q}}_J(T)$ decreased with increasing temperature due to the increasing electrolyte ionic conductivity [76]. However, the reversible heat generation rate was found to be independent of temperature for the potential window of 1 V considered [76].

Overall, previous calorimetric studies have investigated the instantaneous heat generation rate in EDLCs (i) with aqueous or organic electrolytes for potential window $\Delta\psi_s \leq 1.0$ V at 20 °C [87], (ii) with neat $Pyr_{14}TFSI$ or 1 M $Pyr_{14}TFSI$ in PC for potential window varying from 1.0 V to 4.0 V at 20 °C [90], and (iii) with 1 M $Pyr_{14}TFSI$ in PC for potential window of 1.0 V and temperature varying from 20 to 60 °C [76]. The present study aims to assess the effect of temperature on reversible and irreversible heat generation rates in EDLC with IL-based electrolyte under galvanostatic cycling. Here, a potential window of 2.5 V was chosen as a stable potential window for both neat $Pyr_{14}TFSI$ and 1 M $Pyr_{14}TFSI$ in PC electrolytes at 20 °C. The operating temperature was varied between 5 and 80 °C to assess its effect on the heat generation rate. The results can also be used to design thermal management strategies for EDLCs and to determine the operating limits of the devices.

4.2 Materials and methods

4.2.1 Electrode and device fabrication

Activated carbon slurries were prepared by mixing (i) activated carbon (YP-50F, Kuraray Chemical), (ii) TX-100 surfactant (DOW Chemical), (iii) carboxymethyl cellulose (CMC, DOW Chemical) used as a thickening agent/binder, and (iv) styrene-butadiene rubber (SBR, MTI Corp.) as a binder, in DI water in an 80:5:1.5:13.5 weight ratio. The slurry was drop-casted onto carbon-coated aluminum current collector sheets (MTI Corp.) with 1×1 cm^2 footprint area. The current collectors were previously treated by oxygen plasma to enhance their hydrophilicity and ensure uniform spreading of the slurry. The mass loading on each electrode was 2.5 mg of slurry (2.0 mg of AC) corresponding to an electrode thickness of about 60 μm. The electrodes were dried in a vacuum oven at 120 °C for 24 h before being assembled into full-cell devices in a glove box under argon

(Ar) atmosphere (< 1 ppm H_2O/O_2).

The EDLC devices consisted of two identical activated carbon electrodes separated by a 1 mm-thick chemical-resistant polypropylene mesh serving as a separator and as thermal insulator. The devices were assembled using either (i) neat $Pyr_{14}TFSI$ (Device 1) or (ii) 1 M $Pyr_{14}TFSI$ diluted in PC electrolyte (Device 2). The concentration of 1 M $Pyr_{14}TFSI$ in PC corresponds to the maximum ionic conductivity ($\sim$ 8.3 mS/cm) and the lowest viscosity ($\sim$ 5 mPa·s) at 20 °C [109]. Finally, the device was assembled and placed in the calorimeter compartment inside a glove box under Ar atmosphere before being taken out for isothermal calorimetric measurements at temperatures ranging from 5 to 80 °C. The isothermal calorimeter was described in detail in Ref. [87].

4.2.2 Device characterization

First, linear sweep voltammetry (LSV) was employed to determine the electrochemical stability window (ESW) of the electrolytes with either (i) neat $Pyr_{14}TFSI$ or (ii) 1 M $Pyr_{14}TFSI$ in PC incorporated in a two-terminal stainless steel coin cell (MTI Corp). Each coin cell, consisted of two AC-based electrodes (previously described) with a diameter of 9.5 mm (3/8") separated by a Whatman glass microfiber D (Sigma-Aldrich). The coin cells were pressed to a pressure of $\sim$ 6 MPa inside of an argon-rich glovebox. LSV measurements were performed at slow sweep rate of 0.1 mV/s at temperatures 20 °C, 40 °C, and 80 °C.

Second, cyclic voltammetry (CV) measurements were performed on Devices 1 and 2 inside the isothermal calorimeter at scan rate ν ranging from 5 to 30 mV/s at temperatures ranging from 5 to 80 °C. The device's gravimetric integral capacitance $C_{int,m}$ (in F/g) was evaluated from the CV curves as a function of

scan rate ν according to [110],

$$C_{int,m}(\nu) = \frac{1}{m(\psi_{s,max} - \psi_{s,min})} \oint \frac{I(\psi_s)}{2\nu} \mathrm{d}\psi_s. \tag{4.1}$$

Here, m is the total mass loading of AC in both electrodes ($m = 4.0$ mg) while $I(\psi_s)$ is the current measured at cell potential ψ_s. A cell potential window between $\psi_{s,min} = 0$ V and $\psi_{s,max} = 2.5$ V was selected because it fell within the ESW of both electrolytes investigated at room temperature [90].

Third, galvanostatic cycling combined with calorimetric measurements were performed on the devices at constant current I ranging from 1 to 5 mA at temperatures between 5 and 80 °C. For a given temperature, fifteen consecutive cycles were performed for each value of current I to guarantee that oscillatory steady state had been reached. In addition, the gravimetric differential capacitance $C_{diff,m}$ (in F/g) was estimated according to [110],

$$C_{diff,m}(I) = \frac{I}{m|\mathrm{d}\psi_s/\mathrm{d}t|} \tag{4.2}$$

where $|\mathrm{d}\psi_s/\mathrm{d}t|$ was estimated at the end of the discharging or charging step for each cycle at constant current I.

Furthermore, the internal resistance R_s was calculated from the IR drop observed at the charging/discharging transitions under galvanostatic cycling according to [89, 111–113],

$$R_s(I) = \frac{\psi_s(t_c^+) - \psi_s(t_c^-)}{2I} \tag{4.3}$$

where $\psi_s(t_c^+)$ and $\psi_s(t_c^-)$ denote the potentials across the cell at the end of the charging step and immediately after the beginning of the discharging step, respectively. The IR drop, $\psi_s(t_c^+) - \psi_s(t_c^-)$, was obtained by estimating the cell potential $\psi_s(t_c^-)$ 10 ms after the beginning of the discharging step (i.e., $t_c^+ - t_c^- = 10$ ms), as suggested for supercapacitors by Zhao et al. [112] and successfully used in our

previous studies [76, 87, 88].

4.2.3 Isothermal Calorimeter

The instantaneous heat generation rate at each electrode in Devices 1 and 2 was measured under galvanostatic cycling at constant temperatures ranging from 5 to 80 °C. The instantaneous heat generation rate $\dot{Q}_i(t)$ (in mW) at electrode "i" was found by measuring the heat transfer rate $q_i''(t)$ through the thermoelectric heat flux sensor and in thermal contact with the current collector such that [87],

$$\dot{Q}_i(t) = q_i''(t)A_i = \frac{\Delta V_i(t)}{S_i}A_i \qquad \text{with } i = \ + \text{ or } - \tag{4.4}$$

where $\Delta V_i(t)$ refers to the instantaneous voltage difference measured within each thermoelectric heat flux sensor in thermal contact with electrode "i". Here, subscript "i" refers to either the positive "+" or negative "−" electrode. In addition, S_i denotes the temperature-dependent sensitivity of the heat flux sensor provided by the manufacturer (in μV/(W/m^2)) and A_i refers to the footprint area of the electrode (in cm^2). Then, the instantaneous total heat generation rate in the entire device (denoted by subscript "T") can be written as $\dot{Q}_T(t) = \dot{Q}_+(t) + \dot{Q}_-(t)$.

Moreover, the instantaneous heat generation rate $\dot{Q}_i(t)$ in each electrode can be decomposed as the sum of the reversible $\dot{Q}_{rev,i}(t)$ and irreversible $\dot{Q}_{irr,i}(t)$ heat generation rates, i.e., $\dot{Q}_i(t) = \dot{Q}_{rev,i}(t) + \dot{Q}_{irr,i}(t)$ [87, 88]. Furthermore, by definition, time-averaging of the reversible heat generation rate $\dot{Q}_{rev,i}(t)$ at electrode "i" over a complete charging-discharging cycle yields $\bar{\dot{Q}}_{rev,i} = 0$. Thus, the time-averaged heat generation rate of $\dot{Q}_i(t)$ over a charging-discharging cycle period t_{cd} is equal to the time-averaged irreversible heat generation rate $\bar{\dot{Q}}_{irr,i}$ at electrode

"i", i.e. [87, 88],

$$\bar{\dot{Q}}_{irr,i} = \frac{1}{t_{cd}} \int_{(n_c-1)t_{cd}}^{n_c t_{cd}} \dot{Q}_i(t)\, dt \qquad \text{with } i = \ + \text{ or } \ - \,. \tag{4.5}$$

Here, n_c refers to the cycle number chosen to be large enough for $\dot{Q}_i(t)$ to have reached oscillatory steady state.

Finally, in order to compare the reversible heat generation rate at each electrode, the instantaneous reversible heat generation rate $\dot{Q}_{rev,i}(t)$ was time-averaged only over a charging period t_c according to [87, 88],

$$\bar{\dot{Q}}^{c}_{rev,i} = \frac{1}{t_c} \int_{(n_c-1)t_{cd}}^{(n_c-1)t_{cd}+t_c} \dot{Q}_{rev,i}(t)\, dt \qquad \text{with } i = T, \ +, \text{ or } \ - \,. \tag{4.6}$$

4.3 Results and discussion

4.3.1 Combined thermal and electrochemical stabilities

Figure 4.1 plots the linear sweep voltammograms (LSVs) for coin cells with the same AC electrodes as those used for calorimetric measurement with either neat $Pyr_{14}TFSI$ or 1 M $Pyr_{14}TFSI$ in PC electrolyte at scan rate of 0.1 mV/s and temperatures of 20 °C, 40 °C, and 80 °C. The current density $i(\psi_s)$ was defined as the ratio of the measured current response $I(\psi_s)$ during increasing coin cell potential ψ_s over the footprint area of the AC-based electrode in the coin cell, i.e., $i(\psi_s) = I(\psi_s)/A$ with $A = 0.7$ cm^2. The ESW depends on the choice of the cutoff current density beyond which the electrolyte is considered unstable. The cutoff current density typically ranges between 10 μA/cm^2 and 1 mA/cm^2 [129]. Figure 4.1 indicates that the ESW of the neat $Pyr_{14}TFSI$ electrolyte decreased with increasing temperature from above 5.5 V at 20 °C, to 4.6 V at 40 °C, and down to 3.7 V at 80 °C, based on the cutoff current density of 0.5 mA/cm^2 suggested

in Refs [129–131].

Moreover, the ESW of the 1 M $Pyr_{14}TFSI$ in PC electrolyte was smaller than that of neat $Pyr_{14}TFSI$ for a given temperature due to the lower electrochemical stability of PC. In addition, the ESW decreased with increasing temperature from 4.2 V at 20 °C, to 3.7 V at 40 °C, and 3.3 V at 80 °C. Note that, partial decomposition of some electrolyte components may start below the reported ESW.

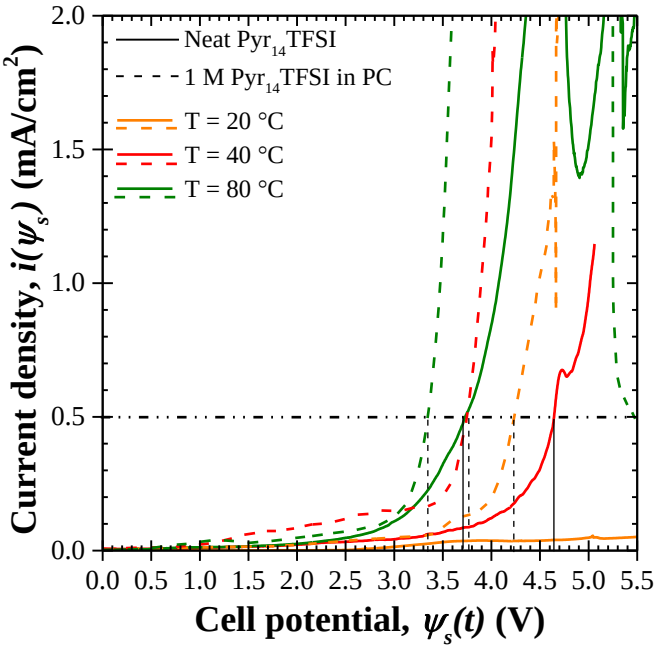

Figure 4.1: Linear sweep voltammograms for coin cells with two identical AC-based electrodes and either neat $Pyr_{14}TFSI$ or 1 M $Pyr_{14}TFSI$ in PC for sweep rate of 0.1 mV/s at 20 °C, 40 °C, and 80 °C.

4.3.2 Cyclic voltammetry and gravimetric integral capacitance

Figures 4.2(a) and 4.2(b) show the CV curves measured for Device 1 with neat $Pyr_{14}TFSI$ ionic liquid electrolyte at different temperatures between 5 and 80 °C for scan rate (a) $\nu = 5$ mV/s and (b) $\nu = 30$ mV/s, respectively. The CV curves at both scan rates featured leaf-like shape at low temperatures (≤ 20 °C) and became

larger and more rectangular with increasing temperature. These observations can be attributed to the increase in the ionic conductivity and to decreasing viscosity of neat IL with increasing temperature [101, 105]. However, at $T = 80$ °C, small and broad peaks were observed around $\psi_s \sim 1.0 - 2.0$ V for both positive and negative sweeps. This may be attributed to reversible Faradaic reactions involving electron transfer across the double layer, as observed in carbon-based SWNT at 100 °C [65] and graphene nanosheet at 60 °C in IL-based electrolytes [70].

Similarly, Figures 4.2(c) and 4.2(d) show the CV curves measured for Device 2 with 1 M $Pyr_{14}TFSI$ in PC electrolyte at different temperatures from 5 to 80 °C for scan rate (c) $\nu = 5$ mV/s and (d) $\nu = 30$ mV/s, respectively. Here, the CV curves were nearly rectangular at both low and high scan rates and did not change significantly with temperature, including at or below 20 °C. However, for slow charging at scan rate $\nu = 5$ mV/s, all curves featured a peak at the end of the charging step near $\psi_{s,max} = 2.5$ V that became more prominent as temperature increased, suggesting more ion storage due to increased ionic conductivity and accessibility in porous electrode [132] but also parasitic redox reactions at higher potential [133]. For faster charging at scan rate $\nu = 30$ mV/s, this change in current response peak with temperature was small due to ion transport limitation within shorter charging time and/or slow redox reactions.

Furthermore, for a given scan rate ν and temperature T, Device 2 featured current $I(t)$ two to eight times larger than that in Device 1 owing to better ion mobility when $Pyr_{14}TFSI$ is dissolved in PC. Moreover, the area enclosed by the CV curves of Device 1 expanded significantly with increasing temperature. By contrast, those of Device 2 almost collapsed on top of each other except near $\psi_{s,min}$ and $\psi_{s,max}$. In other words, the increase in temperature contributed greatly to improving the performance of Device 1 while it had a modest effect on that of Device 2. This was due to the fact that neat $Pyr_{14}TFSI$ features ionic conductivity and viscosity that depend strongly on temperature [101, 105], unlike $Pyr_{14}TFSI$

in PC.

Figures 4.3(a) and 4.3(b) plot the gravimetric integral capacitance $C_{int,m}$ [Equation (4.1)] as a function of scan rate ν for temperatures T ranging from 5 to 80 °C for Devices 1 and 2, respectively. Figure 4.3 indicates that, for a given temperature, the gravimetric integral capacitance $C_{int,m}$ decreased with increasing scan rate ν, as typically observed in various EDLCs [87,114,117,118] and attributed to ion-diffusion limitation in porous electrodes at high scan rates [119]. In addition, the capacitance $C_{int,m}$ of Device 2 was about two to five times larger than that of Device 1 for any given scan rate ν and temperature T. This was likely due to the fact that the dielectric constant ϵ_r of PC was much larger than that of $Pyr_{14}TFSI$. For example, ϵ_r(PC) $\approx$ 65 [134, 135] while ϵ_r($Pyr_{14}TFSI$) $\approx$ 11.7 to 14.7 at 25 °C [136–138]. Similarly, the viscosity of 1 M $Pyr_{14}TFSI$ in PC was much smaller than that of neat $Pyr_{14}TFSI$ leading to better wetting of the porous AC electrodes [70]. Moreover, Figure 4.3(a) establishes that the capacitance of Device 1 increased significantly with increasing temperature from ∼4 F/g at 5 °C to ∼21 F/g at 80 °C due to the increasing ion mobility of the neat IL with increasing temperature. On the other hand, $C_{int,m}$ of Device 2 increased slightly from ∼25 F/g at 5 °C to ∼32 F/g at 60 °C. Interestingly, performance of Device 2 started degrading at 80 °C and high scan rates.

4.3.3 Galvanostatic cycling

Figure 4.4 shows the galvanostatic charge-discharge curves plotting the cell potential $\psi_s(t)$ as a function of time t for Device 1 with neat $Pyr_{14}TFSI$ electrolyte at (a) I = 2 mA and (b) I = 4 mA and for Device 2 with 1 M $Pyr_{14}TFSI$ in PC electrolyte at (c) I = 2 mA and (d) I = 4 mA at different temperatures between 5 and 80 °C. The cell potential $\psi_s(t)$ in both devices varied linearly with time t at any current I and temperature T between potentials $\psi_{s,min}$ = 0 V and $\psi_{s,max}$ = 2.5 V, except for the IR drop. Figure 4.4 indicates that, for a given temper-

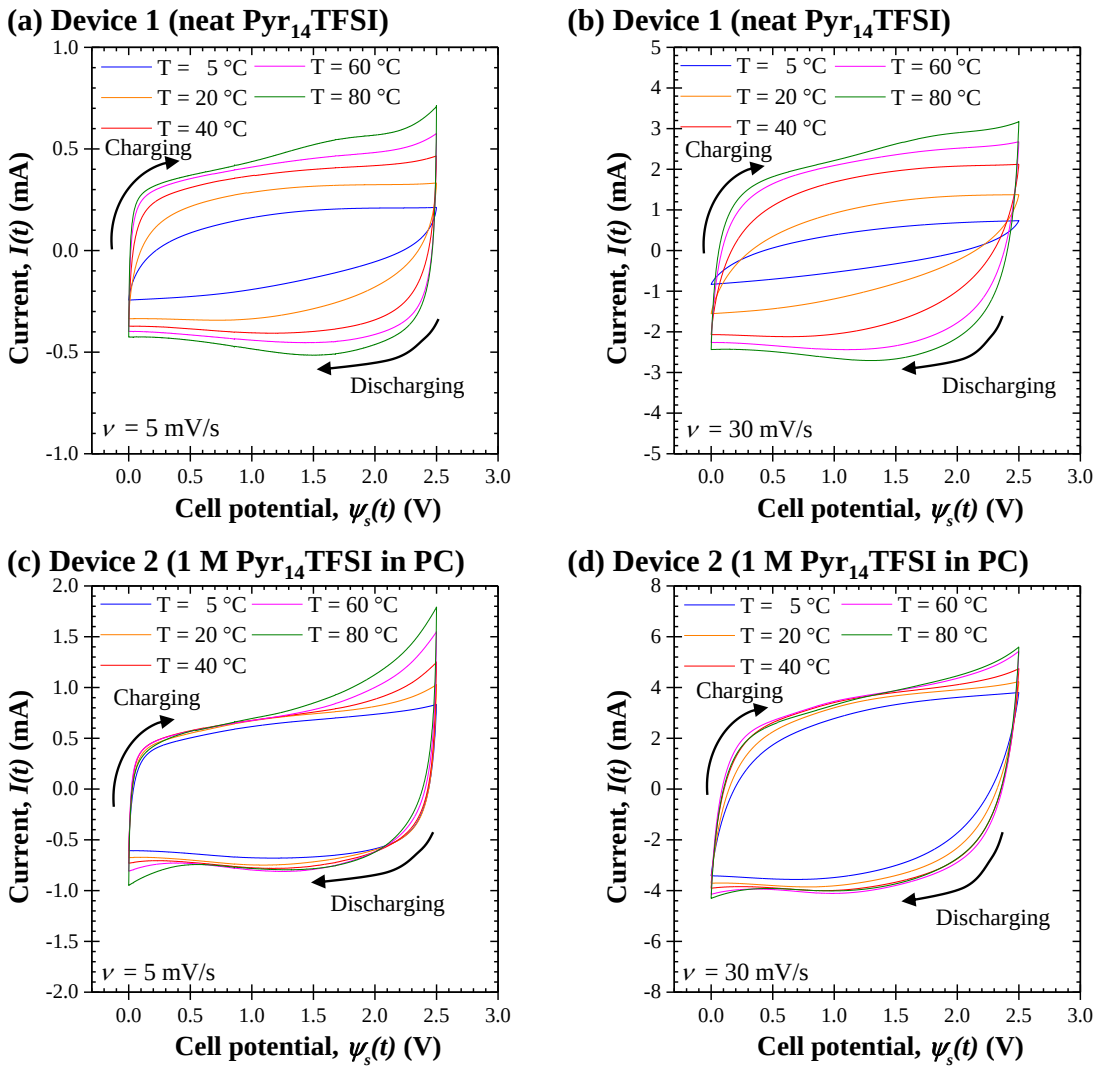

Figure 4.2: Cyclic voltammograms of (a) Device 1 with neat $Pyr_{14}TFSI$ at $\nu = 5$ mV/s and (b) at $\nu = 30$ mV/s and (c) Device 2 with 1 M $Pyr_{14}TFSI$ in PC at $\nu = 5$ mV/s and (d) at $\nu = 30$ mV/s at temperatures T ranging from 5 to 80 °C. The potential window ranged between $\psi_{s,min} = 0$ V and $\psi_{s,max} = 2.5$ V.

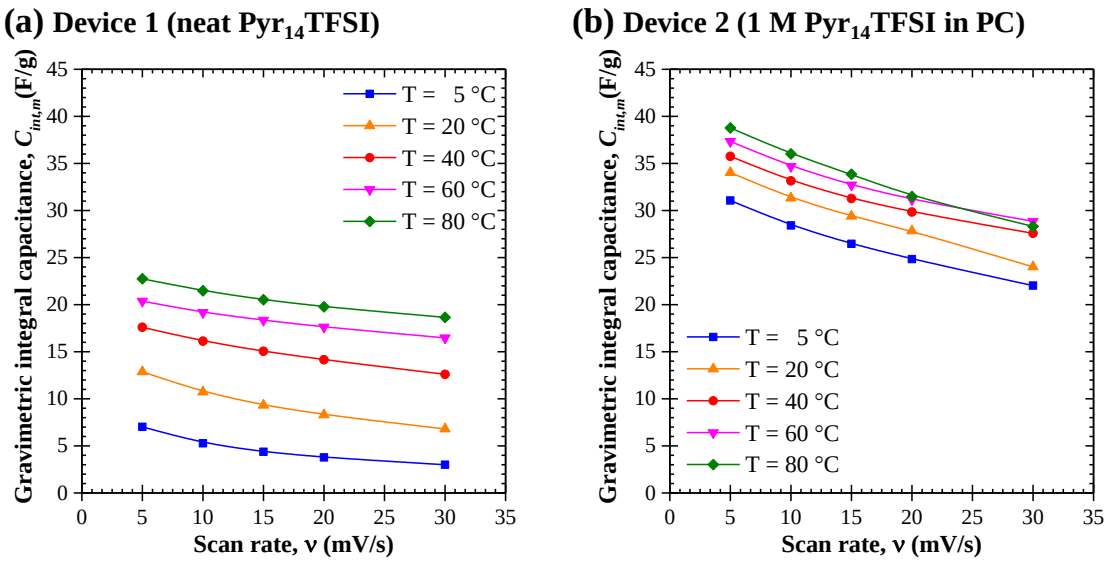

Figure 4.3: Gravimetric integral capacitance $C_{int,m}$ [Equation (4.1)] of (a) Device 1 with neat $Pyr_{14}TFSI$ and (b) Device 2 with 1 M $Pyr_{14}TFSI$ in PC electrolytes obtained from the CV curves shown in Figure 4.2 for temperature T ranging from 5 to 80 °C and scan rate ν between 5 and 30 mV/s.

ature, the IR drop $\psi_s(t_c^+) - \psi_s(t_c^-)$ increased with increasing current I for both devices [87,88,97]. It also decreased with increasing temperature for both devices except for Device 2 at 80 °C. Figure 4.5 shows charging-discharging times t_{cd} obtained from galvanostatic cycling curves in Figure 4.4 as functions of imposed current I ranging between 1 and 5 mA for (a) Device 1 with neat $Pyr_{14}TFSI$ and (b) Device 2 with 1 M $Pyr_{14}TFSI$ in PC for temperatures T ranging between 5 and 80 °C. Figure 4.5(a) indicates that t_{cd} of Device 1 decreased sharply with imposed current I but increased significantly with increasing temperature. Interestingly, in Device 1 with neat $Pyr_{14}TFSI$, operating temperature can limit the imposed current I. Here, at $T = 5$ °C, t_{cd} was already as small as 9 s for imposed current $I = 2$ mA resulting in a very small amount of energy storage. In other words, imposed current I larger than 2 mA is not recommended in use at 5 °C. By contrast, in Device 2 [Figure 4.5(b)], t_{cd} decreased with increasing current I and it increased slightly with increasing temperature T. Here, operating temperature did not limit the imposed current for the range of current considered. Moreover,

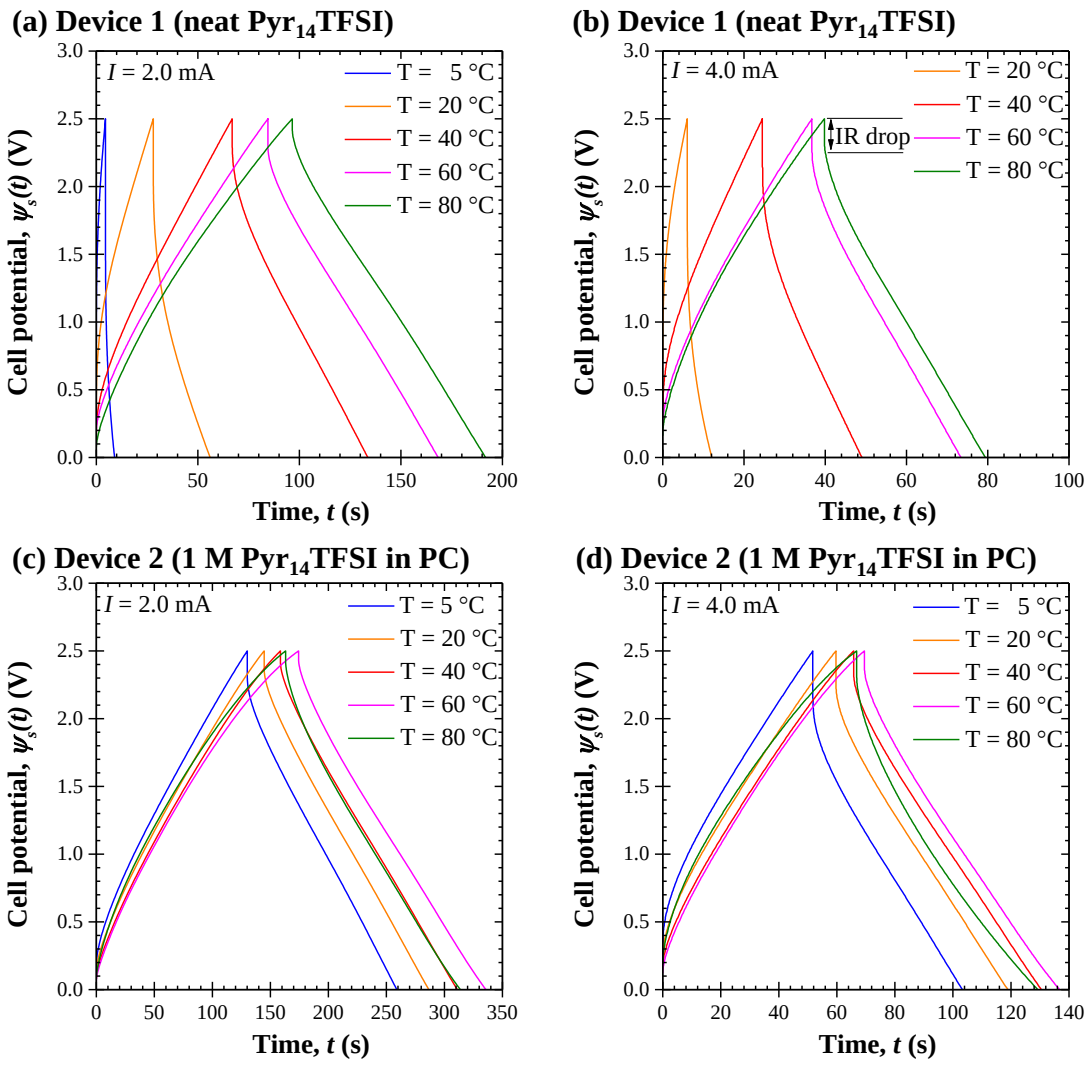

Figure 4.4: Cell potential under galvanostatic cycling for Device 1 with neat $Pyr_{14}TFSI$ electrolyte at (a) $I = 2$ mA and (b) $I = 4$ mA and for Device 2 with 1 M $Pyr_{14}TFSI$ in PC electrolyte at (c) $I = 2$ mA and (d) $I = 4$ mA for temperature T ranging from 5 to 80 °C and potential window between $\psi_{s,min} = 0$ V and $\psi_{s,max} = 2.5$ V.

t_{cd} was systematically larger for Device 2 than Device 1 for any given current I and temperature T confirming the larger charge storage capacity illustrated in Figure 4.3.

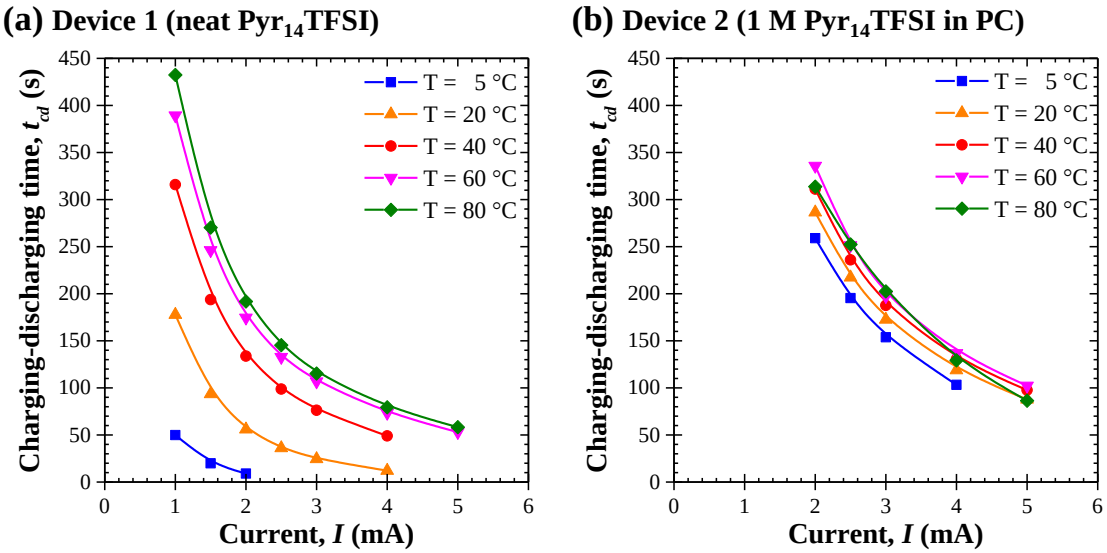

Figure 4.5: Charging-discharging times t_{cd} as functions of imposed current I ranging between 1 and 5 mA for (a) Device 1 with neat $Pyr_{14}TFSI$ and (b) Device 2 with 1 M $Pyr_{14}TFSI$ in PC for temperatures T ranging between 5 and 80 °C.

Figure 4.6 plots the internal resistance R_s obtained from the IR drop [Equation (4.3)] as a function of temperature T ranging from 5 to 80 °C for (a) Device 1 and (b) Device 2 for imposed current I ranging from 1 to 5 mA. Figure 4.6(a) establishes that the internal resistance R_s of Device 1 with neat $Pyr_{14}TFSI$ electrolyte (i) was independent of the imposed current I at any given temperature and (ii) decreased significantly with increasing temperature from $R_s = 213 \pm 6\ \Omega$ at 5 °C to $R_s = 22 \pm 5\ \Omega$ at 80 °C. This observation was due mainly to the significant increase in ionic conductivity of neat $Pyr_{14}TFSI$ with temperature [101, 105]. Similarly, Figure 4.6(b) indicates that the internal resistance R_s of Device 2 with 1 M $Pyr_{14}TFSI$ in PC electrolyte was nearly independent of the imposed current I and decreased with increasing temperature T. In fact, the internal resistance R_s of Device 2 decreased from around $R_s = 47 \pm 3\ \Omega$ at 5 °C to $R_s = 16 \pm 5\ \Omega$ at 60 °C and was about two to four times smaller than that of Device 1 at any

temperature up to 60 °C. Interestingly, the internal resistance R_s of Device 2 was larger at 80 °C than at 40 °C and 60 °C and depended on the imposed current I. This was due to PC decomposition at high temperatures and large potential windows. In fact, neat PC can lose about 10% of its initial mass within 4 h at 60 °C due to PC reduction at the negative electrode forming gaseous propane and/or hydrogen [127,139]. Note, however, that the rate of mass loss was smaller when mixed with ILs [127, 139]. Regardless, PC degradation impeded access of the liquid electrolyte to the pores in the porous electrode resulting in large internal resistance [127, 140]. Such increase in internal resistance with increasing temperature is responsible for thermal runaway [141].

Figure 4.7 shows the gravimetric differential capacitance $C_{diff,m}$ calculated from galvanostatic charge-discharge cycles [Equation (4.2)] as a function of cycle number n_c under different current I ranging from 1 to 5 mA for (a) Device 1 and (b) Device 2 at temperature T ranging between 5 and 80 °C. First, Figure 4.7 indicates that $C_{diff,m}$ decreased with increasing current I in both devices. This could be due to ion diffusion limitation through the porous electrode under high current and fast charging. In addition, for any imposed current I in both devices, $C_{diff,m}$ increased with increasing temperature, except for Device 2 beyond T = 60 °C. However, $C_{diff,m}$ of Device 1 was more sensitive to the temperature than that of Device 2. For example, in Device 1, $C_{diff,m}$ increased from 3.4 F/g at 20 °C to 16.1 F/g at 60 °C during discharging at I = 4 mA. By contrast, in Device 2, $C_{diff,m}$ increased only slightly from 27.4 F/g at 20 °C to 29.4 F/g at 60 °C also at I = 4 mA. Furthermore, $C_{diff,m}$ in both devices was slightly larger during charging than during discharging for any imposed current I and temperature T. This difference increased for smaller currents and higher temperatures. This could be attributed to self-discharge caused by (i) higher ion desorption rate at the electrode/electrolyte interface at high temperature and (ii) longer charging-discharging time t_{cd} at low current. Similar results were observed

in devices composed of activated carbon electrodes with 1 M $TEABF_4$ or 1 M $EMIBF_4$ in ACN electrolytes [74]. Interestingly, $C_{diff,m}$ of Device 2 at $T = 80$ °C featured unusual fluctuations. This is consistent with the previous explanation that gaseous and/or solid byproducts generated during PC decomposition impeded electrolyte from entering porous electrodes.

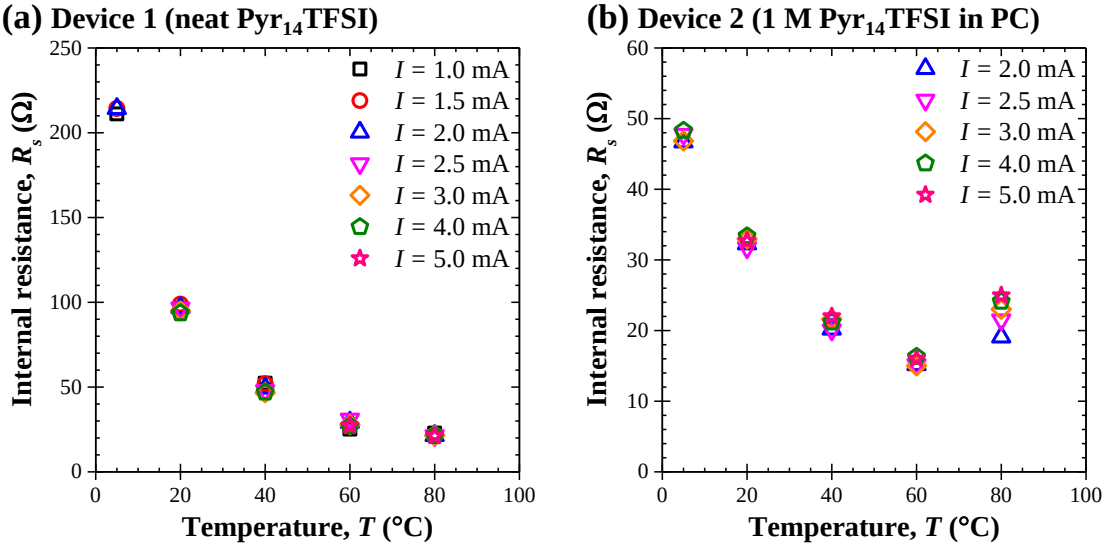

Figure 4.6: Internal resistance R_s [Equation 4.3] as a function of temperature T ranging from 5 to 80 °C for (a) Device 1 with neat $Pyr_{14}TFSI$ and (b) Device 2 with 1 M $Pyr_{14}TFSI$ in PC for imposed current I ranging from 1 to 5 mA.

4.3.4 Instantaneous heat generation rates

Figure 4.8 shows the instantaneous heat generation rates (a) $\dot{Q}_+(t)$ at the positive electrode and (b) $\dot{Q}_-(t)$ at the negative electrode for Device 1 with neat $Pyr_{14}TFSI$ electrolyte as functions of dimensionless time t/t_{cd} for different temperatures ranging between 5 and 80 °C during four consecutive galvanostatic cycles under constant current $I = 4$ mA. Similarly, Figures 4.8(c) and 4.8(d) show $\dot{Q}_+(t)$ and $\dot{Q}_-(t)$ for Device 2 with 1 M $Pyr_{14}TFSI$ in PC electrolyte, respectively. Note that, for Device 1, the imposed current I was limited to 2 mA at 5 °C due to an excessively large resistance and IR-drop and thus short charging-discharging

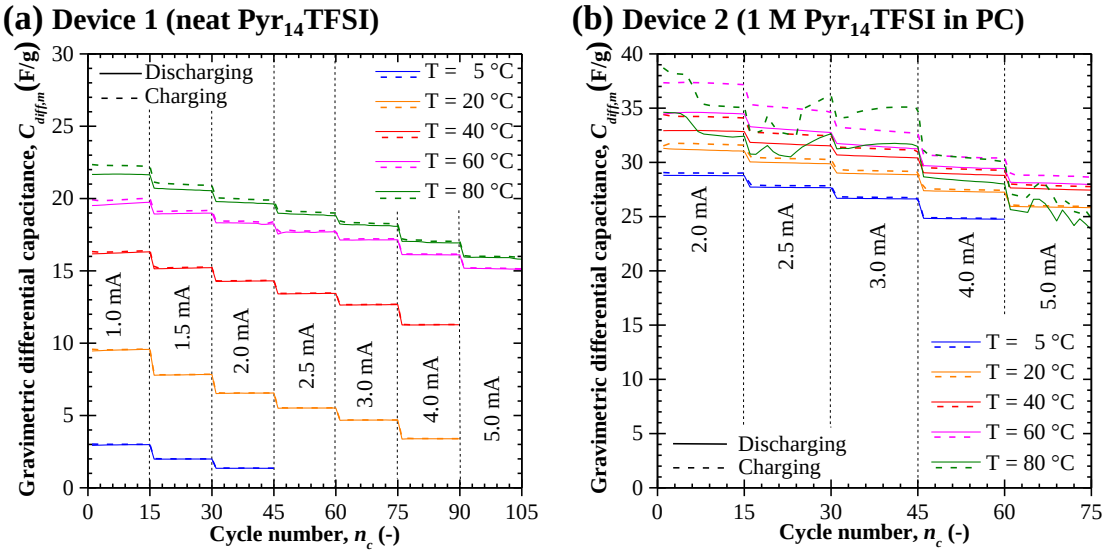

Figure 4.7: Gravimetric differential capacitance $C_{diff,m}$ of (a) Device 1 with neat $Pyr_{14}TFSI$ and (b) Device 2 with 1 M $Pyr_{14}TFSI$ in PC as a function of cycle number n_c during charging and discharging steps at constant current I between 1 and 5 mA and at temperature T ranging from 5 to 80 °C.

time t_{cd}. For both devices, Figure 4.8 indicates that the heat generation rate measurements were repeatable cycle after cycle for all temperatures considered. Note that the heat generation rate due to Joule heating – often considered as the only source of heat generation in EDLCs [6, 78, 79] – is constant over time under constant current cycling. Instead, experimental measurements in Figure 4.8 featured strong temporal oscillations due to additional heat generation processes including reversible processes such as ion adsorption/desorption and solvation/desolvation.

Figures 4.8(a) and 4.8(b) indicate that $\dot{Q}_+(t)$ and $\dot{Q}_-(t)$ at the positive and negative electrodes of Device 1 had similar magnitude for all temperatures, except for $T = 80$ °C when $\dot{Q}_+(t)$ was larger than $\dot{Q}_-(t)$. By contrast, in Device 2, the magnitude of $\dot{Q}_+(t)$ was consistently larger than that of $\dot{Q}_-(t)$ at any given temperature. This difference became larger with increasing temperature. Moreover, Figure 4.8 indicates that $\dot{Q}_+(t)$ and $\dot{Q}_-(t)$ decreased with increasing temperature in Devices 1 and 2 for temperatures up to 60 °C. However, in both devices, the amplitude of the oscillations in $\dot{Q}_+(t)$ and $\dot{Q}_-(t)$ increased with increasing tem-

perature. In Device 2 at 80 °C, both $\dot{Q}_+(t)$ and $\dot{Q}_-(t)$ increased due to the overall increase in internal resistance as a result of PC decomposition [Figure 4.6(b)].

Furthermore, the instantaneous heat generation rate $\dot{Q}_+(t)$ at the positive electrode in both devices was strictly (i) exothermic during charging due to ion adsorption and (ii) endothermic during discharging due to ion desorption. This was consistent with results obtained from numerical simulations [84, 85] and from previous experimental studies on AC-based EDLCs with aqueous, organic, or IL-based electrolytes [76, 87, 88, 90]. On the other hand, the instantaneous heat generation rate $\dot{Q}_-(t)$ at the negative electrode of both Devices 1 and 2 featured an endothermic dip at the beginning of the charging step whose magnitude increased with increasing temperature. This dip was more significant in Device 2 than in Device 1. Indeed, for Device 1 with neat $Pyr_{14}TFSI$, a small endothermic dip can be observed at $T \geq 40$ °C for potential window of 2.5 V. A similar endothermic dip was also observed at $T = 20$ °C albeit for larger potential window of 3.5 V and 4 V in similar devices with neat $Pyr_{14}TFSI$ electrolyte [90]. This dip was attributed to the overscreening effect at the beginning of the charging step in presence of CMC binder at the negative AC-electrode with neat $Pyr_{14}TFSI$ electrolyte, as explained previously [88, 90]. Similarly, the fact that the endothermic dip in $\dot{Q}_-(t)$ during charging was larger in Device 2 than in Device 1 could be due not only to the overscreening effect but also to the complete or partial endothermic desolvation of Pyr_{14}^+ cations of their PC solvation shell as they enter the AC nanopores to form an EDL [9, 94, 106, 142].

Finally, the endothermic dip at the negative electrode of Device 2 became noticeably larger with increasing temperature as a result of increasing PC decomposition caused by endothermic PC reduction reaction [90]. Note that, this dip dominated at the beginning of the charging step due to the competing and sharply increasing exothermic heat generation rate associated with cation adsorption throughout the charging step [90].

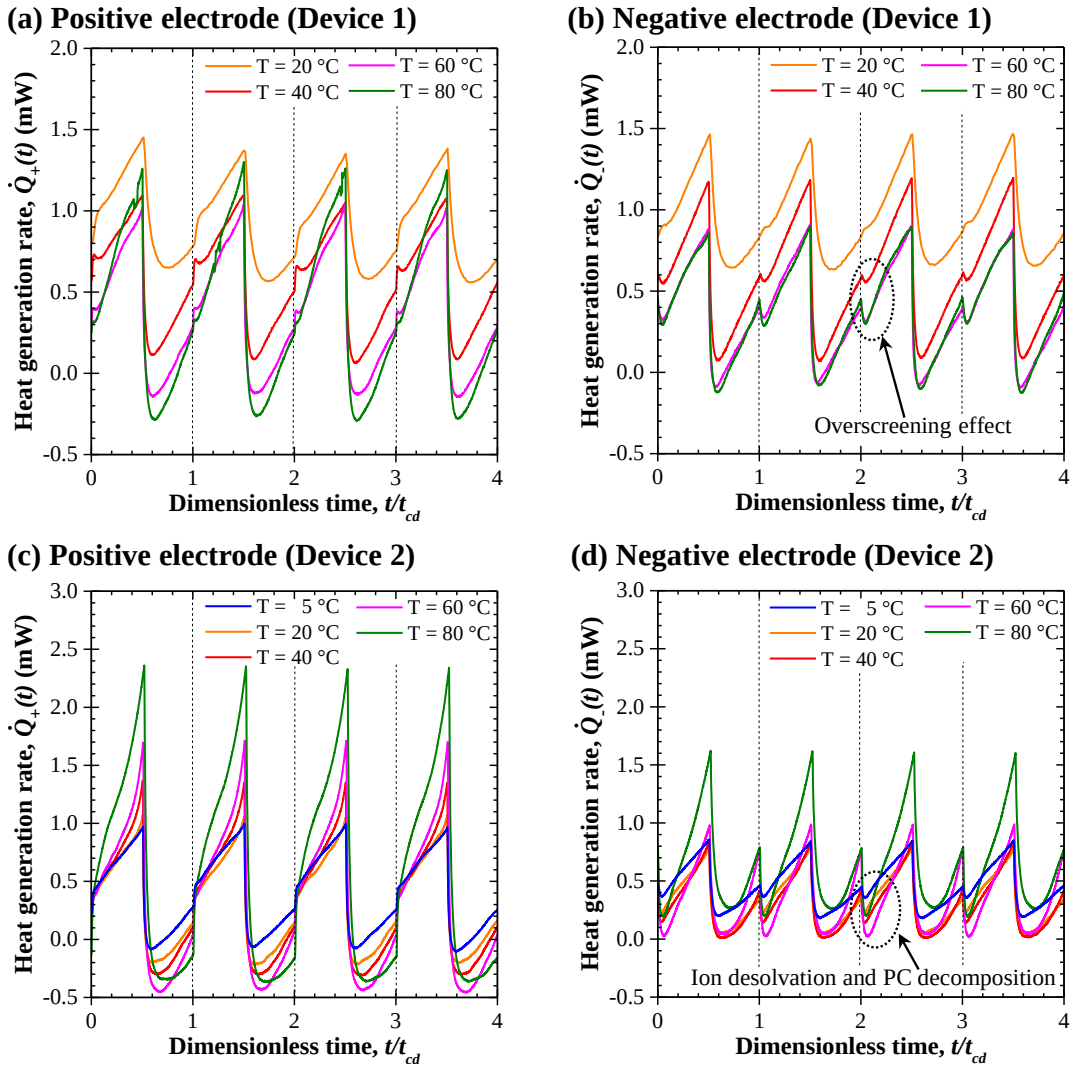

Figure 4.8: Instantaneous heat generation rates as functions of dimensionless time t/t_{cd} for Device 1 with neat $Pyr_{14}TFSI$ electrolyte (a) $\dot{Q}_+(t)$ at the positive and (b) $\dot{Q}_-(t)$ at negative electrodes and for Device 2 with 1 M $Pyr_{14}TFSI$ in PC electrolyte (c) $\dot{Q}_+(t)$ at the positive and (d) $\dot{Q}_-(t)$ at negative electrodes for temperatures between 5 and 80 °C during four consecutive galvanostatic cycles under constant current $I = 4$ mA.

4.3.5 Time-averaged irreversible heat generation rates

Figures 4.9 and 4.10 plot the time-averaged irreversible heat generation rates (a) $\bar{\dot{Q}}_{irr,+}$ at the positive electrode, (b) $\bar{\dot{Q}}_{irr,-}$ at the negative electrode, (c) $\bar{\dot{Q}}_{irr,T}$ in the entire cell, and (d) the ratio $\bar{\dot{Q}}_{irr,T}/\bar{\dot{Q}}_J$ of total irreversible heat generation rate to Joule heating as functions of I^2 with imposed current I ranging from 1 to 5 mA and temperature T varying between 5 and 80 °C for Device 1 and Device 2, respectively. The error bars correspond to two standard deviation or 95% confidence interval estimated by evaluating $\bar{\dot{Q}}_{irr,i}$ over five consecutive galvanostatic cycles. In addition, Joule heating was estimated as

$$\bar{\dot{Q}}_J = \bar{R}_s(T) I^2 \tag{4.7}$$

where $\bar{R}_s(T)$ is the average internal resistance reported in Figure 4.6, except for Device 2 at 80 °C when variations in $R_s(T)$ with imposed current I were accounted for.

Figures 4.9 and 4.10 indicate that $\bar{\dot{Q}}_{irr,+}$ and $\bar{\dot{Q}}_{irr,-}$ were fairly similar in each device and for any given temperature. This was attributed to the fact that (i) the positive and negative electrodes were synthesized in the same manner and should be nearly identical and (ii) the diffusion coefficients of Pyr_{14}^+ cations and $TFSI^-$ anions were similar in each electrolyte considered [45, 105, 123, 143]. In fact, the ratio of the diffusion coefficients of Pyr_{14}^+ to that of $TFSI^-$ in neat $Pyr_{14}TFSI$, i.e., D_+/D_- was reported to be equal to 1.2 at 20 °C and 1.1 at 40 °C [143] and approaching 1.0 as the temperature increases [45]. Similarly, in Device 2 (Figure 4.10), $D_+ \approx D_-$ in 1 M of $Pyr_{14}TFSI$ dissolved in PC at 20 °C [105, 123]. Therefore, the ionic conductivity of the electrolyte in each half cell were similar at all temperatures in each device. The slight differences between $\bar{\dot{Q}}_{irr,+}$ and $\bar{\dot{Q}}_{irr,-}$ could be due to differences in the electrode mass loading. In addition, the irreversible heat generation rates $\bar{\dot{Q}}_{irr,+}$ and $\bar{\dot{Q}}_{irr,-}$ in Device 2 were typically

smaller than those in Device 1 due, in part, to its smaller internal resistance R_s (Figure 4.6).

Moreover, Figure 4.9 establishes that the time-averaged irreversible heat generation rates $\bar{\dot{Q}}_{irr,+}$ and $\bar{\dot{Q}}_{irr,-}$ at the positive and negative half-cells as well as $\bar{\dot{Q}}_{irr,T}$ in the entire Device 1 decreased significantly with increasing temperature from 5 to 80 °C. This was due, in part, to the fact that the ionic conductivity of neat $Pyr_{14}TFSI$ and the wettability of the electrodes increased sharply with increasing temperature. By contrast, Figure 4.10 establishes that $\bar{\dot{Q}}_{irr,+}$, $\bar{\dot{Q}}_{irr,-}$, and $\bar{\dot{Q}}_{irr,T}$ in Device 2 decreased slightly between 5 and 20 °C and were nearly independent of temperature between 20 to 60 °C for any given current. These observations are surprising given the decrease in internal resistance $\bar{R}_s(T)$ of Device 2 with increasing temperature from 5 to 60 °C [Figure 4.6(b)]. It suggested that Joule heating was not the only source of irreversible heat generation. However, $\bar{\dot{Q}}_{irr,+}$, $\bar{\dot{Q}}_{irr,-}$, and $\bar{\dot{Q}}_{irr,T}$ increased significantly at 80 °C in Device 2 due to the partial PC decomposition resulting in electrode pore blockage [51, 81] and increasing cell resistance [Figure 4.6(b)].

Furthermore, $\bar{\dot{Q}}_{irr,+}$, $\bar{\dot{Q}}_{irr,-}$, and $\bar{\dot{Q}}_{irr,T}$ in EDLCs with aqueous and organic electrolytes at 20 °C [87, 88] and in IL-based electrolyte between 20 to 60 °C [76] all for cell potential window $\Delta\psi_s \leq 1$ V were linearly proportional to I^2. In fact, the total heat generation rate $\bar{\dot{Q}}_{irr,T}$ was equal to Joule heating, i.e., $\bar{\dot{Q}}_J = R_s I^2$. By contrast, $\bar{\dot{Q}}_{irr,+}$, $\bar{\dot{Q}}_{irr,-}$, and $\bar{\dot{Q}}_{irr,T}$ in both Devices 1 and 2 with $\Delta\psi_s = 2.5$ V did not vary linearly with I^2, as indicated by power law fit. In fact, the total irreversible heat generation rate $\bar{\dot{Q}}_{irr,T}$ in both Devices 1 and 2 exceeded Joule heating $\bar{\dot{Q}}_J$ for any temperatures between 5 and 80 °C, i.e., $\bar{\dot{Q}}_{irr,T}/\bar{\dot{Q}}_J > 1$. The ratio $\bar{\dot{Q}}_{irr,T}/\bar{\dot{Q}}_J$ increased with increasing temperature and decreasing current in both Devices 1 and 2. Similar results were also observed in similar devices cycled at 20 °C under large potential windows $\Delta\psi_s$ up to 4 V [90]. This can be attributed to a combination of phenomena namely (i) the charge redistribution in porous

electrodes caused by higher ions desorption rate with increasing temperature and modeled as the leakage current flowing through the pore resistance [63,74,77,80,90] and (ii) the longer charging-discharging time t_{cd} at low current (Figure 4.5). In fact, the pore resistance is responsible for EDLC self-discharge and increased with increasing potential window [77, 90, 144, 145].

4.3.6 Reversible heat generation rates

As previously discussed, the instantaneous irreversible heat generation rate $\dot{Q}_{irr,i}(t)$ cannot be solely attributed to Joule heating and may vary with time. Thus, the instantaneous reversible heat generation rate $\dot{Q}_{rev,i}(t) = \dot{Q}_i(t) - \dot{Q}_{irr,i}(t)$ cannot be estimated from our measurements. Instead, Figure 4.11 shows the time-averaged reversible heat generation rates during a charging step [Equation 4.6] (a,c) $\bar{\dot{Q}}^c_{rev,+}$ at the positive electrode and (b,d) $\bar{\dot{Q}}^c_{rev,-}$ at the negative electrode as functions of current I for (a,b) Device 1 and (c,d) Device 2, respectively. Here also, the current I ranged from 1 to 5 mA and the temperature T from 5 to 80 °C and the error bars correspond to 95% confidence interval estimated by evaluating $\bar{\dot{Q}}^c_{rev,i}$ over five cycles. Figure 4.11 indicates that, in both Devices 1 and 2, $\bar{\dot{Q}}^c_{rev,+}$ was systematically larger than $\bar{\dot{Q}}^c_{rev,-}$. This could be attributed to the fact that $TFSI^-$ anions are smaller ($\sim$ 0.7 nm) than Pyr^+_{14} cations ($\sim$ 1.1 nm). In fact, d'Entremont et al. [85] established theoretically that adsorption of smaller ions at a given electrode resulted not only in larger integral capacitance but also in larger reversible heat generation rate. Thus, $TFSI^-$ adsorption at the positive electrode during charging caused more reversible heat generation than Pyr^+_{14} adsorption at the negative electrode in Device 1 with neat $Pyr_{14}TFSI$. Similar arguments apply to Device 2 where solvated PC-Pyr^+_{14} ions were significantly larger than $TFSI^-$ ions in the 1 M $Pyr_{14}TFSI$ in PC electrolyte [85].

Moreover, for any given current and temperature, $\bar{\dot{Q}}^c_{rev,+}$ was typically larger in Device 2 than in Device 1 due to the fact that the capacitance of Device 2

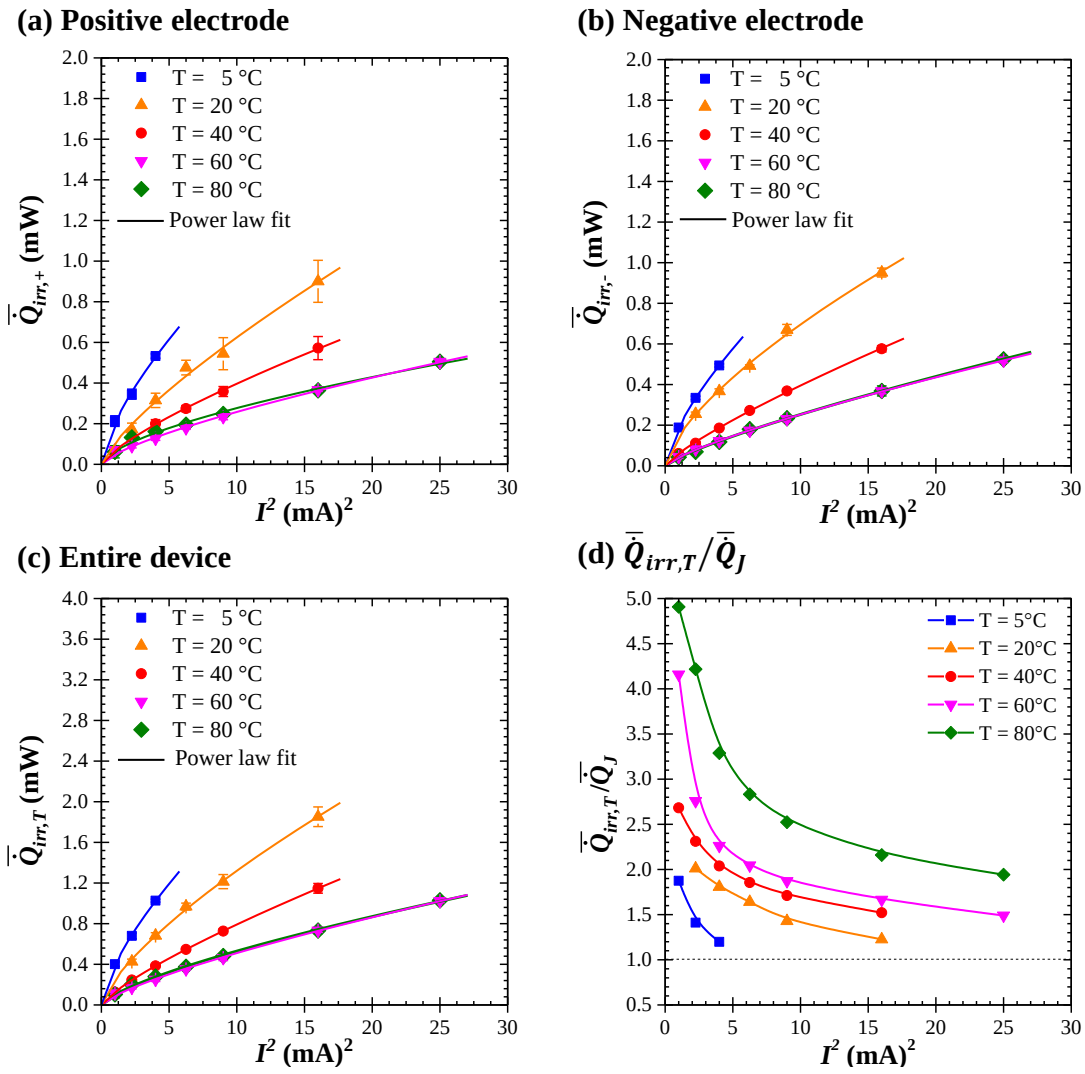

Figure 4.9: Time-averaged irreversible heat generation rates (a) $\bar{\dot{Q}}_{irr,+}$ at the positive electrode, (b) $\bar{\dot{Q}}_{irr,-}$ at the negative electrode, (c) $\bar{\dot{Q}}_{irr,T}$ in the entire cell, and (d) $\bar{\dot{Q}}_{irr,T}/\bar{\dot{Q}}_J$ the ratio of total irreversible heat generation rate to Joule heating as functions of I^2 with imposed current I ranging from 1 to 5 mA for Device 1 with neat $Pyr_{14}TFSI$ electrolyte.

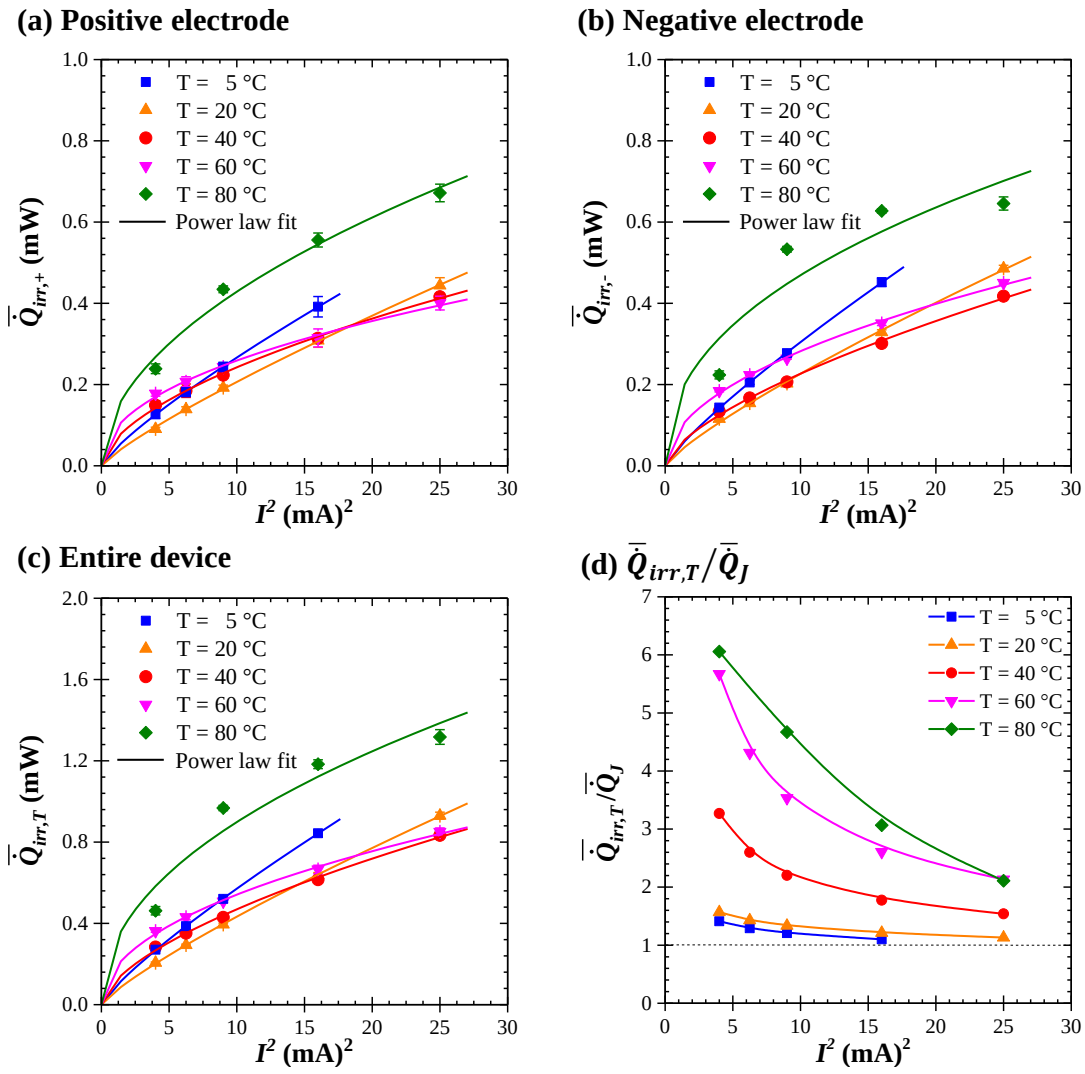

Figure 4.10: Time-averaged irreversible heat generation rates (a) $\bar{\dot{Q}}_{irr,+}$ at the positive electrode, (b) $\bar{\dot{Q}}_{irr,-}$ at the negative electrode, (c) $\bar{\dot{Q}}_{irr,T}$ in the entire cell, and (d) $\bar{\dot{Q}}_{irr,T}/\bar{\dot{Q}}_J$ the ratio of total irreversible heat generation rate to Joule heating as functions of I^2 with imposed current I ranging from 1 to 5 mA for Device 2 with 1 M $Pyr_{14}TFSI$ in PC electrolyte.

was significantly larger than that of Device 1 (Figures 4.3 and 4.7). By contrast, $\bar{\dot{Q}}^c_{rev,-}$ in Device 2 was smaller than in Device 1 as solvated PC-Pyr^+_{14} cations were larger compared to non-solvated Pyr^+_{14} cations in neat IL.

Figures 4.11(a) and 4.11(b) also establish that, for a given current in Device 1, $\bar{\dot{Q}}^c_{rev,+}$ increased with increasing temperature whereas $\bar{\dot{Q}}^c_{rev,-}$ generally did not change significantly with temperature. This could be due to the endothermic dip previously observed in $\dot{Q}_-(t)$ at the negative electrode and associated with overscreening effect, ion desolvation, and/or PC decomposition. Indeed, the magnitude of this endothermic dip increased with increasing temperature and compensate the rise in reversible heat generation caused by increasing capacitance.

Furthermore, in Device 1 with neat Pyr_{14}TFSI [Figures 4.11(a) and 4.11(b)], both $\bar{\dot{Q}}^c_{rev,+}$ and $\bar{\dot{Q}}^c_{rev,-}$ increased linearly with imposed current I for all temperatures considered. This was consistent with results from numerical simulations of EDLCs [84]. Similar observations were also made in previous experimental studies for EDLC cells consisting of AC-electrodes with organic or aqueous electrolytes for potential window $\Delta\psi_s \leq 1$ V [87, 88] and with neat or diluted Pyr_{14}TFSI electrolyte for different potential windows between 1 V to 4 V at 20 °C [90]. Similarly, in Device 2 with 1 M Pyr_{14}TFSI diluted in PC [Figures 4.11(c) and 4.11(d)], $\bar{\dot{Q}}^c_{rev,+}$ and $\bar{\dot{Q}}^c_{rev,-}$ increased fairly linearly with imposed current I except for temperatures $T = 60$ and 80 °C. This was due to the fact that the endothermic dip in the instantaneous heat generation rate at the negative electrode [Figure 4.8(d)] attributed to overscreening effect and/or desolvation of Pyr^+_{14} from PC solvent shell and PC decomposition became significant at 60 and 80 °C.

4.4 Chapter summary

This chapter reported the irreversible and reversible heat generation rates in two sets of AC-based EDLC devices with either (i) neat Pyr_{14}TFSI or (ii) 1 M

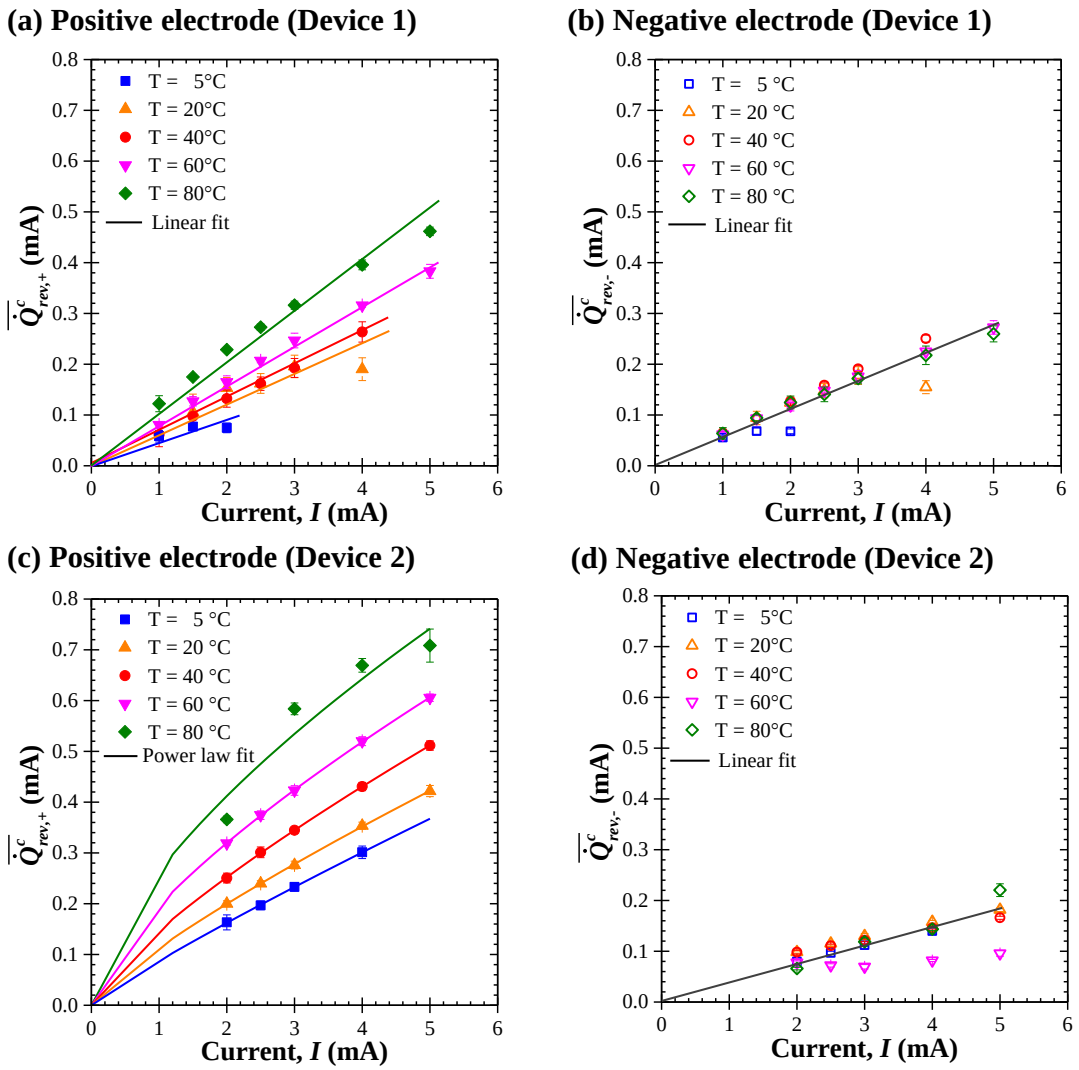

Figure 4.11: Time-averaged reversible heat generation rates during the charging step as functions of imposed current I ranging between 1 and 5 mA for Device 1 with neat $Pyr_{14}TFSI$ electrolyte (a) $\bar{\dot{Q}}^c_{rev,+}$ at the positive and (b) $\bar{\dot{Q}}^c_{rev,-}$ at negative electrodes and for Device 2 with 1 M $Pyr_{14}TFSI$ in PC electrolyte (c) $\bar{\dot{Q}}^c_{rev,+}$ at the positive and (d) $\bar{\dot{Q}}^c_{rev,-}$ at negative electrodes for temperatures between 5 and 80 °C.

$Pyr_{14}TFSI$ in PC electrolytes. The measurements were performed in an isothermal *in operando* calorimeter under galvanostatic cycling with potential window of 2.5 V and temperatures ranging from 5 to 80 °C. The instantaneous heat generation rate at each electrode was measured under galvanostatic cycling at temperatures between 5 and 80 °C for a potential window of 2.5 V. First, the instantaneous heat generation rate was similar at each electrode in neat IL. By contrast, it was smaller at the negative electrode than at the positive electrode in devices with diluted IL in PC. Large oscillations in the instantaneous heat generation rate were observed due to reversible processes such as ion adsorption/desorption and ion solvation/desolvation. In addition, endothermic dips appeared and grew with increasing temperature above 60 °C at the negative electrode at the beginning of the charging step. They were attributed to (i) overscreening effects in both electrolytes as well as to (ii) desolvation of Pyr_{14}^{+} cations and (iii) partial decomposition of PC in diluted IL electrolyte. Moreover, the irreversible heat generation rate in both devices decreased with increasing temperature due to the significant increase in the electrolyte ionic conductivity, particularly for the device with neat $Pyr_{14}TFSI$ electrolyte. The irreversible heat generation rates in the device with 1 M $Pyr_{14}TFSI$ in PC increased sharply at 80 °C as a result of PC decomposition. In addition, the total irreversible heat generation rate in each device exceeded Joule heating. This was attributed to additional irreversible heat generation caused by charge redistribution in the porous electrode and increasing leakage current due to ion desorption with increasing temperature. Second, in both EDLC devices, the time-averaged reversible heat generation rate over the charging step increased with increasing temperature and was larger at the positive than at the negative electrode due to the better accessibility of smaller $TFSI^{-}$ anions into subnanoscale pores compared with larger Pyr_{14}^{+} cations. Furthermore, the time-averaged reversible heat generation rate during charging at both electrodes increased linearly with imposed current except in the device with IL diluted in PC above 60 °C.

CHAPTER 5

Heat generation in all-solid-state supercapacitors with graphene electrodes and gel electrolytes

The chapter aims to investigate instantaneous heat generation rate in graphene-based all-solid-state supercapacitors with either conventional or redox-active gel electrolytes under galvanostatic cycling. It also aims to gain insights into the charging mechanism and also to quantify the heat generation for further design of the packaging to achieve adequate thermal comfort for flexible and wearable all-solid-state supercapacitors.

5.1 Materials and methods

5.1.1 Sample preparation

Electrode fabrication

Sheets of commercial buckypaper (Nanocomp Technologies, Inc., USA) with surface area 1.5×0.6 cm^2 were used as substrates to grow graphene petals (GPs) by microwave plasma chemical vapor deposition (MPCVD), as described in previous studies [146–148]. Buckypaper serves as a flexible, light, and mechanically robust substrate for GP growth. The buckypaper samples were elevated 9 mm above a 55 mm diameter molybdenum puck by ceramic spacers and then subjected to MPCVD conditions with H_2 (50 sccm, standard cubic centimeters per minute) and CH_4 (10 sccm) as the primary feed gases. During GP growth, the total pressure and plasma power were maintained at 30 Torr and 600 W, respectively. The growth time was 25 min. The mass loading of GPs on each electrode was

measured by subtracting the weight of the original buckypaper (BP) (i.e., 1.96 mg/cm^2) from the final weight of each electrode.

Polymer gel electrolyte preparation

Two types of gel electrolytes were prepared: (i) 1 M H_3PO_4-PVA as a conventional gel electrolyte and (ii) 0.02 M $K_3Fe(CN)_6$-$K_4Fe(CN)_6$-PVA as a redox-active gel electrolyte. First, to prepare the PVA solution, 4 g of PVA powder (molecular weight 89,000-98,000 g/mol, 99%, hydrolyzed, Sigma-Aldrich) was dissolved in 40 ml of deionized water, and the resulting solution was subjected to continuous stirring for 20 min at 85 °C in a water bath.

For preparing H_3PO_4-PVA gel electrolyte, 4 g of concentrated liquid H_3PO_4 solution (85 wt.% in H_2O, 99% trace metals basis, Sigma-Aldrich) was added to 40 ml of the previously prepared PVA solution. For synthesizing the redox-active gel electrolyte, $K_3Fe(CN)_6$-$K_4Fe(CN)_6$-PVA (denoted by PFC-PVA), 0.329 g of $K_3Fe(CN)_6$ powder (molecular weight 329.26 g/mol, 99%, Sigma-Aldrich) and 0.422 g of $K_4Fe(CN)_6$ powder (molecular weight 422.39 g/mol, 99%, Sigma-Aldrich) were dissolved in 10 ml DI water to prepare a 0.1 M $K_3Fe(CN)_6$/$K_4Fe(CN)_6$ solution (PFC solution). Then, the aqueous PFC solution was added to 40 ml of the previously prepared PVA solution to create 0.02 M PFC-PVA solution. For both gel electrolytes, 5 ml of the solutions were allowed to cool to room temperature. The resulting homogeneous viscous solution was drop-casted onto a polytetrafluoroethylene (PTFE) evaporating dish and allowed to dry at room temperature for 24 hours. Finally, dried free-standing electrolyte films about 100 μm in thickness were cut into small pieces matching the size of the GP/BP electrodes.

Device assembly

To fabricate an all-solid-state supercapacitor, a clean paintbrush was dipped into the desired gel electrolyte solution and applied on two identical GP/BP electrodes. The electrodes were left to dry for about 45 min before the procedure was repeated twice. The objective of the initial coating and drying process was to achieve a complete coverage of the porous electrodes by the electrolyte and good adhesion between the electrode and the solid electrolyte film. After the third application, the device was assembled by sandwiching the gel electrolyte film between two identical GP/BP electrodes. Then, the device was placed between two glass microscope slides of dimensions 2.5×7.5 cm^2 and pressure was applied with a small paper clip on each end of the slides. The assembled device was left at room temperature for 1 hour prior to experimental measurements in order to evaporate the excess water.

Figure 5.1 illustrates the final appearance of the all-solid-state supercapacitor devices assembled in this study along with typical dimensions. Table 5.1 summarizes the composition of the gel electrolyte, length, width, and graphene (GP) mass loading of each electrode in the four devices assembled. The cross-sectional area and the thickness of Devices 2, 3, and 4 were identical and equal to (1.4×0.6 cm^2) while the cross-sectional area of Device 1 was slightly smaller (1.1×0.6 cm^2).

Table 5.1: Gel electrolyte composition, footprint and mass loading of graphene petals (GP) on buckypaper for the four devices investigated.

Device	**Gel electrolyte**	**Footprint**	**Mass loading of GP electrodes**	
		L × W	positive	negative
1	1 M H_3PO_4-PVA	1.1 cm × 0.6 cm	3.98 mg	3.06 mg
2	1 M H_3PO_4-PVA	1.4 cm × 0.6 cm	3.85 mg	4.53 mg
3	0.02 M $K_3Fe(CN)_6$-$K_4Fe(CN)_6$-PVA	1.4 cm × 0.6 cm	4.55 mg	3.83 mg
4	0.02 M $K_3Fe(CN)_6$-$K_4Fe(CN)_6$-PVA	1.4 cm × 0.6 cm	2.65 mg	2.87 mg

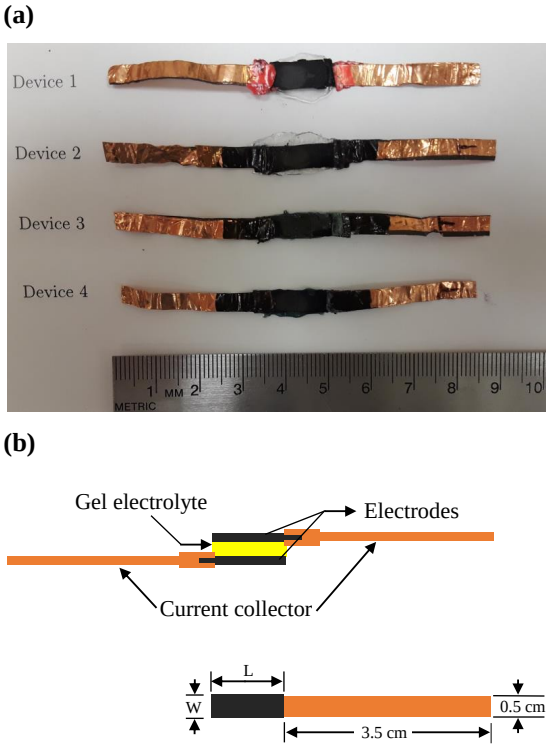

Figure 5.1: (a) Photograph of the four devices considered in this study, (b) side and top views of device's assembly, consisting of solid gel electrolyte, MPCVD GP on buckypaper electrodes, current collectors, and associated dimensions (see Table 5.1).

5.1.2 Isothermal Calorimeter

In this study, instantaneous heat generation rates were measured in Devices 1 to 4 under galvanostatic cycling using a custom-made isothermal calorimeter previously described [87]. The calorimeter can measure the time-dependent heat generation rate in each electrode of an electrochemical cell separately with high accuracy (± 10 μW) and with uncertainty under 3% [87].

Based on the thermal analysis of a single electrode described in supplementary material of Ref. [87], the time-dependent heat generation rate $\dot{Q}_i(t)$ (in mW) at each electrode is equal to the heat transfer rate $q_i''(t)$ passing through the heat

flux sensor such that [87],

$$\dot{Q}_i(t) = q_i''(t)A_i = \frac{\Delta V_i(t)}{S_i}A_i \qquad \text{with } i = \ + \text{ or } - \tag{5.1}$$

where A_i denotes the footprint area of the electrode (in cm^2) while S_i is the temperature-dependent sensitivity of the heat flux sensor provided by the manufacturer (in $\mu\mathrm{V}/(\mathrm{W}/\mathrm{m}^2)$) while subscript "$i$" refers to either the positive "+" or negative "−" electrode. Here, $\Delta V_i(t)$ is the voltage difference measured in each heat flux sensor in thermal contact with electrode "i". The instantaneous total heat generation rate in the entire device (denoted by subscript "T") can be expressed as $\dot{Q}_T(t) = \dot{Q}_+(t) + \dot{Q}_-(t)$.

The instantaneous heat generation rate $\dot{Q}_i(t)$ can be decomposed as the sum of the irreversible $\dot{Q}_{irr,i}(t)$ and reversible heat generation rates $\dot{Q}_{rev,i}(t)$, i.e., $\dot{Q}_i(t)$ = $\dot{Q}_{irr,i}(t)$ + $\dot{Q}_{rev,i}(t)$ [87]. The time-averaged heat generation rate over a cycle period t_{cd} corresponds to the time-averaged irreversible heat generation rate $\bar{\dot{Q}}_{irr,i}$ at electrode "i", i.e. [87],

$$\bar{\dot{Q}}_{irr,i} = \frac{1}{t_{cd}} \int_{(n_c-1)t_{cd}}^{n_c t_{cd}} \dot{Q}_i(t)\, dt \qquad \text{with } i = \ + \text{ or } - \tag{5.2}$$

here n_c is the cycle number, chosen to be adequately large so that $\dot{Q}_i(t)$ has reached oscillatory steady state. Indeed, by definition, time-averaging of the reversible heat generation rate $\dot{Q}_{rev,i}(t)$ at electrode "i" over a complete charging-discharging cycle yields $\bar{\dot{Q}}_{rev,i} = 0$.

Finally, in the interest of comparing the reversible heat generation rate at each electrode, the instantaneous reversible heat generation rate $\dot{Q}_{rev,i}(t)$ was averaged

over a charging period t_c of galvanostatic cycling [87],

$$\bar{\dot{Q}}^{c}_{rev,i} = \frac{1}{t_c} \int_{(n_c-1)t_{cd}}^{(n_c-1)t_{cd}+t_c} \dot{Q}_{rev,i}(t)\ dt \qquad \text{with } i = T,\ +,\ \text{or}\ -\,. \tag{5.3}$$

5.1.3 Device characterization

A device's integral capacitance C_{int} (in mF) was evaluated by integrating the area enclosed by the cyclic voltammetry (CV) curve plotting the measured current I (in mA) versus the imposed potential ψ_s (in V) for a given scan rate ν and potential window ranging between ψ_{min} and ψ_{max} as [149],

$$C_{int}(\nu) = \frac{1}{(\psi_{max} - \psi_{min})} \oint \frac{I}{2\nu} d\psi_s. \tag{5.4}$$

Here, the integral capacitances C_{int} of Devices 1 to 4 were obtained for scan rates 5, 10, 20, and 30 mV/s.

Subsequently, galvanostatic cycling was performed on each device, for 20 cycles at constant current I ranging from 1 to 4 mA to reach oscillatory steady state. Table 5.2 summarizes the conditions, namely the potential window $(\psi_{max} - \psi_{min})$ and current I for CV and galvanostatic cycling of each device. The potential window for both CV and galvanostatic cycling was 1.0 V for Device 1, 0.8 V for Device 2, and 1.2 V for Devices 3 and 4. These potential windows were chosen during CV pre-cycling of each device in order to avoid unwanted redox reactions.

Moreover, the internal resistance R_s was evaluated from the IR drop at the charging/discharging transitions under galvanostatic cycling at current I according to [89, 111–113],

$$R_s(I) = \frac{\psi_s(t_c^+) - \psi_s(t_c^-)}{2I} \tag{5.5}$$

where $\psi_s(t_c^+)$ and $\psi_s(t_c^-)$ denote the potential across the device at the end of the charging step and immediately after the beginning of the discharging step,

Table 5.2: Cyclic voltammetry and galvanostatic cycling operating conditions for four devices.

Device	**Cyclic Voltammetry (CV)**	**Galvanostatic cycling**	
	Potential window	Current imposed	Potential window
	ψ_{min} - ψ_{max}	I (mA)	ψ_{min} - ψ_{max}
1	0 - 1.0 V	2.0 − 4.0	0 - 1.0 V
2	0 - 0.8 V	1.0 − 4.0	0 - 0.8 V
3	0 - 1.2 V	1.0 − 4.0	0 - 1.2 V
4	0 - 1.2 V	1.0 − 4.0	0 - 1.2 V

respectively. Here, the IR drop $[\psi_s(t_c^+) - \psi_s(t_c^-)]$ was calculated by considering the cell potential $\psi_s(t_c^-)$ 10 ms after the beginning of the discharging step (i.e. $t_c^- - t_c^+ = 10$ ms), as suggested by Zhao et al. [112].

5.2 Results and discussion

5.2.1 Cyclic voltammetry curves and integral capacitances

Figure 5.2 shows the CV curves at scan rates $\nu = 5$, 10, 20, and 30 mV/s measured for Devices 1 to 4 under the operating conditions listed in Table 5.2. The nearly rectangular CV curves of Devices 1 and 2 featuring conventional gel electrolyte are characteristic of EDLCs behavior. By contrast, Devices 3 and 4 with redox-active gel electrolyte exhibited CV curves with peaks attributed to reversible redox reactions. Here, the redox peaks were observed in the potential range $\psi_s(t) \sim 0$ to 0.4 V corresponding to the Faradaic regime when charging was dominated by redox reactions [150].

Figure 5.3 plots the integral capacitance C_{int}, estimated from CV curves using Equation (5.4), for all four devices as a function of scan rate ν. As expected, the integral capacitance C_{int} of Devices 3 and 4 with redox-active gel electrolyte was about two to three times larger than that of Device 2 with conventional gel electrolyte for the same footprint area, albeit with slightly larger potential windows. This result can be attributed to additional charge storage due to redox reactions

in the redox-active gel electrolyte of $Fe(CN)_6^{3-}/Fe(CN)_6^{4-}$ redox pair. This improvement in C_{int} has also been observed for different redox electrolytes [53–59], as previously discussed. In addition, Figure 4.3 indicates that the integral capacitances C_{int} of all devices decreases with increasing scan rate. The slight decrease of C_{int} in Devices 1 and 2 is consistent with results for EDLC devices with activated carbon electrodes reported in Ref. [87]. However, the decrease in C_{int} for Devices 3 and 4 was steeper than for Devices 1 and 2. This observation is consistent with results for graphene-based solid-state flexible supercapacitor using polymer gel electrolyte with sodium molybdate (Na_2MoO_4) as a redox additive electrolyte [151]. This observation can be attributed to the slow kinetics of the Faradaic reactions in redox-active electrolytes, producing less total charge storage at higher scan rates. In addition, Devices 1 to 4 showed either better or comparable capacitance comparing to some other all-solid-state supercapacitor devices reported in Refs. [20, 152, 153].

5.2.2 Galvanostatic cycling and internal resistances

Figure 5.4 shows the cell potential $\psi_s(t)$ as a function of time t during galvanostatic cycling of Devices 1 to 4 for constant current I ranging from 1 to 4 mA and the same potential windows as for the CV curves (see Figure 5.2). For Devices 1 and 2 [Figures 5.4(a) and 5.4(b)], the cell potential $\psi_s(t)$ varies linearly with time t between the minimum ψ_{min} and maximum ψ_{max} potentials. This result confirms the EDLC behavior of Devices 1 and 2 and the absence of redox reactions. By contrast, for Devices 3 and 4 [Figures 5.4(c) and 5.4(d)] the cell potential $\psi_s(t)$ during galvanostatic cycling did not vary linearly with time t. The cell potential $\psi_s(t)$ features a small slope at the beginning of charging indicating larger differential capacitance $C_{diff} = I/(d\psi_s/dt)$ [154] at the early stage of the charging process from $\psi_s(t) \sim 0$ to 0.4 V. This potential range corresponded to the Faradaic regime when Faradaic reactions dominated [155]. This interpretation is consistent with

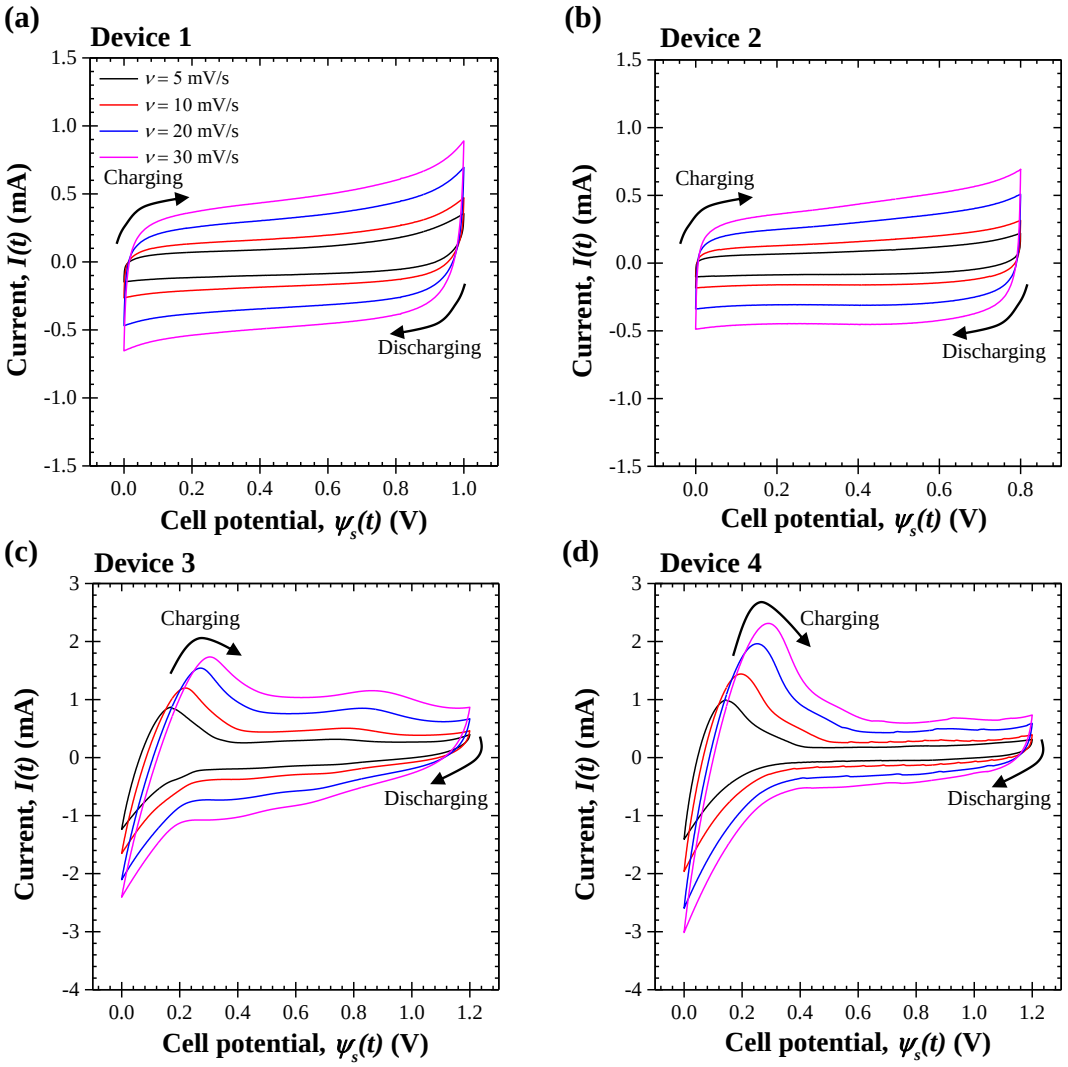

Figure 5.2: Cyclic Voltammetry (CV) curves for (a) Device 1, (b) Device 2, (c) Device 3, and (d) Device 4 for scan rate ν = 5, 10, 20, and 30 mV/s for different potential windows (Table 5.2).

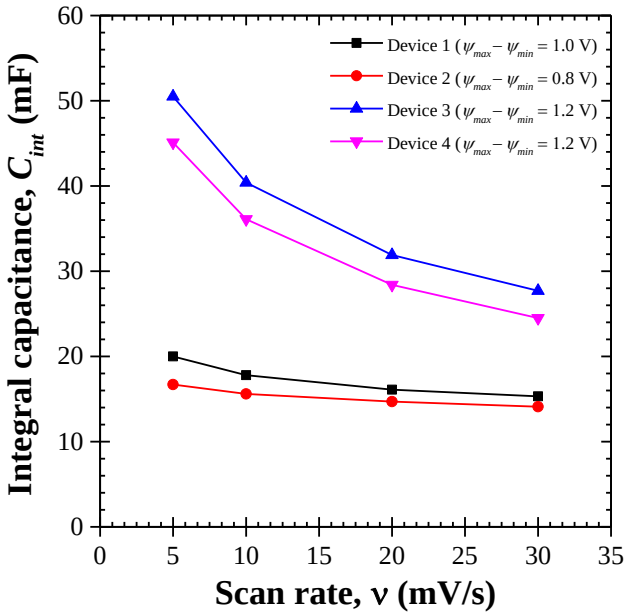

Figure 5.3: Integral capacitance $C_{int}(\nu)$ obtained from CV curves [Equation (5.4)] presented in Figure 4.2 for the four devices investigated as a function of scan rate ν for ν = 5, 10, 20, and 30 mV/s.

observation of the redox peaks in CV curves (Figure 5.2). The larger differential capacitance C_{diff} can be attributed to Faradaic reactions (Faradaic regime) during charging, while the smaller differential capacitance C_{diff} in the second part of the charging process (capacitive regime) from $\psi_s(t) \sim 0.4$ to 1.2 V, can be attributed to EDL formation [155]. Moreover, in all devices, IR drop $[\psi_s(t_c^+) - \psi_s(t_c^-)]$ can be observed at the transition between the end of charging and the beginning of discharging.

Figure 5.5 shows the associated internal resistance R_s of Devices 1 to 4, calculated according to Equation (5.5), as a function of imposed current I. The internal resistance R_s in all four devices was fairly constant regardless of imposed current. However, the internal resistances R_s of Devices 3 and 4 with redox-active gel electrolyte were about five to six times larger than those of Devices 1 and 2. This observation can be attributed to the smaller ionic conductivity of redox-active gel electrolyte due to the much smaller ion concentration (0.02 M PFC-PVA), limited

by solubility of the salts, compared with the ion concentration of the conventional gel electrolyte (1 M H_3PO_4-PVA). Indeed, the ionic conductivity of 0.02 M PFC-PVA gel electrolyte has been reported as 6 mS cm^{-1} by Yang et al. [156] and 5.44 mS cm^{-1} by Kundu et al. [157]. On the other hand, the ionic conductivity of 1 M (1:1) H_3PO_4-PVA gel electrolyte has been reported to be larger than 10 mS cm^{-1} [158]. In addition, the internal resistance of Device 1 was about two times larger than that of Device 2. This observation seems counterintuitive given the fact that mass loading of the negative electrode of Device 2 was about 48% larger than that of Device 1. The larger resistance of Device 1 can be attributed to (i) variations in the drop-casting of the gel electrolyte that may have resulted in larger electrolyte thickness and/or (ii) variations in the device fabrication process due to poorer wetting and lower coverage of the electrode surface by the gel electrolyte. The latter would lead to poor electrical contact between the electrode and the viscous polymer gel electrolyte [159].

5.2.3 Instantaneous heat generation rates

Figure 5.6 shows the temporal evolution of the measured heat generation rates (i) $\dot{Q}_-(t)$ at the negative electrode, (ii) $\dot{Q}_+(t)$ at the positive electrode, and (iii) $\dot{Q}_T(t) = \dot{Q}_+(t) + \dot{Q}_-(t)$ in the entire cell for Devices 1 to 4 as functions of dimensionless time t/t_{cd} for five consecutive galvanostatic cycles under constant current $I = 3$ mA. The results indicate that the heat generation rates in all four devices were repeatable over five consecutive cycles. Note such repeatability is not expected over hundreds or thousands of cycles as the device degrades. However, while the cyclic stability of the redox electrolyte device and its effect on heat generation is certainly important, it falls beyond the scope of the present study. In addition, the heat generation rates $\dot{Q}_-(t)$, $\dot{Q}_+(t)$, and $\dot{Q}_T(t)$ in Devices 3 and 4 were significantly larger than those in Devices 1 and 2 due, in part, to their larger internal resistance R_s (Figure 5.5).

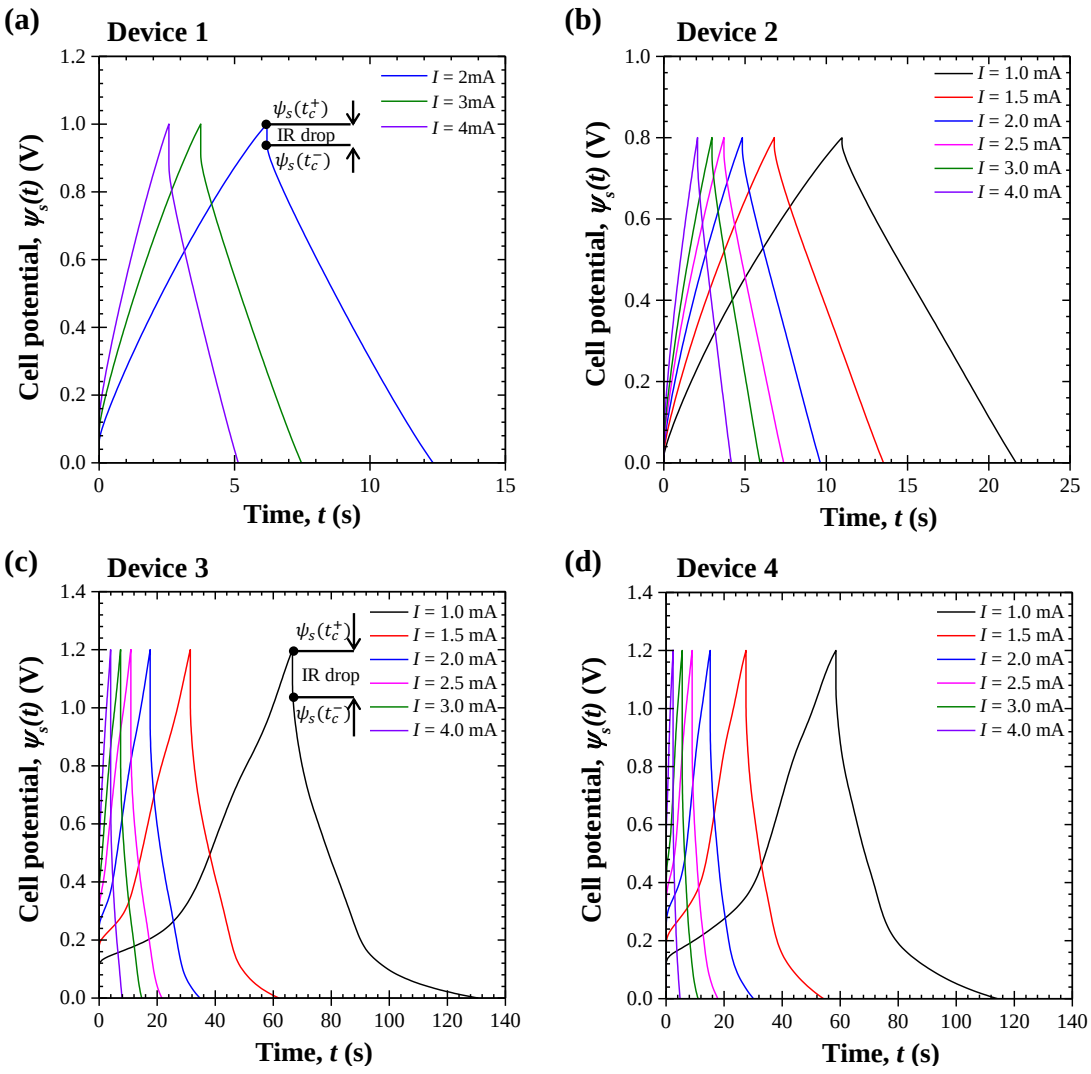

Figure 5.4: Cell potential under galvanostatic cycling for (a) Device 1, (b) Device 2, (c) Device 3, and (d) Device 4 under imposed current I between 1 and 4 mA for different potential windows (Table 5.2).

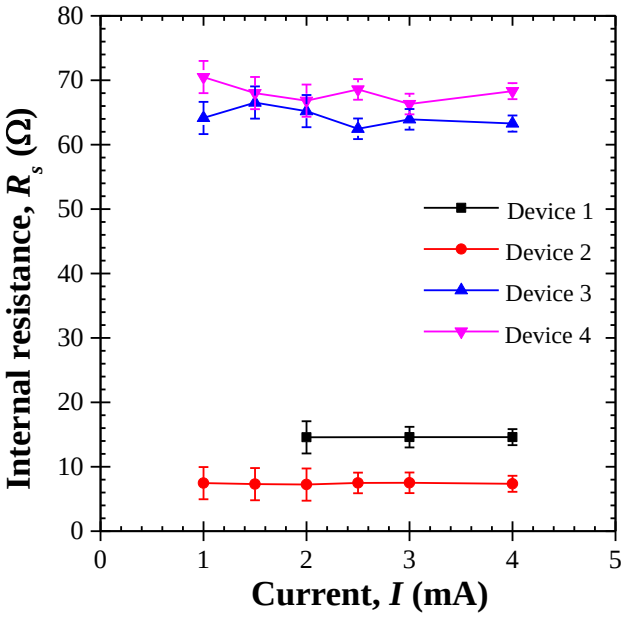

Figure 5.5: Internal resistance R_s as a function of imposed current I for Devices 1 to 4 determined from Equation (6) based on the IR drop shown in Figure 5.4.

Moreover, $\dot{Q}_-(t)$, $\dot{Q}_+(t)$, and $\dot{Q}_T(t)$ in Device 1 was systematically larger than in Device 2 despite having similar capacitances because Device 1 had a larger internal resistance R_s and was cycled over a larger potential window (ψ_{max} - ψ_{min}) compared to Device 2. Furthermore, in both Devices 1 and 2, the heat generation rate at the positive electrode $\dot{Q}_+(t)$ was slightly larger than that at the negative electrode $\dot{Q}_-(t)$. This asymmetry in the heat generation rate at the positive and negative electrodes can be attributed to differences in charging mechanisms between the electrodes due to overscreening effect caused by negatively charged functional group on graphene electrodes, as observed also in activated carbon electrodes with CMC binder [88].

Finally, despite having the same electrode and electrolyte compositions, and similar capacitance and internal resistance, the heat generation rates $\dot{Q}_-(t)$ and $\dot{Q}_+(t)$ were significantly different in Devices 3 and 4 due to larger mass loading of GPs on the positive and negative electrodes of Device 3 than those of Device

4. The larger electrode/electrolyte interfacial area for charge storage produces higher heat generation rate.

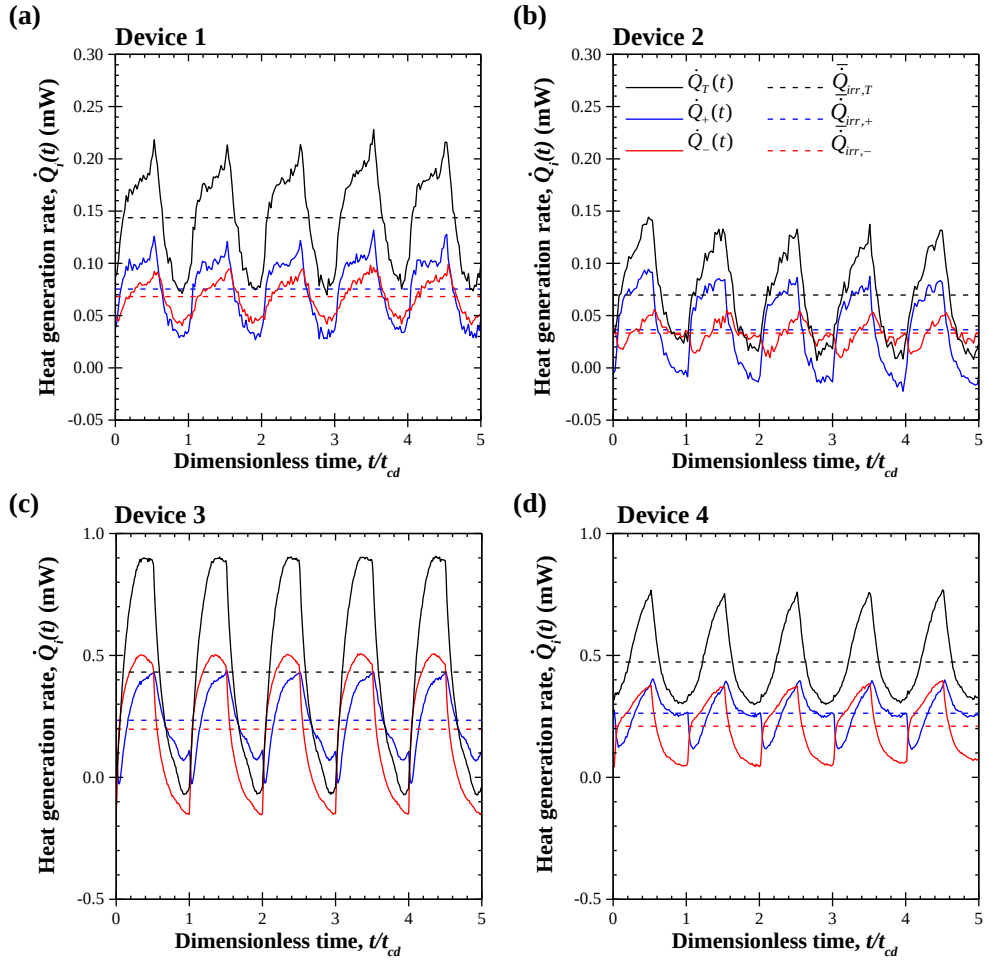

Figure 5.6: Instantaneous heat generation rates $\dot{Q}_+(t)$, $\dot{Q}_-(t)$, and $\dot{Q}_T(t)$ and their time-averaged heat generation rates $\bar{\dot{Q}}_+(t)$, $\bar{\dot{Q}}_-(t)$, and $\bar{\dot{Q}}_T(t)$ at the positive and negative electrodes and for the entire cell for (a) Device 1, (b) Device 2, (c) Device 3, and (d) Device 4 under constant current cycling at $I = 3$ mA for potential windows (ψ_{max} - ψ_{min}) of 1.0 V, 0.8 V, 1.2 V, and 1.2 V, respectively (see Table 2).

5.2.4 Time-averaged heat generation rates

Figure 5.7 shows the time-averaged irreversible heat generation rates (i) $\bar{\dot{Q}}_{irr,-}$ at the negative electrode, (ii) $\bar{\dot{Q}}_{irr,+}$ at the positive electrode, and (iii) $\bar{\dot{Q}}_{irr,T} =$

$\bar{\dot{Q}}_{irr,-} + \bar{\dot{Q}}_{irr,+}$ in the entire cell, represented by dashed lines. The time-averaged irreversible total heat generation rate $\bar{\dot{Q}}_{irr,T}$ in Device 1 was larger than in Device 2 due to its larger internal resistance R_s (Figure 5.5), as previously discussed. On the other hand, despite differences in the instantaneous heat generation rates, the time-averaged total heat generation rate $\bar{\dot{Q}}_{irr,T}$ was similar in Devices 3 and 4 as their internal resistance R_s was comparable (Figure 5.5).

Figure 5.7 plots the time-averaged irreversible heat generation rates $\bar{\dot{Q}}_{irr,-}$, $\bar{\dot{Q}}_{irr,+}$, and $\bar{\dot{Q}}_{irr,T}$ as functions of I^2 for Devices 1 to 4 under constant current cycling. It also shows the heat generation rate due to Joule heating expressed as $\bar{\dot{Q}}_J = I^2 R_s$, where R_s is the average internal resistance for each devices obtained from their IR drop (Figure 5.5). The measured total irreversible heat generation rate $\bar{\dot{Q}}_{irr,T}$ under galvanostatic cycling was in excellent agreement with Joule heating $\bar{\dot{Q}}_J = I^2 R_s$ for all four devices considered. In other words, Joule heating was the only cause of irreversible heat generation in the all-solid-state supercapacitors considered, including those with redox-active gel electrolytes. In addition, the time-averaged heat generation rates $\bar{\dot{Q}}_{irr,-}$ and $\bar{\dot{Q}}_{irr,+}$ at the negative and positive electrodes were also linearly proportional to I^2, and the coefficient of proportionality corresponded to their respective resistances R_- and R_+. In fact, for all four devices tested, Figure 5.7 indicates that the two electrodes had similar resistances whose sum corresponds to the device internal resistance, i.e., $R_- \approx R_+$ and $R_- + R_+ \approx R_s$. Similar results were obtained previously with EDLCs with activated carbon electrodes of various compositions and with different electrolytes [87, 88].

5.2.5 Reversible heat generation rates

Conventional gel electrolyte

As previously demonstrated, Joule heating is the sole cause of irreversible heat generation. Thus, under constant current cycling, the instantaneous irreversible

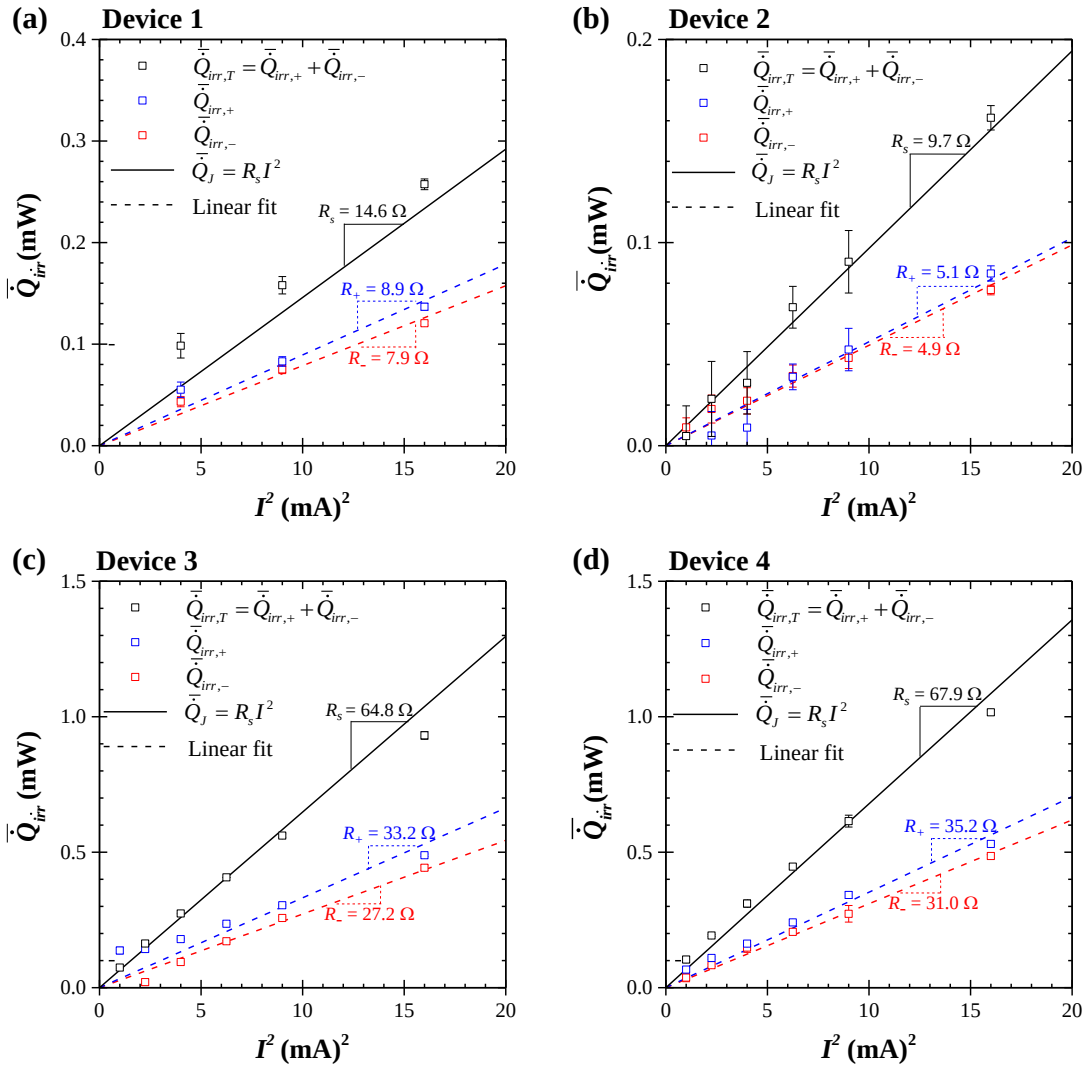

Figure 5.7: Time-averaged heat generation rates $\bar{\dot{Q}}_{irr,-}$, $\bar{\dot{Q}}_{irr,+}$, and $\bar{\dot{Q}}_{irr,T}$ under galvanostatic cycling as functions of I^2 for current I ranging between 2 and 4 mA for (a) Device 1, (b) Device 2, (c) Device 3, and (d) Device 4. Heat generation rate $\bar{\dot{Q}}_J = I^2 R_s$ due to Joule heating and linear fits of $\bar{\dot{Q}}_{irr,-}$ and $\bar{\dot{Q}}_{irr,+}$ are also shown.

heat generation rate $\dot{Q}_{irr,i}(t)$ remains time-independent so that $\dot{Q}_{irr,i}(t) = \bar{\dot{Q}}_{irr,i} = R_i I^2$. Therefore, the instantaneous reversible heat generation rate $\dot{Q}_{rev,i}(t)$ at each electrode or in the entire device can be calculated by subtracting the time-averaged irreversible heat generation rate $\bar{\dot{Q}}_{irr,i}$ from the instantaneous heat generation rate $\dot{Q}_i(t)$, i.e.,

$$\dot{Q}_{rev,i}(t) = \dot{Q}_i(t) - \bar{\dot{Q}}_{irr,i} \qquad \text{with } i = -,\ +,\ \text{or } T. \tag{5.6}$$

Figure 5.8 shows the instantaneous reversible heat generation rates (a) $\dot{Q}_{rev,+}(t)$ at the positive electrode, (b) $\dot{Q}_{rev,-}(t)$ at the negative electrode, and (c) $\dot{Q}_{rev,T}(t)$ in the entire cell estimated by Equation (5.6) for Devices 1 and 2 for current I ranging from 2 to 4 mA. The reversible heat generation rate at the positive electrode $\dot{Q}_{rev,+}(t)$ was systematically larger than that at the negative electrode $\dot{Q}_{rev,-}(t)$ for both Devices 1 and 2 and at all imposed current I. At the positive electrode [Figure 5.8(a)], the reversible heat generation rate $\dot{Q}_{rev,+}(t)$ was exothermic during charging and endothermic during discharging for both Devices 1 and 2. Moreover, the magnitude of $\dot{Q}_{rev,+}(t)$ increased slightly with increasing current I. By contrast, at the negative electrode [Figure 5.8(b)], the reversible heat generation rate $\dot{Q}_{rev,-}(t)$ was both endothermic and exothermic during charging and discharging. The trends observed in $\dot{Q}_{rev,+}(t)$ and $\dot{Q}_{rev,-}(t)$ and their differences were consistent with those observed in EDLC devices with activated carbon electrodes containing carboxymethyl cellulose (CMC) binder [87,88]. There, the behavior of $\dot{Q}_{rev,-}(t)$ was explained by the overscreening effect of ions induced by negatively charged functional groups in CMC binder, as previously discussed [88]. Similarly, in graphene-based electrodes, functional groups such as carboxyl ($-$COOH) exist and can dissociate to form negatively charged carboxylic ($-\text{COO}^-$) surface functionalities [160]. The dissociation of $-$COOH into $-\text{COO}^-$ is an irreversible spontaneous process that may occur during device assembly or during the first

charging/discharging cycle. It could not be observed in the highly repeatable and consecutive cycles shown in Figure 5.6. The resulting negatively charged functional groups attracted positively charged H^+ cations from H_3PO_4 gel electrolyte via electrostatic force between opposite charge. In order to charge-balance the inner Helmholtz layer in the electrolyte, another subsequent layer of PO_4^{3-} anions was required [88, 95]. Therefore, at the beginning of the charging step, the negative electrode was first charged by desorption of PO_4^{3-} anion (endothermic) and by H^+ cations adsorption (exothermic) [88,95]. Thus, the endothermic anion desorption present at the electrode/electrolyte interface due to the overscreening effect partially compensated the exothermic cation adsorption during charging at the negative electrode. Therefore, the magnitude of $\dot{Q}_{rev,-}(t)$ was small compared with that of $\dot{Q}_{rev,+}(t)$, at all times. Consequently, the instantaneous reversible heat generation rate in the entire cell $\dot{Q}_{rev,T}(t) = \dot{Q}_{rev,+}(t) + \dot{Q}_{rev,-}(t)$ followed the same trends as $\dot{Q}_{rev,+}(t)$ at all imposed current I [Figure 5.8(c)]. At the transition between charging and discharging steps, there was a sight time lag due to response time of the heat flux sensors (0.7 s to reach 95% of actual value, gSKIN-XP, greenTEG) and thermal mass of the GP/BP electrodes and gel electrolyte in Devices 1 and 2.

Finally, Figure 5.8(d) plots the time-averaged reversible heat generation over a charging step at each electrode $\bar{\dot{Q}}^c_{rev,i}$ as a function of current I for Devices 1 and 2. At the negative electrode, $\bar{\dot{Q}}^c_{rev,-}$ for all currents fell close to 0 mW, indicating a comparable amount of endothermic and exothermic heat generated during a charging step. This result is consistent with $\bar{\dot{Q}}^c_{rev,-}$ of devices with activated carbon electrodes containing CMC binder reported in Ref [88]. However, at the positive electrode, $\bar{\dot{Q}}^c_{rev,+}$ was positive and fairly independent of the imposed current I.

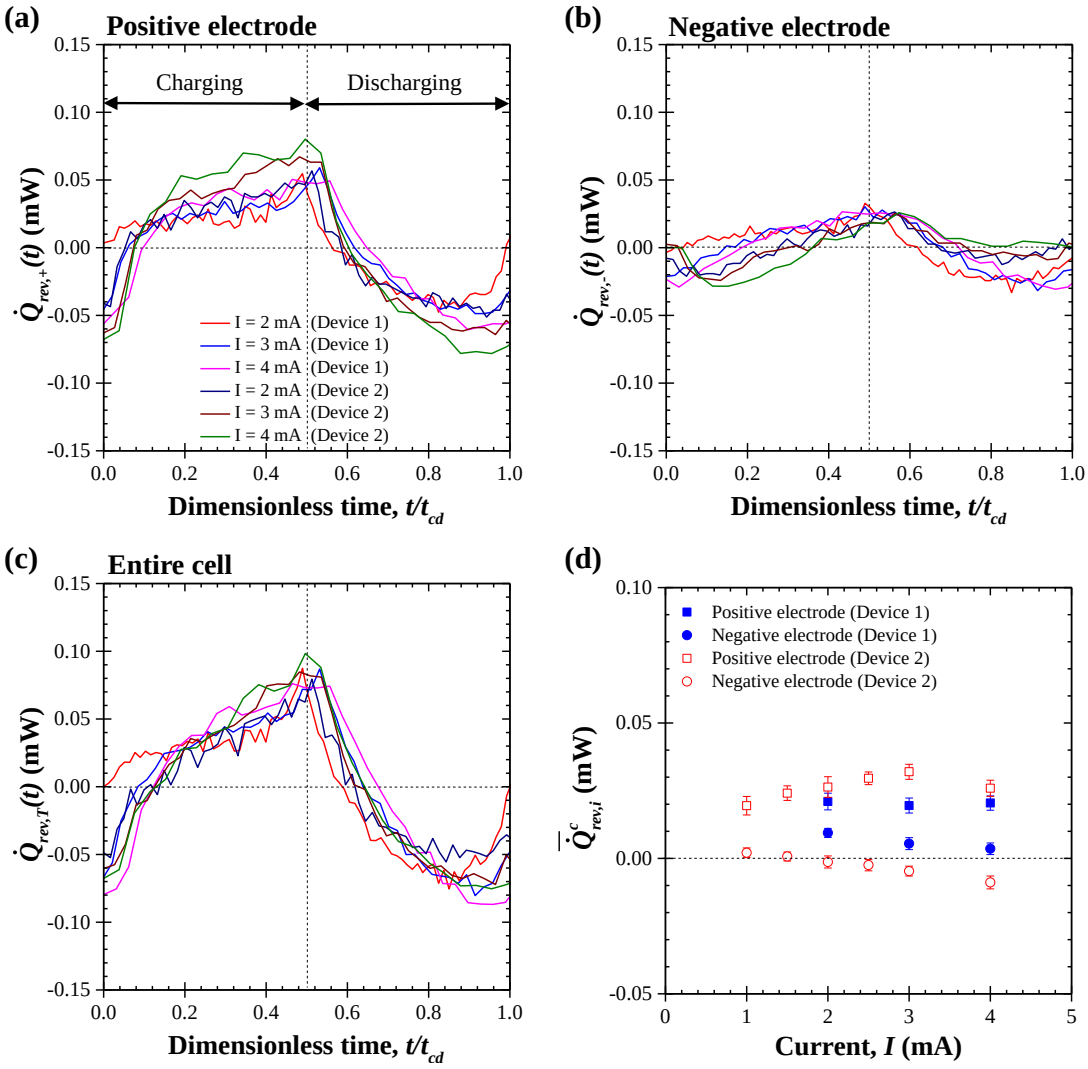

Figure 5.8: One charging-discharging cycle of the reversible heat generation rate (a) $\dot{Q}_{rev,+}(t)$ at the positive electrode, (b) $\dot{Q}_{rev,-}(t)$ at the negative electrode, (c) $\dot{Q}_{rev,T}(t)$ in the entire cell for Devices 1 and 2 as functions of dimensionless time t/t_{cd} for constant current I = 2, 3, and 4 mA. (d) Corresponding time-averaged reversible heat generation rate $\bar{\dot{Q}}^c_{rev,+}$ at the positive and $\bar{\dot{Q}}^c_{rev,-}$ at the negative electrodes during a charging step for Devices 1 and 2.

Redox-active gel electrolyte

Figure 5.9 shows the instantaneous reversible heat generation rates (a) $\dot{Q}_{rev,+}(t)$ at the positive electrode, (b) $\dot{Q}_{rev,-}(t)$ at the negative electrode, and (c) $\dot{Q}_{rev,T}(t)$ in the entire cell estimated by Equation (7) for Devices 3 and 4 for currents I ranging from 2 to 4 mA. At the positive electrode [Figure 5.9(a)], the reversible heat generation rates $\dot{Q}_{rev,+}(t)$ were both endothermic and exothermic during charging and discharging. This can be explained by the combination of two superimposed charging mechanisms at the positive electrode, namely (i) EDL formation and (ii) redox reaction involving $Fe(CN)_6^{3-}$ and $Fe(CN)_6^{4-}$, as observed in Refs. [161, 162]. These two charging mechanisms have opposite thermal signatures: (i) EDL formation/adsorption of $Fe(CN)_6^{3-}$ and $Fe(CN)_6^{4-}$ anions on GP is exothermic and (ii) the oxidation reaction $Fe(CN)_6^{4-} \rightarrow Fe(CN)_6^{3-} + e^-$ in the gel electrolyte was found to be endothermic both experimentally [61,163,164] and analytically, based on entropy considerations [165].

Moreover, in contrast to Devices 1 and 2, the reversible heat generation rate at the negative electrode $\dot{Q}_{rev,-}(t)$ was systematically larger than that at the positive electrode $\dot{Q}_{rev,+}(t)$ for both Devices 3 and 4 at all imposed current I. In addition, the reversible heat generation rates $\dot{Q}_{rev,-}(t)$ were exothermic during charging and endothermic during discharging. Furthermore, the magnitude of $\dot{Q}_{rev,-}(t)$ increased with increasing current I. Note that $\dot{Q}_{rev,-}(t)$ was larger in Device 3 than in Device 4 because the graphene petal mass loading of the negative electrode was about 33% larger in Device 3 than in Device 4 [Figure 5.9(b)]. The instantaneous reversible heat generation rate in the entire cell $\dot{Q}_{rev,T}(t) = \dot{Q}_{rev,+}(t) + \dot{Q}_{rev,-}(t)$ followed the behavior observed at the negative electrode for Devices 3 and 4 [Figure 5.9(c)]. Here also, there was a slight time lag at the transition between charging and discharging steps, due to response time of the heat flux sensors (0.7 s to reach 95% of actual value, gSKIN-XP, greenTEG) and thermal mass of the GP/BP electrodes and gel electrolyte in Devices 3 and 4.

Finally, Figure 5.9(d) plots the time-averaged reversible heat generation over a charging step at each electrode $\bar{\dot{Q}}^c_{rev,i}$ as a function of current I for Devices 3 and 4. At the positive electrode, $\bar{\dot{Q}}^c_{rev,+}$ was nearly zero for all currents, indicating a comparable amount of endothermic and exothermic heat generated during a charging step. On the other hand, at the negative electrode, $\bar{\dot{Q}}^c_{rev,-}$ in both Devices 3 and 4 was positive and increased with imposed current I. This result is consistent with $\bar{\dot{Q}}^c_{rev}$ at the positive electrodes of EDLC devices consisting of activated carbon electrodes in different electrolytes [87] and that at positive and negative electrodes without CMC binder [88], where neither redox reactions nor overscreening effects were present. Notably, the magnitude of instantaneous reversible heat generation rate $\dot{Q}_{rev,i}(t)$ was larger in Devices 3 and 4 than in Devices 1 and 2 at both electrodes and for any given current I. The value of $\dot{Q}_{rev,+}(t)$, $\dot{Q}_{rev,-}(t)$, and $\dot{Q}_{rev,T}(t)$ in Devices 3 and 4 with redox-active gel electrolyte oscillated between $\pm$ 0.2 mW, $\pm$ 0.5 mW, and $\pm$ 0.7 mW, respectively while $\dot{Q}_{rev,+}(t)$, $\dot{Q}_{rev,-}(t)$, and $\dot{Q}_{rev,T}(t)$ in Devices 1 and 2 with conventional gel electrolyte (without redox reaction) oscillated in a smaller range between $\pm$ 0.05 mW, $\pm$ 0.03 mW, and $\pm$ 0.1 mW, respectively. This could be predominantly attributed to the additional redox reactions that enhance charge storage and led to larger capacitance and thus, stronger thermal signatures. The larger reversible heat generation rate could also be due to the larger potential window for Devices 3 and 4 than those for Devices 1 and 2.

Faradaic and capacitive regimes in a galvanostatic cycling

For Device 3 under imposed current $I = 2$ mA, Figure 5.10 shows the cell potential $\psi_s(t)$ features a small slope at the beginning of charging indicating larger differential capacitance C_{diff} at the early stage of the charging process from $\psi_s(t) \sim 0$ to 0.4 V. This potential range corresponded to the Faradaic regime when Faradaic reactions dominated. This interpretation is consistent with observation of the

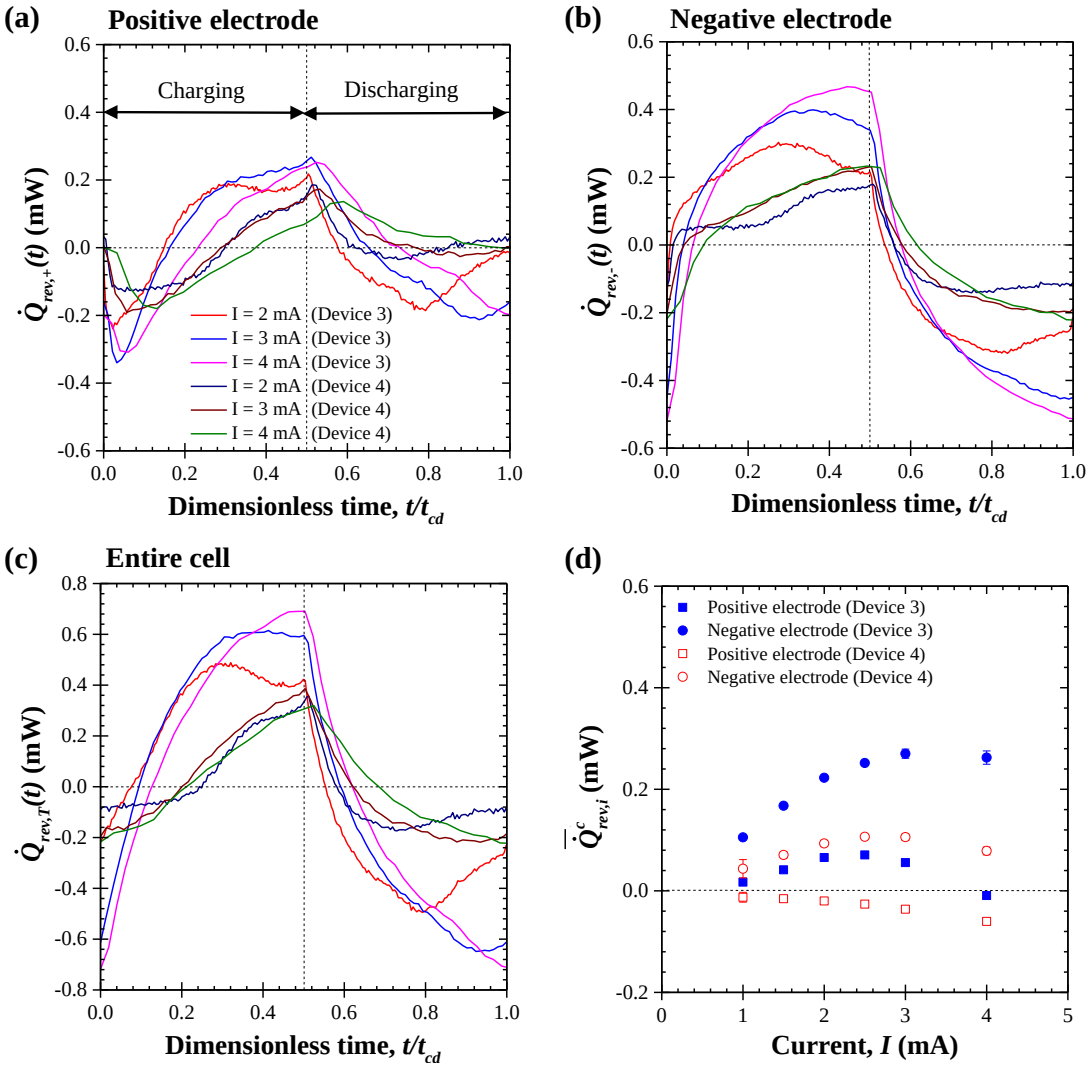

Figure 5.9: One charging-discharging cycle of the reversible heat generation rate (a) $\dot{Q}_{rev,+}(t)$ at the positive electrode, (b) $\dot{Q}_{rev,-}(t)$ at the negative electrode, (c) $\dot{Q}_{rev,T}(t)$ in the entire cell for Devices 3 and 4 as functions of dimensionless time t/t_{cd} for constant current I = 2, 3, and 4 mA. (d) Corresponding time-averaged reversible heat generation rate $\bar{\dot{Q}}^c_{rev,+}$ at the positive and $\bar{\dot{Q}}^c_{rev,-}$ at the negative electrodes during a charging step for Devices 3 and 4.

redox peaks in CV curves (Figure 5.2). The larger differential capacitance C_{diff} can be attributed to Faradaic reactions (Faradaic regime) during charging, while the smaller differential capacitance C_{diff} in the second part of the charging process (capacitive regime) from $\psi_s(t) \sim 0.4$ to 1.2 V, can be attributed to EDL formation [155]

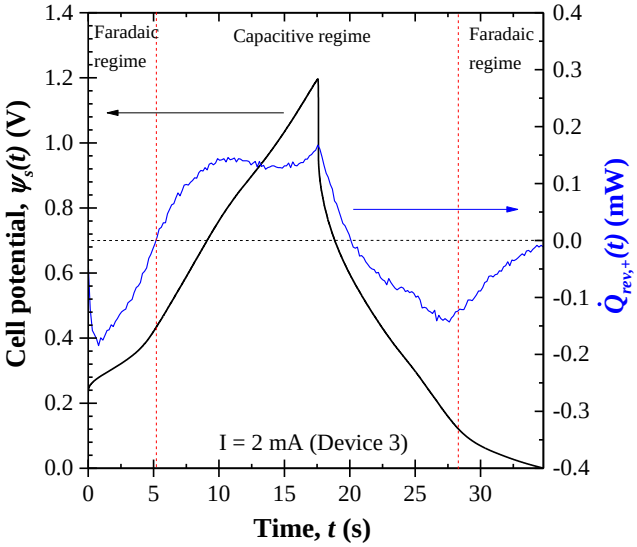

Figure 5.10: Cell potential under galvanostatic cycling for Device 3 under imposed current $I = 2$ mA (left Y-axis) and the corresponding profile of instantaneous reversible heat generation rate $\dot{Q}_{rev,+}(t)$ at the positive electrode (right Y-axis) as functions of time t with two vertical dashed red lines dividing Faradaic and capacitive regimes over the time span.

Comparison between heat generation from the devices and from human body

Overall, heat generation in Devices 1 and 2 charged under constant current of 4 mA [Figures 5.11(a) and 5.11(b)] would result in a heat flux of up to 2.9 W/m^2 on each face of the devices representing 3% of the total metabolic heat dissipation rate given off by the body of 91.7 W/m^2 by convection, radiation and evaporation [166]. On the other hand, the heat generation in Devices 3 and 4 would reach up to 10.7 W/m^2 representing 12% of the total metabolic heat dissipation rate. Note

that the presence of all wearable devices would reduce natural convection and evaporation from the skin. It also remains unclear how the temporal fluctuations in heat generation rate may be perceived by the person wearing such devices. This suggests that active thermal management may be necessary, particularly for devices with redox-active gel electrolytes.

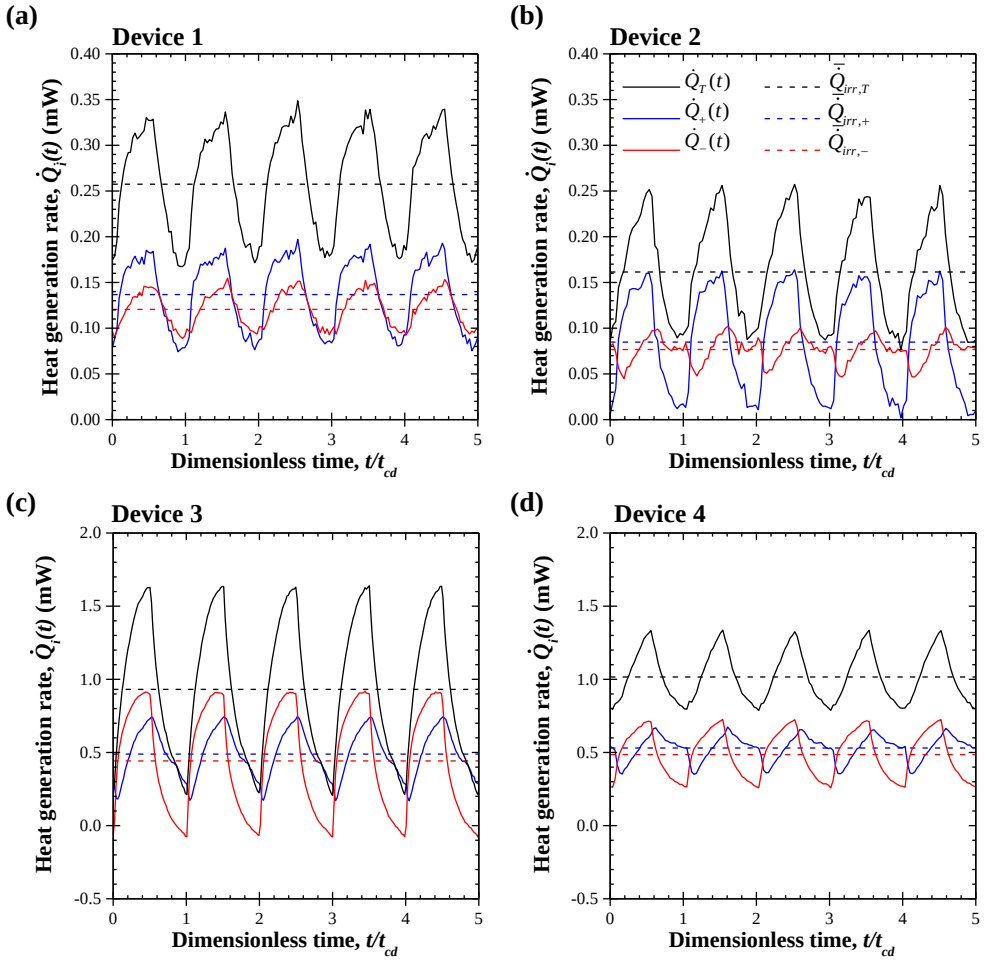

Figure 5.11: Instantaneous heat generation rates $\dot{Q}_+(t)$, $\dot{Q}_-(t)$, and $\dot{Q}_T(t)$ and their time-averaged heat generation rates $\bar{\dot{Q}}_+(t)$, $\bar{\dot{Q}}_-(t)$, and $\bar{\dot{Q}}_T(t)$ at the positive and negative electrodes and for the entire cell for (a) Device 1, (b) Device 2, (c) Device 3, and (d) Device 4 under constant current cycling at $I = 4$ mA for potential windows (ψ_{max} - ψ_{min}) of 1.0 V, 0.8 V, 1.2 V, and 1.2 V, respectively (see Table 2).

5.3 Chapter summary

This chapter assesses the effect of gel electrolyte composition on heat generation rate in all-solid-state supercapacitors using graphene petals grown on buckypaper electrodes. Two all-solid-state supercapacitor devices with conventional gel electrolyte (H_3PO_4 in PVA) and other two devices with redox-active gel electrolyte ($K_3Fe(CN)_6$-$K_4Fe(CN)_6$ in PVA) were fabricated and tested for their capacitance, internal resistance, and heat generation rate. For all devices, the measured irreversible heat generation $\bar{\dot{Q}}_{irr,T}$ was proportional to I^2 and equal to Joule heating $\bar{\dot{Q}}_J$. It was about five times larger in devices with redox-active gel electrolyte than that in devices with conventional gel electrolyte due to larger internal resistance R_S. Moreover, reversible heat generation rates were different at the positive and negative electrodes of all devices. In a conventional gel electrolyte, at the positive electrode $\dot{Q}_{rev,+}(t)$ was exothermic during charging and endothermic during discharging while at the negative electrode, $\dot{Q}_{rev,-}(t)$ was endothermic at the beginning of charging step and exothermic for the rest of the charging step due to the effect of overscreening on charging mechanism. By contrast, at the negative electrode of devices with redox-active gel electrolyte, $\dot{Q}_{rev,-}(t)$ was clearly exothermic during charging and endothermic during discharging whereas $\dot{Q}_{rev,+}(t)$ at the positive electrode combined (i) exothermic EDL formation/adsorption of $Fe(CN)_6^{3-}$ and $Fe(CN)_6^{4-}$ anions on GP and (ii) endothermic redox reaction of $Fe(CN)_6^{4-} \rightarrow Fe(CN)_6^{3-} + e^-$ in the gel electrolyte resulting in both endothermic and exothermic during charging. Overall, heat generation measurements can be used to provide insight into the electrochemical processes occurring during charging/discharging of all-solid-state supercapacitors. They can also be used to design thermal management solutions.

CHAPTER 6

Conclusions and Future Work

6.1 Conclusions

The objectives of the study were to investigate the effect of temperature on the heat generation and the associated electrochemical phenomena in ionic liquid-based EDLCs under (i) a small potential window of 1 V in order to compare with aqueous and organic electrolytes and (ii) a larger potential window of 2.5 V for more realistic applications, and (iii) the effect of redox-active components on the heat generation in all-solid-state graphene-based supercapacitors.

The first objective was achieved by measuring separately the instantaneous heat generation rate at each electrode of ionic liquid-based electric double layer capacitors (EDLCs) at three different temperatures, 20 °C, 40 °C, and 60 °C, under galvanostatic cycling using an *in operando* isothermal calorimeter. Here, the ionic liquid-based electrolyte consists of 1 M N-butyl-n-methylpyrrolidinium bis(trifluoromethane sulfonyl)imide ($Pyr_{14}TFSI$) dissolved in propylene carbonate (PC). The potential window was limited to 1 V to compare with results from similar devices using aqueous or organic electrolytes. First, the results establish that Joule heating of the device was the main source of irreversible heat generation similar to previous results obtained from EDLC devices with aqueous or organic electrolytes for the operating conditions considered. The irreversible heat generation rate was similar at the positive and negative electrodes and decreased with increasing temperature due to enhanced ion mobility in the IL-based electrolyte resulting in the decrease in internal resistance. Furthermore reversible heat generation rates at the positive and negative electrodes were mostly exothermic

during charging and endothermic during discharging due to the change in entropy of the electrolyte system. It increased slightly with increasing temperature and was larger at the positive electrode due to the fact that adsorbing $TFSI^-$ anions were smaller than Pyr_{14}^+ cations. The reversible heat generation rate at the negative electrode featured a small endothermic dip at the beginning of the charging step potentially due to overscreening effect and/or endothermic desolvation of PC molecules from Pyr_{14}^+ cations.

The second objective was achieved in a similar manner as the first objective. Here also, standard electrochemical and heat generation measurements were performed. However, two EDLCs consisted of two identical activated carbon electrodes with either neat $Pyr_{14}TFSI$ or $Pyr_{14}TFSI$ diluted in PC were investigated and compared. In addition, the cell potential window was extended to 2.5 V while the temperature was extended to 5 °C as lower limit and 80 °C as upper limit. First, the instantaneous heat generation rate was similar at each electrode in neat IL while it was smaller at the negative electrode than at the positive electrode in devices with diluted IL in PC. In addition, endothermic dips appeared and grew with increasing temperature above 60 °C at the negative electrode at the beginning of the charging step. They were attributed to (i) overscreening effects in both electrolytes as well as to (ii) desolvation of Pyr_{14}^+ cations and (iii) partial decomposition of PC in diluted IL electrolyte. Moreover, the irreversible heat generation rate in both devices decreased with increasing temperature due to the significant increase in the electrolyte ionic conductivity, particularly for the device with neat $Pyr_{14}TFSI$ electrolyte. The irreversible heat generation rates in the device with 1 M $Pyr_{14}TFSI$ in PC increased sharply at 80 °C as a result of PC decomposition. In addition, the total irreversible heat generation rate in each device exceeded Joule heating. This was attributed to additional irreversible heat generation caused by charge redistribution in the porous electrode and increasing leakage current due to ion desorption with increasing temperature. Second,

in both EDLC devices, the time-averaged reversible heat generation rate over the charging step increased with increasing temperature and was larger at the positive than at the negative electrode due to the better accessibility of smaller $TFSI^-$ anions into subnanoscale pores compared with larger Pyr_{14}^+ cations. Furthermore, the time-averaged reversible heat generation rate during charging at both electrodes increased linearly with imposed current except in the device with IL diluted in PC above 60 °C.

The third objective was achieved by fabricating two all-solid-state supercapacitor devices with conventional gel electrolyte (H_3PO_4 in PVA) and other two devices with redox-active gel electrolyte ($K_3Fe(CN)_6$-$K_4Fe(CN)_6$ in PVA). Then, standard electrochemical and heat generation measurements were performed on those devices. For all devices under potential windows smaller than 1.2 V, the irreversible heat generation $\bar{\dot{Q}}_{irr,T}$ was proportional to I^2 and equal to Joule heating $\bar{\dot{Q}}_J$. Moreover, reversible heat generation rates were different at the positive and negative electrodes of all devices. In a conventional gel electrolyte, at the positive electrode $\dot{Q}_{rev,+}(t)$ was exothermic during charging and endothermic during discharging while at the negative electrode, $\dot{Q}_{rev,-}(t)$ was endothermic at the beginning of charging step and exothermic for the rest of the charging step due to the overscreening effect. By contrast, at the negative electrode of devices with redox-active gel electrolyte, $\dot{Q}_{rev,-}(t)$ was clearly exothermic during charging and endothermic during discharging whereas $\dot{Q}_{rev,+}(t)$ at the positive electrode combined (i) exothermic EDL formation/adsorption of anions on graphene petals and (ii) endothermic redox reaction in the gel electrolyte resulting in both endothermic and exothermic during charging.

6.2 Future work

The effect of ion size and valency on charging mechanism of in MnO_2 cryptomelane with aqueous electrolytes

MnO_2 is one of the most common pseudocapacitive electrode in hybrid pseudocapacitors pairing with an activated carbon electrode. In fact, MnO_2 exists in many and different crystallographic structures. Especially, MnO_2 cyptomelene exhibits fast surface redox reaction at the electrode/electrolyte interface. However, depending on the size of the cations, charging mechanism can be different. Several electrolytes can be tested for its heat generation rate associated with electrochemical phenomena. One idea is to investigate MnO_2 pseudocapacitive electrodes in electrolytes made of sulfate salts of alkaline metals (e.g., Li_2SO_4, Na_2SO_4, K_2SO_4, and Cs_2SO_4) and of an alkaline-earth metal (e.g., $MgSO_4$) dissolved in DI water. By fixing the anions to be SO_4^{2-} and varying cations with different sizes (Li^+, K^+, Na^+, and Cs^+) and valencies (Mg^{2+}), the effect of ion size and valency on charging mechanism can be explored. The result would provide the insight in charging mechanisms and therefore to evaluate promising electrolyte for such MnO_2 hybrid supercapacitors.

APPENDIX A

Supplementary Materials for Background

A.1 Heat flux and heat generation rate relation

A.1.1 Schematic and assumptions

• **Schematic:** Figure A.1 shows the schematic of an electrode and its thermal components.

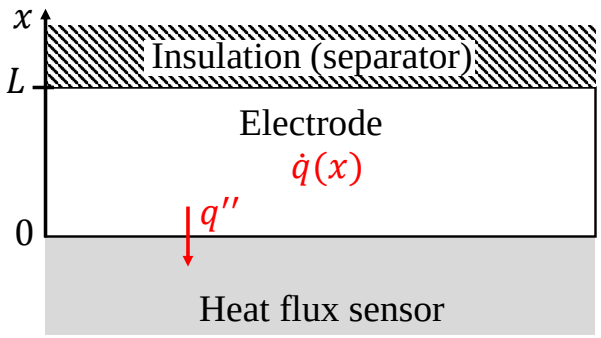

Figure A.1: Schematic of the 1D transient heat transfer model with heat generation at the electrode.

• **Assumptions:**

1. Constant properties, i.e., ρ, c_p, and k.

2. The temperature variation at the surface of the electrode (y-z plane) can be ignored [84, 86].

3. Heat losses from the side faces are ignored.

A.1.2 Governing equations

Heat conduction equation for an electrode can be written as,

$$\rho c_p \frac{\partial T}{\partial t} = \left[\frac{\partial}{\partial x}\left(k\frac{\partial T}{\partial x}\right) + \frac{\partial}{\partial y}\left(k\frac{\partial T}{\partial y}\right) + \frac{\partial}{\partial z}\left(k\frac{\partial T}{\partial z}\right)\right] + \dot{q}(x) \tag{A.1}$$

where ρ, c_p, and k are the effective density, specific heat, and thermal conductivity of the electrode and $\dot{q}$ is the volumetric heat generation rate in the electrode.

A.1.3 Boundary conditions

1. Insulated electrode surface at $x = L$ (the separator works as insulator),

$$\frac{dT}{dx}\Big|_{x=L} = 0. \tag{A.2}$$

2. Heat flux at $x = 0$ is given as,

$$q'' = \frac{dT}{dx}\Big|_{x=0}. \tag{A.3}$$

A.1.4 Heat generation rate

Considering the assumption 1, 2, and 3, Equation (A.1) can be reduced as,

$$\rho c_p \frac{\partial T}{\partial t} = k\frac{\partial^2 T}{\partial x^2} + \dot{q}(x) \tag{A.4}$$

Now, we can write Equation (A.4) at arbitrary time as,

$$k\frac{d^2 T}{dx^2} + \dot{q} = 0. \tag{A.5}$$

By integrating Equation (A.5) and using the first boundary condition, Equation (A.5) can be written as,

$$k\frac{dT}{dx} = \int_{x}^{L} \dot{q}(x)dx \tag{A.6}$$

Now, the heat flux $q^{''}$ at the heat flux sensor/electrode interface can be written as,

$$q^{''} = k\frac{dT}{dx}\Big|_{x=0} = \int_{0}^{L} \dot{q}(x)dx. \tag{A.7}$$

To obtain the heat generation rate $\dot{Q}$ (in mW) in the electrode, Equation (A.7) was multiplied by the footprint area A of the electrode,

$$\dot{Q}(t) = q^{''}A = \frac{\Delta V(t)}{S}A \tag{A.8}$$

APPENDIX B

Supplementary Materials for Chapter 3

B.1 Cyclic voltammograms

Figure B.1 shows CV curves for the same device as that considered in the manuscript but at different temperatures for scan rate ν of (a) 5 mV/s, (b) 10 mV/s, (c) 15 mV/s, and (d) 30 mV/s. It confirms that CV curves were rectangular at all temperatures and scan rates considered, as observed in Figure 3.1(b) for scan rate ν = 20 mV/s.

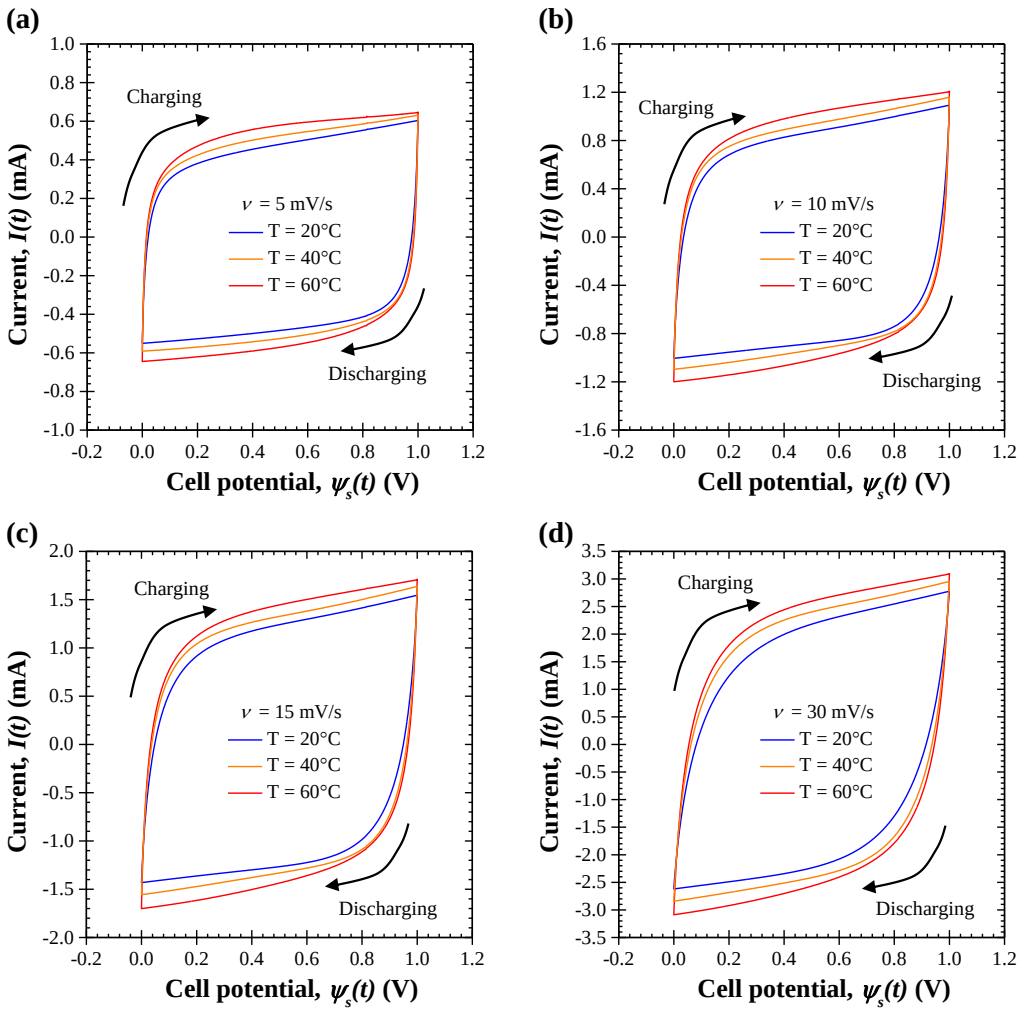

Figure B.1: Cyclic voltammogram from the same device as in the manuscript at temperature between 20 °C and 60 °C at scan rate ν = (a) 5 mV/s, (b) 10 mV/s, (c) 15 mV/s, and (d) 30 mV/s .

B.2 Cell potential under galvanostatic cycling

Figure B.2 shows the galvanostatic charge-discharge curves for the same device as that considered in the manuscript for temperature between 20 °C and 60 °C under imposed (a) 2 mA, (b) 3 mA, (c) 5 mA, and (d) 6 mA. It confirms the observations made from Figure 3.3(b) at imposed current $I = 4$ mA.

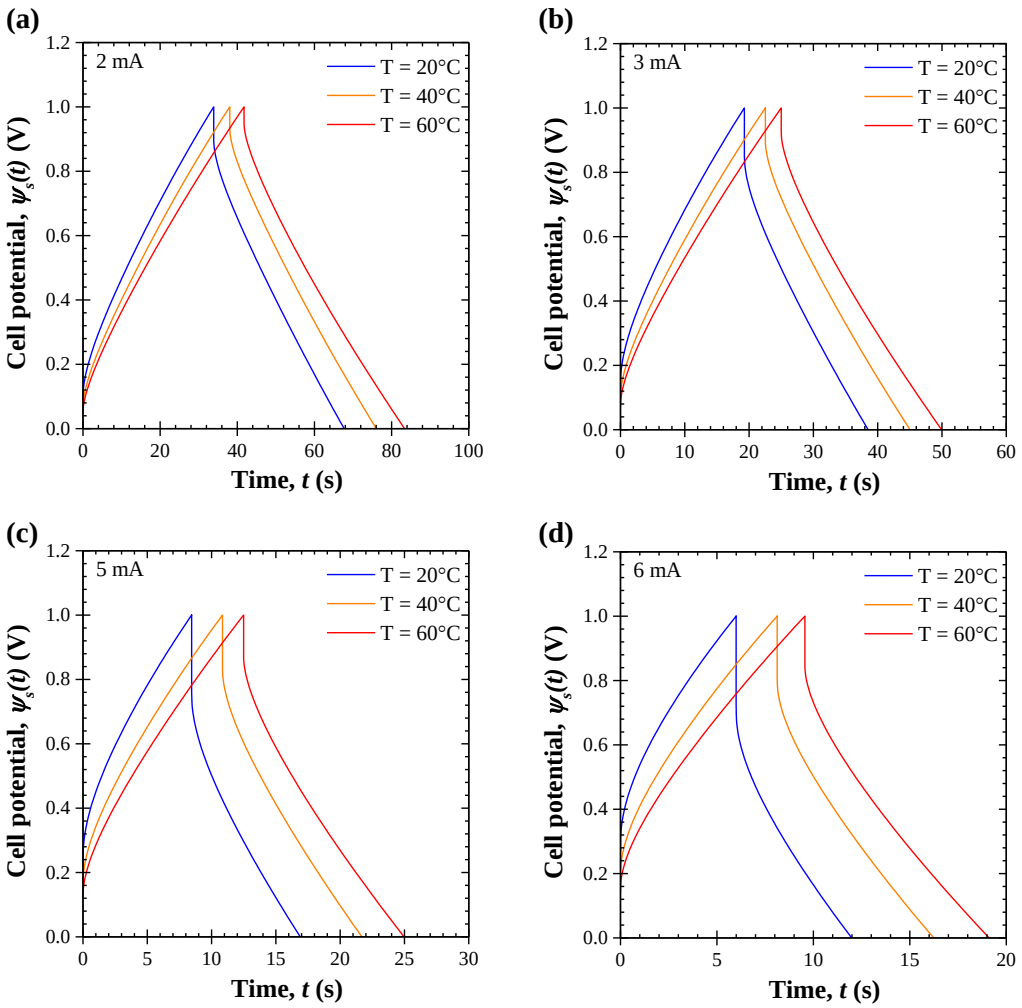

Figure B.2: Cell potential for the same device as in the manuscript under galvanostatic cycling for temperature between 20 °C and 60 °C under imposed current (a) 2 mA, (b) 3 mA, (c) 5 mA, and (d) 6 mA.

B.3 Reversible heat generation rates

Figures B.3 and B.4 plot the instantaneous reversible heat generation rates (a,d) $\dot{Q}_{rev,+}(t)$ at the positive electrode, (b,e) $\dot{Q}_{rev,-}(t)$ at the negative electrode, and (c,f) $\dot{Q}_{rev,T}(t)$ in the entire cell as functions of the dimensionless time t/t_{cd} for current $I = 2$ and 3 mA (Figures B.3) and for current $I = 5$ and 6 mA (Figures B.4), respectively, at constant temperature of 20 °C, 40 °C, and 60 °C. It confirms the observation made from Figures 3.7(a)−3.7(c) for imposed current $I = 4$ mA.

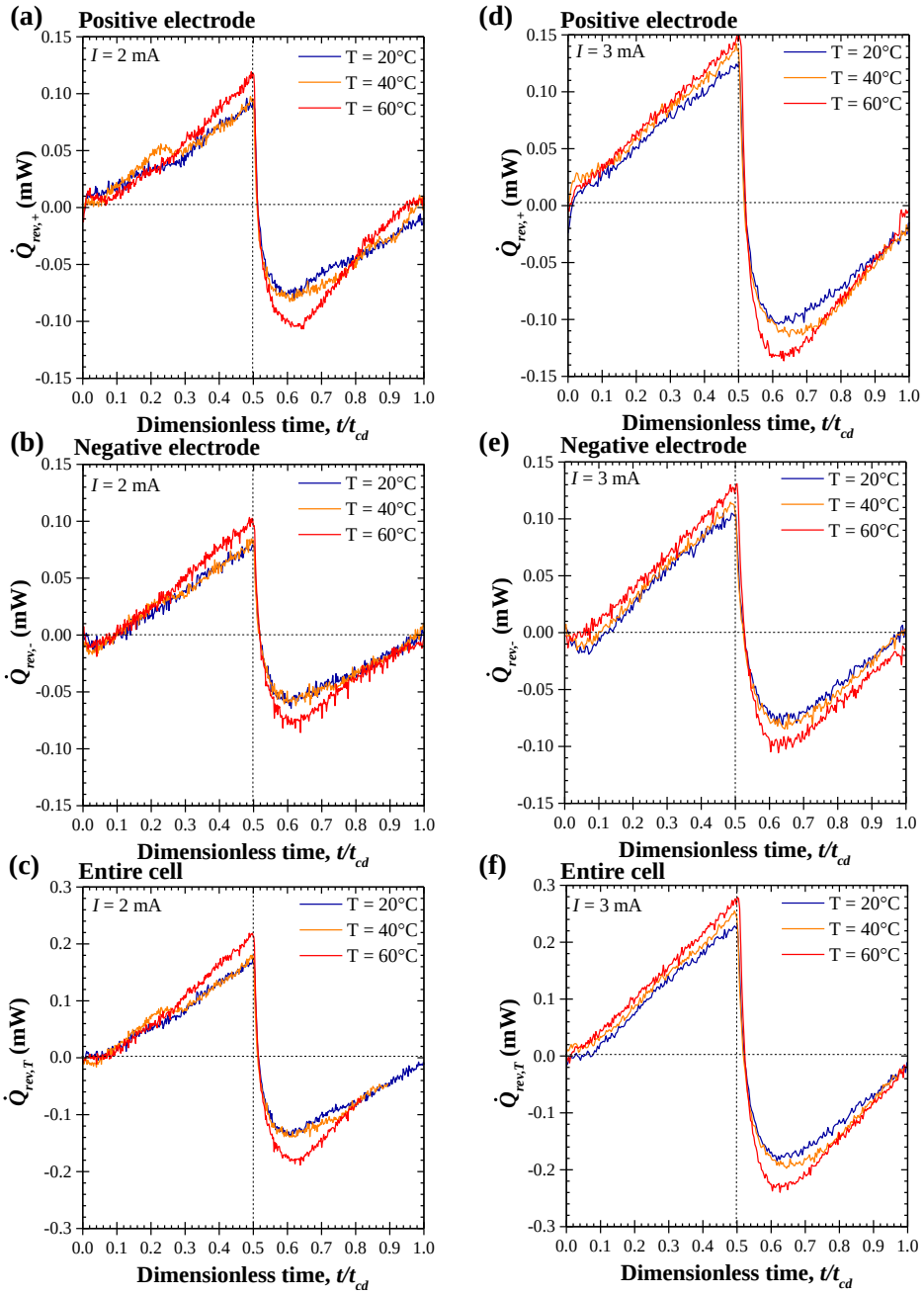

Figure B.3: Reversible heat generation rates (a) $\dot{Q}_{rev,+}(t)$ at the positive electrode, (b) $\dot{Q}_{rev,-}(t)$ at the negative electrode, and (c) $\dot{Q}_{rev,T}(t)$ in the entire cell as functions of the dimensionless time t/t_{cd} under current $I = 2$ mA and (d) $\dot{Q}_{rev,+}(t)$, (e) $\dot{Q}_{rev,-}(t)$, and (f) $\dot{Q}_{rev,T}(t)$ under current $I = 3$ mA for temperature between 20 °C and 60 °C.

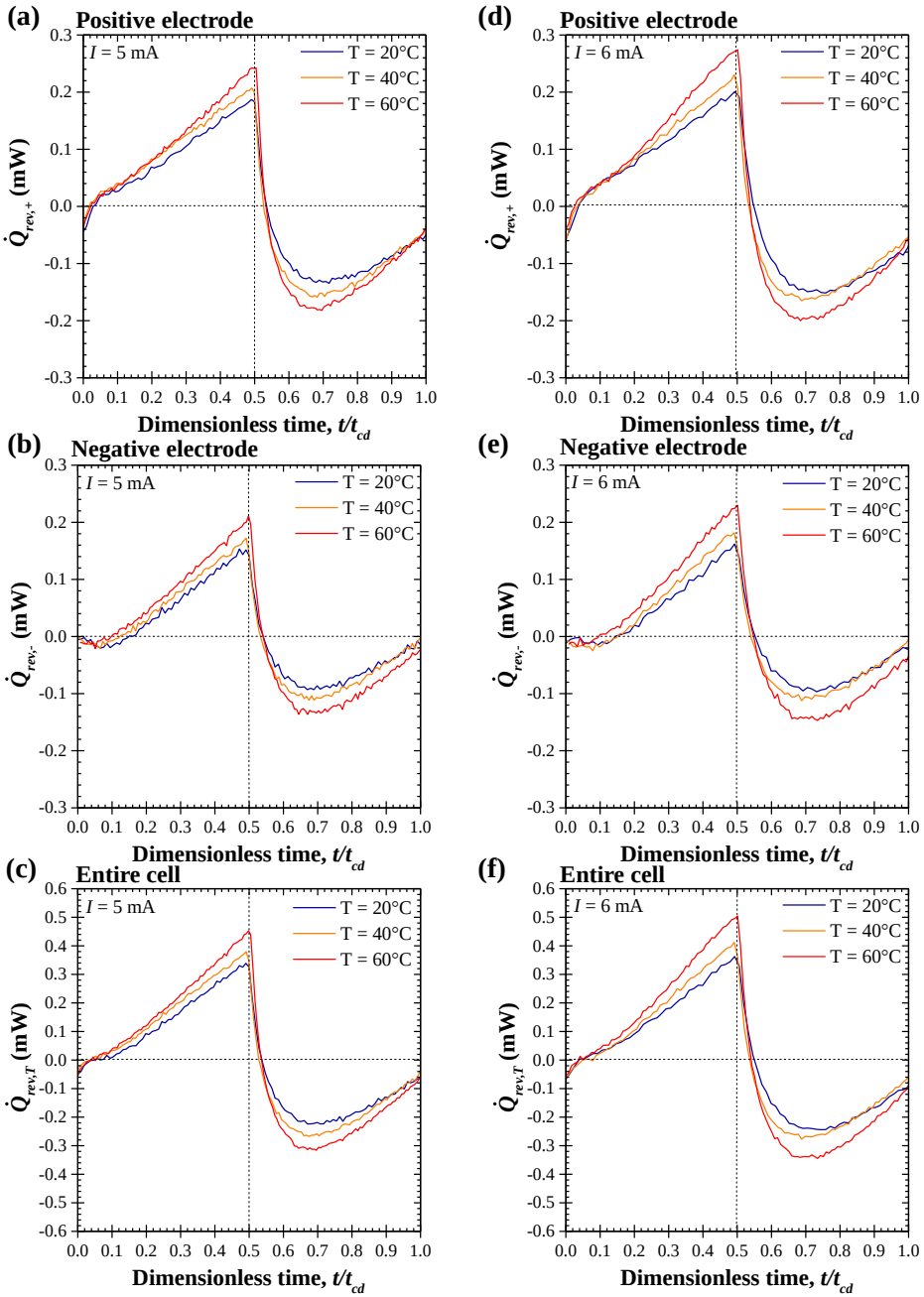

Figure B.4: Reversible heat generation rates (a) $\dot{Q}_{rev,+}(t)$ at the positive electrode, (b) $\dot{Q}_{rev,-}(t)$ at the negative electrode, and (c) $\dot{Q}_{rev,T}(t)$ in the entire cell as functions of the dimensionless time t/t_{cd} under current $I = 5$ mA and (d) $\dot{Q}_{rev,+}(t)$, (e) $\dot{Q}_{rev,-}(t)$, and (f) $\dot{Q}_{rev,T}(t)$ under current $I = 6$ mA for temperature between 20 °C and 60 °C.

References

[1] B. E. Conway, *Electrochemical Supercapacitors: Scientific Fundamentals and Technological Applications*, Kluwer Academic/Plenum Publishers, New York, NY, 1999.

[2] J. B. Goodenough, H. D. Abruna, and M. V. Buchanan, "Basic Research Needs for Electrical Energy Storage: Report of the Basic Energy Sciences Workshop for Electrical Energy Storage", Tech. Rep. DOI 10.2172/935429, U.S. Department of Energy, 2007.

[3] A. Burke, "Ultracapacitors: why, how, and where is the technology", *Journal of Power Sources*, vol. 91, no. 1, pp. 37–50, 2000.

[4] M. D. Stoller, S. Park, Y. Zhu, J. An, and R. S. Ruoff, "Graphene-based ultracapacitors", *Nano Letters*, vol. 8, no. 10, pp. 3498–3502, 2008.

[5] J. R. Miller, "Electrochemical capacitor thermal management issues at high-rate cycling", *Electrochimica Acta*, vol. 52, no. 4, pp. 1703–1708, 2006.

[6] P. Guillemet, Y. Scudeller, and T. Brousse, "Multi-level reduced-order thermal modeling of electrochemical capacitors", *Journal of Power Sources*, vol. 157, no. 1, pp. 630–640, 2006.

[7] L. Maharjan, S. Inoue, and H. Akagi, "A transformerless energy storage system based on a cascade multilevel PWM converter with star configuration", *IEEE Transactions on Industry Applications*, vol. 44, no. 5, pp. 1621–1630, 2008.

[8] P. Simon and Y. Gogotsi, "Materials for electrochemical capacitors", *Nature Materials*, vol. 7, no. 11, pp. 845–854, 2008.

[9] F. Béguin, V. Presser, A. Balducci, and E. Frackowiak, "Carbons and electrolytes for advanced supercapacitors", *Advanced Materials*, vol. 26, no. 14, pp. 2219–2251, 2014.

[10] C. Zhong, Y. Deng, W. Hu, J. Qiao, L. Zhang, and J. Zhang, "A review of electrolyte materials and compositions for electrochemical supercapacitors", *Chemical Society Reviews*, vol. 44, no. 21, pp. 7484–7539, 2015.

[11] B. Pal, S. Yang, S. Ramesh, V. Thangadurai, and R. Jose, "Electrolyte selection for supercapacitive devices: a critical review", *Nanoscale Advances*, vol. 1, no. 10, pp. 3807–3835, 2019.

[12] V. Augustyn, P. Simon, and B. Dunn, "Pseudocapacitive oxide materials for high-rate electrochemical energy storage", *Energy & Environmental Science*, vol. 7, no. 5, pp. 1597–1614, 2014.

[13] T. Brousse, D. Bélanger, K. Chiba, M. Egashira, F. Favier, J. Long, J. R. Miller, M. Morita, K. Naoi, P. Simon, and W. Sugimoto, "Materials for electrochemical capacitors", in *Springer Handbook of Electrochemical Energy*, pp. 495–561. Springer, 2017.

[14] J. A. Rogers, "Electronics for the human body", *Jama*, vol. 313, no. 6, pp. 561–562, 2015.

[15] H. Nishide and K. Oyaizu, "Toward flexible batteries", *Science*, vol. 319, no. 5864, pp. 737–738, 2008.

[16] L. Nyholm, G. Nyström, A. Mihranyan, and M. Strømme, "Toward flexible polymer and paper-based energy storage devices", *Advanced Materials*, vol. 23, no. 33, pp. 3751–3769, 2011.

[17] H. Guo, M.-H. Yeh, Y. Zi, Z. Wen, J. Chen, G. Liu, C. Hu, and Z. L. Wang, "Ultralight cut-paper-based self-charging power unit for self-powered portable electronic and medical systems", *ACS Nano*, vol. 11, no. 5, pp. 4475–4482, 2017.

[18] F. Meng and Y. Ding, "Sub-micrometer-thick all-solid-state supercapacitors with high power and energy densities", *Advanced Materials*, vol. 23, no. 35, pp. 4098–4102, 2011.

[19] W. Liu, H. Lu, C.and Li, R. Y. Tay, L. Sun, X. Wang, W. L. Chow, X. Wang, B. K. Tay, Z. Chen, et al., "based all-solid-state flexible micro-supercapacitors with ultra-high rate and rapid frequency response capabilities", *Journal of Materials Chemistry A*, vol. 4, no. 10, pp. 3754–3764, 2016.

[20] A. Ramadoss, K.-Y. Yoon, S.-I. Kwak, M.-J.and Kim, S.-T. Ryu, and J.-H. Jang, "Fully flexible, lightweight, high performance all-solid-state supercapacitor based on 3-dimensional-graphene/graphite-paper", *Journal of Power Sources*, vol. 337, pp. 159–165, 2017.

[21] L. Yuan, X.-H. Lu, X. Xiao, T. Zhai, J. Dai, F. Zhang, B. Hu, X. Wang, L. Gong, J. Chen, et al., "Flexible solid-state supercapacitors based on carbon nanoparticles/ MnO_2 nanorods hybrid structure", *ACS Nano*, vol. 6, no. 1, pp. 656–661, 2011.

[22] Y. J. Kang, H. Chung, C.-H. Han, and W. Kim, "All-solid-state flexible supercapacitors based on papers coated with carbon nanotubes and ionic-liquid-based gel electrolytes", *Nanotechnology*, vol. 23, no. 6, pp. 065401, 2012.

[23] Y. Xie, Y. Liu, Y. Zhao, Y. H. Tsang, S. P. Lau, H. Huang, and Y. Chai, "Stretchable all-solid-state supercapacitor with wavy shaped polyaniline/graphene electrode", *Journal of Materials Chemistry A*, vol. 2, no. 24, pp. 9142–9149, 2014.

[24] L. Pilon, H. Wang, and A. d'Entremont, "Recent advances in continuum modeling of interfacial and transport phenomena in electric double layer capacitors", *Journal of the Electrochemical Society*, vol. 162, no. 5, pp. A5158–A5178, 2015.

[25] L. L. Zhang, Y. Gu, and X. Zhao, "Advanced porous carbon electrodes for electrochemical capacitors", *Journal of Materials Chemistry A*, vol. 1, no. 33, pp. 9395–9408, 2013.

[26] F. Stoeckli and T. A. Centeno, "Optimization of the characterization of porous carbons for supercapacitors", *Journal of Materials Chemistry A*, vol. 1, no. 23, pp. 6865–6873, 2013.

[27] X. Du, P. Guo, H. Song, and X. Chen, "Graphene nanosheets as electrode material for electric double-layer capacitors", *Electrochimica Acta*, vol. 55, no. 16, pp. 4812–4819, 2010.

[28] W. Yang, M. Ni, X. Ren, Y. Tian, N. Li, Y. Su, and X. Zhang, "Graphene in supercapacitor applications", *Current Opinion in Colloid & Interface Science*, vol. 20, no. 5-6, pp. 416–428, 2015.

[29] Z.-S. Wu, D.-W. Wang, W. Ren, J. Zhao, G. Zhou, F. Li, and H.-M. Cheng, "Anchoring hydrous RuO_2 on graphene sheets for high-performance electrochemical capacitors", *Advanced Functional Materials*, vol. 20, no. 20, pp. 3595–3602, 2010.

[30] J. Y. Hwang, M. F. El-Kady, Y. Wang, L. Wang, Y. Shao, K. Marsh, J. M. Ko, and R. B. Kaner, "Direct preparation and processing of graphene/RuO_2 nanocomposite electrodes for high-performance capacitive energy storage", *Nano Energy*, vol. 18, pp. 57–70, 2015.

[31] S. Chen, J. Zhu, X. Wu, Q. Han, and X. Wang, "Graphene oxide- MnO_2 nanocomposites for supercapacitors", *ACS Nano*, vol. 4, no. 5, pp. 2822–2830, 2010.

[32] N. Li, J.and Wang, Y. Zhao, Y. Ding, and L. Guan, "MnO_2 nanoflakes coated on multi-walled carbon nanotubes for rechargeable lithium-air batteries", *Electrochemistry Communications*, vol. 13, no. 7, pp. 698–700, 2011.

[33] K. R. Prasad and N. Munichandraiah, "Fabrication and evaluation of 450 F electrochemical redox supercapacitors using inexpensive and high-performance, polyaniline coated, stainless-steel electrodes", *Journal of Power Sources*, vol. 112, no. 2, pp. 443–451, 2002.

[34] D.-W. Wang, F. Li, J. Zhao, W. Ren, Z.-G. Chen, J. Tan, Z.-S. Wu, I. Gentle, G. Q. Lu, and H.-M. Cheng, "Fabrication of graphene/polyaniline composite paper via in situ anodic electropolymerization for high-performance flexible electrode", *ACS Nano*, vol. 3, no. 7, pp. 1745–1752, 2009.

[35] K. Jurewicz, S. Delpeux, V. Bertagna, F. Beguin, and E. Frackowiak, "Supercapacitors from nanotubes/polypyrrole composites", *Chemical Physics Letters*, vol. 347, no. 1-3, pp. 36–40, 2001.

[36] P. A. Mini, A. Balakrishnan, S. V. Nair, and K. R. V. Subramanian, "Highly super capacitive electrodes made of graphene/poly(pyrrole)", *Chemical Communications*, vol. 47, no. 20, pp. 5753–5755, 2011.

[37] S. Zhang, S. Brahim, and S. Maat, "High-voltage operation of binder-free CNT supercapacitors using ionic liquid electrolytes", *Journal of Materials Research*, vol. 33, no. 9, pp. 1179–1188, 2018.

[38] A. Lewandowski, A. Olejniczak, M. Galinski, and I. Stepniak, "Performance of carbon–carbon supercapacitors based on organic, aqueous and ionic liquid electrolytes", *Journal of Power Sources*, vol. 195, no. 17, pp. 5814–5819, 2010.

[39] A. Balducci, "Electrolytes for high voltage electrochemical double layer capacitors: A perspective article", *Journal of Power Sources*, vol. 326, pp. 534–540, 2016.

[40] P. Johansson, L. E. Fast, A. Matic, G. B. Appetecchi, and S. Passerini, "The conductivity of pyrrolidinium and sulfonylimide-based ionic liquids: A combined experimental and computational study", *Journal of Power Sources*, vol. 195, no. 7, pp. 2074–2076, 2010.

[41] M. Nádherná, J. Reiter, J. Moškon, and R. Dominko, "Lithium bis(fluorosulfonyl)imide–PYR_{14}TFSI ionic liquid electrolyte compatible with graphite", *Journal of Power Sources*, vol. 196, no. 18, pp. 7700–7706, 2011.

[42] M. Galiński, A. Lewandowski, and I. Stepniak, "Ionic liquids as electrolytes", *Electrochimica Acta*, vol. 51, no. 26, pp. 5567–5580, 2006.

[43] A. Balducci, F. Soavi, and M. Mastragostino, "The use of ionic liquids as solvent-free green electrolytes for hybrid supercapacitors", *Applied Physics A*, vol. 82, no. 4, pp. 627–632, 2006.

[44] C. Arbizzani, G. Gabrielli, and M. Mastragostino, "Thermal stability and flammability of electrolytes for lithium-ion batteries", *Journal of Power Sources*, vol. 196, no. 10, pp. 4801–4805, 2011.

[45] J. Reiter, S. Jeremias, E. Paillard, M. Winter, and S. Passerini, "Fluorosulfonyl-(trifluoromethanesulfonyl)imide ionic liquids with enhanced asymmetry", *Physical Chemistry Chemical Physics*, vol. 15, no. 7, pp. 2565–2571, 2013.

[46] S. Jeremias, M. Kunze, S. Passerini, and M. Schoonhoff, "Polymerizable ionic liquid with state of the art transport properties", *The Journal of Physical Chemistry B*, vol. 117, no. 36, pp. 10596–10602, 2013.

[47] K. Hayamizu, Y. Aihara, H. Nakagawa, T. Nukuda, and W. S. Price, "Ionic conduction and ion diffusion in binary room-temperature ionic liquids composed of [emim][BF_4] and $LiBF_4$", *The Journal of Physical Chemistry B*, vol. 108, no. 50, pp. 19527–19532, 2004.

[48] V. Ruiz, T. Huynh, S. R. Sivakkumar, and A. G. Pandolfo, "Ionic liquid–solvent mixtures as supercapacitor electrolytes for extreme temperature operation", *RSC Advances*, vol. 2, no. 13, pp. 5591–5598, 2012.

[49] S. Leyva-García, D. Lozano-Castelló, E. Morallón, T. Vogl, C. Schütter, S. Passerini, A. Balducci, and D. Cazorla-Amorós, "Electrochemical performance of a superporous activated carbon in ionic liquid-based electrolytes", *Journal of Power Sources*, vol. 336, pp. 419–426, 2016.

[50] A. Borenstein, R. Attias, O. Hanna, S. Luski, R. B. Kaner, and D. Aurbach, "A surprising failure mechanism in symmetric supercapacitors at high voltages", *ChemElectroChem*, vol. 4, no. 10, pp. 2660–2668, 2017.

[51] A. Hammar, P. Venet, R. Lallemand, G. Coquery, and G. Rojat, "Study of accelerated aging of supercapacitors for transport applications", *IEEE Transactions on Industrial Electronics*, vol. 57, no. 12, pp. 3972–3979, 2010.

[52] B. Akinwolemiwa, C. Peng, and G. Z. Chen, "Redox electrolytes in supercapacitors", *Journal of the Electrochemical Society*, vol. 162, no. 5, pp. A5054–A5059, 2015.

[53] H. Yu, J. Wu, L. Fan, K. Xu, X. Zhong, Y. Lin, and J. Lin, "Improvement of the performance for quasi-solid-state supercapacitor by using PVA–KOH–KI polymer gel electrolyte", *Electrochimica Acta*, vol. 56, no. 20, pp. 6881–6886, 2011.

[54] A. Singh and A. Chandra, "Enhancing specific energy and power in asymmetric supercapacitors - a synergetic strategy based on the use of redox additive electrolytes", *Scientific Reports*, vol. 6, no. 25793, 2016.

[55] G. Ma, J. Li, K. Sun, H. Peng, J. Mu, and Z. Lei, "High performance solid-state supercapacitor with PVA–KOH–$K_3[Fe(CN)_6]$ gel polymer as electrolyte and separator", *Journal of Power Sources*, vol. 256, pp. 281–287, 2014.

[56] K. Chen, F. Liu, D. Xue, and S. Komarneni, "Carbon with ultrahigh capacitance when graphene paper meets $K_3Fe(CN)_6$", *Nanoscale*, vol. 7, no. 2, pp. 432–439, 2015.

[57] E. Sun, K.and Feng, H. Peng, G. Ma, Y. Wu, H. Wang, and Z. Lei, "A simple and high-performance supercapacitor based on nitrogen-doped porous carbon in redox-mediated sodium molybdate electrolyte", *Electrochimica Acta*, vol. 158, pp. 361–367, 2015.

[58] S. T. Senthilkumar, R. K. Selvan, J. S. Melo, and C. Sanjeeviraja, "High performance solid-state electric double layer capacitor from redox mediated gel polymer electrolyte and renewable tamarind fruit shell derived porous carbon", *ACS Applied Materials & Interfaces*, vol. 5, no. 21, pp. 10541–10550, 2013.

[59] J. Zhong, L.-Q. Fan, X. Wu, J.-H. Wu, G.-J. Liu, J.-M. Lin, M.-L. Huang, and Y.-L. Wei, "Improved energy density of quasi-solid-state supercapacitors using sandwich-type redox-active gel polymer electrolytes", *Electrochimica Acta*, vol. 166, pp. 150–156, 2015.

[60] G. Wang, R. Liang, L. Liu, and B. Zhong, "Improving the specific capacitance of carbon nanotubes-based supercapacitors by combining introducing functional groups on carbon nanotubes with using redox-active electrolyte", *Electrochimica Acta*, vol. 115, pp. 183–188, 2014.

[61] T. Ozeki, I. Watanbe, and S. Ikeda, "Study of the prussian blue/prussian white redox reaction by cyclic voltammothermometry", *Journal of Electroanalytical Chemistry and Interfacial Electrochemistry*, vol. 236, no. 1-2, pp. 209–218, 1987.

[62] S. I. Fletcher, F. B. Sillars, R. C. Carter, A. J. Cruden, M. Mirzaeian, N. E. Hudson, J. A. Parkinson, and P. J. Hall, "The effects of temperature on the performance of electrochemical double layer capacitors", *Journal of Power Sources*, vol. 195, no. 21, pp. 7484–7488, 2010.

[63] R. Kötz, M. Hahn, and R. Gallay, "Temperature behavior and impedance fundamentals of supercapacitors", *Journal of Power Sources*, vol. 154, no. 2, pp. 550–555, 2006.

[64] O. Bohlen, J. Kowal, and D. U. Sauer, "Ageing behaviour of electrochemical double layer capacitors: Part I. experimental study and ageing model", *Journal of Power Sources*, vol. 172, no. 1, pp. 468–475, 2007.

[65] C. Masarapu, H. F. Zeng, K. H. Hung, and B. Wei, "Effect of temperature on the capacitance of carbon nanotube supercapacitors", *ACS Nano*, vol. 3, no. 8, pp. 2199–2206, 2009.

[66] H. Michel, "Temperature and dynamics problems of ultracapacitors in stationary and mobile applications", *Journal of Power Sources*, vol. 154, no. 2, pp. 556–560, 2006.

[67] M. Arulepp, L. Permann, J. Leis, A. Perkson, K. Rumma, A. Jänes, and E. Lust, "Influence of the solvent properties on the characteristics of a double layer capacitor", *Journal of Power Sources*, vol. 133, no. 2, pp. 320–328, 2004.

[68] P. Kreczanik, P. Venet, A. Hijazi, and G. Clerc, "Study of supercapacitor aging and lifetime estimation according to voltage, temperature, and RMS current", *IEEE Transactions on Industrial Electronics*, vol. 61, no. 9, pp. 4895–4902, 2014.

[69] P. Liu, M. Verbrugge, and S. Soukiazian, "Influence of temperature and electrolyte on the performance of activated-carbon supercapacitors", *Journal of Power Sources*, vol. 156, no. 2, pp. 712–718, 2006.

[70] W. Liu, X. Yan, J. Lang, and Q. Xue, "Effects of concentration and temperature of $EMIMBF_4$/acetonitrile electrolyte on the supercapacitive behavior of graphene nanosheets", *Journal of Materials Chemistry*, vol. 22, no. 18, pp. 8853–8861, 2012.

[71] W. Li, K. Xu, L. An, F. Jiang, X. Zhou, J. Yang, Z. Chen, R. Zou, and J. Hu, "Effect of temperature on the performance of ultrafine MnO_2 nanobelt supercapacitors", *Journal of Materials Chemistry A*, vol. 2, no. 5, pp. 1443–1447, 2014.

[72] J.-G. Wang, Y. Yang, Z.-H. Huang, and F. Kang, "Effect of temperature on the pseudo-capacitive behavior of freestanding MnO_2@ carbon nanofibers composites electrodes in mild electrolyte", *Journal of Power Sources*, vol. 224, pp. 86–92, 2013.

[73] C. Yuan, X. Zhang, Q. Wu, and B. Gao, "Effect of temperature on the hybrid supercapacitor based on NiO and activated carbon with alkaline polymer gel electrolyte", *Solid State Ionics*, vol. 177, no. 13, pp. 1237–1242, 2006.

[74] S. Park, S.-W. Kang, and K. Kim, "Competition between ionic adsorption and desorption on electrochemical double layer capacitor electrodes in acetonitrile solutions at different currents and temperatures", *Journal of Power Sources*, vol. 372, pp. 8–15, 2017.

[75] B. Xu, F. Wu, R. Chen, G. Cao, S. Chen, and Y. Yang, "Mesoporous activated carbon fiber as electrode material for high-performance electrochemical double layer capacitors with ionic liquid electrolyte", *Journal of Power Sources*, vol. 195, no. 7, pp. 2118–2124, 2010.

[76] A. Likitchatchawankun, G. Whang, J. Lau, O. Munteshari, B. Dunn, and L. Pilon, "Effect of temperature on irreversible and reversible heat generation rates in ionic liquid-based electric double layer capacitors", *Electrochimica Acta*, vol. 338, pp. 135802, 2020.

[77] J. Schiffer, D. Linzen, and D. U. Sauer, "Heat generation in double layer capacitors", *Journal of Power Sources*, vol. 160, no. 1, pp. 765–772, 2006.

[78] H. Gualous, H. Louahlia-Gualous, R. Gallay, and A. Miraoui, "Supercapacitor thermal modeling and characterization in transient state for industrial applications", *IEEE Transactions on Industry Applications*, vol. 45, no. 3, pp. 1035–1044, 2009.

[79] M. Al Sakka, H. Gualous, J. Van Mierlo, and H. Culcu, "Thermal modeling and heat management of supercapacitor modules for vehicle applications", *Journal of Power Sources*, vol. 194, no. 2, pp. 581–587, 2009.

[80] M. Ayadi, A. Eddahech, O. Briat, and J.-M. Vinassa, "Voltage and temperature impacts on leakage current in calendar ageing of supercapacitors", in *Proceedings of the 4th International Conference on Power Engineering, Energy and Electrical Drives*, May 13−17, 2013; Istanbul, Turkey, IEEE, pp. 1466–1470, 2013.

[81] T. Umemura, Y. Mizutani, T. Okamoto, T. Taguchi, K. Nakajima, and K. Tanaka, "Life expectancy and degradation behavior of electric double layer capacitor part I", in *Proceedings of the 7th International Conference on Properties and Applications of Dielectric Materials*, Jun 1−5, 2003; Nagoya, Japan, IEEE, vol. 3, pp. 944–948, 2003.

[82] M. Hahn, R. Kötz, R. Gallay, and A. Siggel, "Pressure evolution in propylene carbonate based electrochemical double layer capacitors", *Electrochimica Acta*, vol. 52, no. 4, pp. 1709–1712, 2006.

[83] A. M. Bittner, M. Zhu, Y. Yang, H. F. Waibel, M. Konuma, U. Starke, and C. J. Weber, "Ageing of electrochemical double layer capacitors", *Journal of Power Sources*, vol. 203, pp. 262–273, 2012.

[84] A. L. d'Entremont and L. Pilon, "First-principles thermal modeling of electric double layer capacitors under constant-current cycling", *Journal of Power Sources*, vol. 246, pp. 887–898, 2014.

[85] A. L. d'Entremont and L. Pilon, "Thermal effects of asymmetric electrolytes in electric double layer capacitors", *Journal of Power Sources*, vol. 273, pp. 196–209, 2015.

[86] Y. Dandeville, P. Guillemet, Y. Scudeller, O. Crosnier, L. Athouel, and T. Brousse, "Measuring time-dependent heat profiles of aqueous electrochemical capacitors under cycling", *Thermochimica Acta*, vol. 526, no. 1-2, pp. 1–8, 2011.

[87] O. Munteshari, J. Lau, A. Krishnan, B. Dunn, and L. Pilon, "Isothermal calorimeter for measurements of time-dependent heat generation rate in individual supercapacitor electrodes", *Journal of Power Sources*, vol. 374, pp. 257–268, 2018.

[88] O. Munteshari, J. Lau, D. S. Ashby, B. Dunn, and L. Pilon, "Effects of constituent materials on heat generation in individual EDLC electrodes", *Journal of The Electrochemical Society*, vol. 165, no. 7, pp. A1547–A1557, 2018.

[89] B.-A. Mei, O. Munteshari, J. Lau, B. Dunn, and L. Pilon, "Physical interpretations of Nyquist plots for EDLC electrodes and devices", *The Journal of Physical Chemistry C*, vol. 122, no. 1, pp. 194–206, 2017.

[90] O. Munteshari, A. Borenstein, R. H. DeBlock, J. Lau, G. Whang, Y. Zhou, A. Likitchatchawankun, R. Kaner, B. Dunn, and L. Pilon, "In operando calorimetric measurements for activated carbon electrodes in neat or diluted ionic liquid electrolytes under large potential windows", *ChemSusChem*, vol. 13, pp. 1–15, 2020.

[91] O. Munteshari, J. Lau, A. Likitchatchawankun, B.-A. Mei, C. S. Choi, D. Butts, B. S. Dunn, and L. Pilon, "Thermal signature of ion intercalation and surface redox reactions mechanisms in model pseudocapacitive electrodes", *Electrochimica Acta*, vol. 307, pp. 512–524, 2019.

[92] A. L. d'Entremont and L. Pilon, "First-principles thermal modeling of hybrid pseudocapacitors under galvanostatic cycling", *Journal of Power Sources*, vol. 335, pp. 172–188, 2016.

[93] A. L. d'Entremont and L. Pilon, "First-order thermal model of commercial EDLCs", *Applied Thermal Engineering*, vol. 67, no. 1-2, pp. 439–446, 2014.

[94] M. V. Fedorov and A. A. Kornyshev, "Ionic liquids at electrified interfaces", *Chemical Reviews*, vol. 114, no. 5, pp. 2978–3036, 2014.

[95] M. Z. Bazant, B. D. Storey, and A. A. Kornyshev, "Double layer in ionic liquids: Overscreening versus crowding", *Physical Review Letters*, vol. 106, no. 4, pp. 046102, 2011.

[96] M. D. Levi, N. Levy, S. Sigalov, G. Salitra, D. Aurbach, and J. Maier, "Electrochemical quartz crystal microbalance (EQCM) studies of ions and solvents insertion into highly porous activated carbons", *Journal of the American Chemical Society*, vol. 132, no. 38, pp. 13220–13222, 2010.

[97] A. Likitchatchawankun, A. Kundu, O. Munteshari, T. S. Fisher, and L. Pilon, "Heat generation in all-solid-state supercapacitors with graphene electrodes and gel electrolytes", *Electrochimica Acta*, vol. 303, pp. 341–353, 2019.

[98] A. Krause and A. Balducci, "High voltage electrochemical double layer capacitor containing mixtures of ionic liquids and organic carbonate as electrolytes", *Electrochemistry Communications*, vol. 13, no. 8, pp. 814–817, 2011.

[99] S. Pohlmann, B. Lobato, T. A. Centeno, and A. Balducci, "The influence of pore size and surface area of activated carbons on the performance of ionic liquid based supercapacitors", *Physical Chemistry Chemical Physics*, vol. 15, no. 40, pp. 17287–17294, 2013.

[100] C. Arbizzani, M. Biso, D. Cericola, M. Lazzari, F. Soavi, and M. Mastragostino, "Safe, high-energy supercapacitors based on solvent-free ionic liquid electrolytes", *Journal of Power Sources*, vol. 185, no. 2, pp. 1575–1579, 2008.

[101] S. Pohlmann, T. Olyschläger, P. Goodrich, J. A. Vicente, J. Jacquemin, and A. Balducci, "Azepanium-based ionic liquids as green electrolytes for high voltage supercapacitors", *Journal of Power Sources*, vol. 273, pp. 931–936, 2015.

[102] A. Balducci, W. A. Henderson, M. Mastragostino, S. Passerini, P. Simon, and F. Soavi, "Cycling stability of a hybrid activated carbon//poly (3-methylthiophene) supercapacitor with N-butyl-N-methylpyrrolidinium bis(trifluoromethanesulfonyl)imide ionic liquid as electrolyte", *Electrochimica Acta*, vol. 50, no. 11, pp. 2233–2237, 2005.

[103] A. Brandt and A. Balducci, "Theoretical and practical energy limitations of organic and ionic liquid-based electrolytes for high voltage electrochemical double layer capacitors", *Journal of Power Sources*, vol. 250, pp. 343–351, 2014.

[104] F. Soavi, C. Arbizzani, and M. Mastragostino, "Leakage currents and self-discharge of ionic liquid-based supercapacitors", *Journal of Applied Electrochemistry*, vol. 44, no. 4, pp. 491–496, 2014.

[105] A. Balducci, R. Dugas, P.-L. Taberna, P. Simon, D. Plee, M. Mastragostino, and S. Passerini, "High temperature carbon–carbon supercapacitor using ionic liquid as electrolyte", *Journal of Power Sources*, vol. 165, no. 2, pp. 922–927, 2007.

[106] J. Chmiola, C. Largeot, P.-L. Taberna, P. Simon, and Y. Gogotsi, "Desolvation of ions in subnanometer pores and its effect on capacitance and

double-layer theory", *Angewandte Chemie International Edition*, vol. 47, no. 18, pp. 3392–3395, 2008.

[107] B. Wilson, R. Georgiadis, and J. E. Bartmess, "Enthalpies of solvation of ions. Aliphatic carboxylic acids: Steric hindrance to solvation", *Journal of the American Chemical Society*, vol. 113, no. 5, pp. 1762–1766, 1991.

[108] P. J. Beach, "Heats of Solvation of Organic Liquids in Room Temperature Ionic Liquids", Master's thesis, University of Tennessee - Knoxville, 2008.

[109] S. Pohlmann, T. Olyschläger, P. Goodrich, J. A. Vicente, J. Jacquemin, and A. Balducci, "Mixtures of azepanium based ionic liquids and propylene carbonate as high voltage electrolytes for supercapacitors", *Electrochimica Acta*, vol. 153, pp. 426–432, 2015.

[110] H. Wang and L. Pilon, "Reply to comments on "Intrinsic limitations of impedance measurements in determining electric double layer capacitances" by H. Wang and L. Pilon [Electrochimica Acta 63 (2012) 55]", *Electrochimica Acta*, vol. 76, pp. 529–531, 2012.

[111] A. Burke and M. Miller, "Testing of electrochemical capacitors: Capacitance, resistance, energy density, and power capability", *Electrochimica Acta*, vol. 55, no. 25, pp. 7538–7548, 2010.

[112] S. Zhao, F. Wu, L. Yang, L. Gao, and A. F. Burke, "A measurement method for determination of DC internal resistance of batteries and supercapacitors", *Electrochemistry Communications*, vol. 12, no. 2, pp. 242–245, 2010.

[113] M. D. Stoller and R. S. Ruoff, "Best practice methods for determining an electrode material's performance for ultracapacitors", *Energy & Environmental Science*, vol. 3, no. 9, pp. 1294–1301, 2010.

[114] S. R. C. Vivekchand, C. S. Rout, K. S. Subrahmanyam, A. Govindaraj, and C. N. R. Rao, "Graphene-based electrochemical supercapacitors", *Journal of Chemical Sciences*, vol. 120, no. 1, pp. 9–13, 2008.

[115] V. L. Martins, A. J. R. Rennie, N. Sanchez-Ramirez, R. M. Torresi, and P. J. Hall, "Improved performance of ionic liquid supercapacitors by using tetracyanoborate anions", *ChemElectroChem*, vol. 5, no. 4, pp. 598–604, 2018.

[116] A. J. R. Rennie, V. L. Martins, R. M. Smith, and P. J. Hall, "Influence of particle size distribution on the performance of ionic liquid-based electrochemical double layer capacitors", *Scientific Reports*, vol. 6, pp. 22062, 2016.

[117] C. Kim, "Electrochemical characterization of electrospun activated carbon nanofibres as an electrode in supercapacitors", *Journal of Power Sources*, vol. 142, no. 1-2, pp. 382–388, 2005.

[118] Y. Gao, Y. S. Zhou, M. Qian, X. N. He, J. Redepenning, P. Goodman, H. M. Li, L. Jiang, and Y. F. Lu, "Chemical activation of carbon nano-onions for high-rate supercapacitor electrodes", *Carbon*, vol. 51, pp. 52–58, 2013.

[119] H. Wang and L. Pilon, "Physical interpretation of cyclic voltammetry for measuring electric double layer capacitances", *Electrochimica Acta*, vol. 64, pp. 130–139, 2012.

[120] E. Frackowiak, G. Lota, and J. Pernak, "Room-temperature phosphonium ionic liquids for supercapacitor application", *Applied Physics Letters*, vol. 86, no. 16, pp. 164104, 2005.

[121] D. Wei and T. W. Ng, "Application of novel room temperature ionic liquids in flexible supercapacitors", *Electrochemistry Communications*, vol. 11, no. 10, pp. 1996–1999, 2009.

[122] G. Xiong, A. Kundu, and T. S. Fisher, *Thermal Effects in Supercapacitors*, Springer, 2015.

[123] S. Pohlmann, R.-S. Kühnel, T. A. Centeno, and A. Balducci, "The influence of anion–cation combinations on the physicochemical properties of advanced electrolytes for supercapacitors and the capacitance of activated carbons", *ChemElectroChem*, vol. 1, no. 8, pp. 1301–1311, 2014.

[124] D. R. MacFarlane, M. Forsyth, E. I. Izgorodina, A. P. Abbott, G. Annat, and K. Fraser, "On the concept of ionicity in ionic liquids", *Physical Chemistry Chemical Physics*, vol. 11, no. 25, pp. 4962–4967, 2009.

[125] K. Hayamizu, Y. Aihara, S. Arai, and C. G. Martinez, "Pulse-gradient spin-echo 1H, 7Li, and 19F NMR diffusion and ionic conductivity measurements of 14 organic electrolytes containing $LiN(SO_2CF_3)_2$", *The Journal of Physical Chemistry B*, vol. 103, no. 3, pp. 519–524, 1999.

[126] K. Dixler and W. Kwok, "Active and passive cooling for an energy storage module", U.S. Patent App. 13/710,573 (2014).

[127] A. Brandt, C. Ramirez-Castro, M. Anouti, and A. Balducci, "An investigation about the use of mixtures of sulfonium-based ionic liquids and propylene carbonate as electrolytes for supercapacitors", *Journal of Materials Chemistry A*, vol. 1, no. 40, pp. 12669–12678, 2013.

[128] M. Hahn, A. Würsig, R. Gallay, P. Novák, and R. Kötz, "Gas evolution in activated carbon/propylene carbonate based double-layer capacitors", *Electrochemistry Communications*, vol. 7, no. 9, pp. 925–930, 2005.

[129] K. Xu, S. P. Ding, and T. R. Jow, "Toward reliable values of electrochemical stability limits for electrolytes", *Journal of The Electrochemical Society*, vol. 146, no. 11, pp. 4172, 1999.

[130] M. Morita, M. Goto, and Y. Matsuda, "Ethylene carbonate-based organic electrolytes for electric double layer capacitors", *Journal of Applied Electrochemistry*, vol. 22, no. 10, pp. 901–908, 1992.

[131] M. Ishikawa, M. Ihara, M. Morita, and Y. Matsuda, "Electric double layer capacitors with new gel electrolytes", *Electrochimica Acta*, vol. 40, no. 13-14, pp. 2217–2222, 1995.

[132] C. Yin, X. Liu, J. Wei, R. Tan, J. Zhou, M. Ouyang, H. Wang, S. J. Cooper, B. Wu, C. George, and Q. Wang, "All-in-Gel design for supercapacitors towards solid-state energy devices with thermal and mechanical compliance", *Journal of Materials Chemistry A*, vol. 7, no. 15, pp. 8826–8831, 2019.

[133] Y. Cheng, H. Zhang, S. Lu, C. V. Varanasi, and J. Liu, "Flexible asymmetric supercapacitors with high energy and high power density in aqueous electrolytes", *Nanoscale*, vol. 5, no. 3, pp. 1067–1073, 2013.

[134] R. Payne and I. E. Theodorou, "Dielectric properties and relaxation in ethylene carbonate and propylene carbonate", *The Journal of Physical Chemistry*, vol. 76, no. 20, pp. 2892–2900, 1972.

[135] J. Barthel, R. Neueder, and H. Roch, "Density, relative permittivity, and viscosity of propylene carbonate + dimethoxyethane mixtures from 25 °C to 125 °C", *Journal of Chemical & Engineering Data*, vol. 45, no. 6, pp. 1007–1011, 2000.

[136] I. Krossing, J. M. Slattery, C. Daguenet, P. J. Dyson, A. Oleinikova, and H. Weingärtner, "Why are ionic liquids liquid? A simple explanation based on lattice and solvation energies", *Journal of the American Chemical Society*, vol. 128, no. 41, pp. 13427–13434, 2006.

[137] H. Weingärtner, P. Sasisanker, C. Daguenet, P. J. Dyson, I. Krossing, J. M. Slattery, and T. Schubert, "The dielectric response of room-temperature ionic liquids: effect of cation variation", *The Journal of Physical Chemistry B*, vol. 111, no. 18, pp. 4775–4780, 2007.

[138] M.-M. Huang, Y. Jiang, P. Sasisanker, G. W. Driver, and H. Weingaärtner, "Static relative dielectric permittivities of ionic liquids at 25 °C", *Journal of Chemical & Engineering Data*, vol. 56, no. 4, pp. 1494–1499, 2011.

[139] A. B. McEwen, S. F. McDevitt, and V. R. Koch, "Nonaqueous electrolytes for electrochemical capacitors: imidazolium cations and inorganic fluorides with organic carbonates", *Journal of The Electrochemical Society*, vol. 144, no. 4, pp. L84, 1997.

[140] K. Xu, "Nonaqueous liquid electrolytes for lithium-based rechargeable batteries", *Chemical Reviews*, vol. 104, no. 10, pp. 4303–4418, 2004.

[141] Q. Wang, P. Ping, X. Zhao, G. Chu, J. Sun, and C. Chen, "Thermal runaway caused fire and explosion of lithium ion battery", *Journal of Power Sources*, vol. 208, pp. 210–224, 2012.

[142] X. Baokou and M. Anouti, "Physical properties of a new deep eutectic solvent based on a sulfonium ionic liquid as a suitable electrolyte for electric double-layer capacitors", *The Journal of Physical Chemistry C*, vol. 119, no. 2, pp. 970–979, 2015.

[143] M. Kunze, S. Jeong, G. B. Appetecchi, M. Schönhoff, M. Winter, and S. Passerini, "Mixtures of ionic liquids for low temperature electrolytes", *Electrochimica Acta*, vol. 82, pp. 69–74, 2012.

[144] J. Black and H. A. Andreas, "Effects of charge redistribution on self-discharge of electrochemical capacitors", *Electrochimica Acta*, vol. 54, no. 13, pp. 3568–3574, 2009.

[145] G. Madabattula and S. Kumar, "Insights into charge-redistribution in double layer capacitors", *Journal of The Electrochemical Society*, vol. 165, no. 3, pp. A636–A649, 2018.

[146] T. Bhuvana, A. Kumar, A. Sood, R. H. Gerzeski, J. Hu, V. S. Bhadram, C. Narayana, and T. S. Fisher, "Contiguous petal-like carbon nanosheet outgrowths from graphite fibers by plasma cvd", *ACS Applied Materials & Interfaces*, vol. 2, no. 3, pp. 644–648, 2010.

[147] G. Xiong, K. Hembram, R. G. Reifenberger, and T. S. Fisher, "MnO_2-coated graphitic petals for supercapacitor electrodes", *Journal of Power Sources*, vol. 227, pp. 254–259, 2013.

[148] G. Xiong, C. Meng, R. G. Reifenberger, P. P. Irazoqui, and T. S. Fisher, "Graphitic petal electrodes for all-solid-state flexible supercapacitors", *Advanced Energy Materials*, vol. 4, no. 3, 2014.

[149] L. Pilon, H. Wang, and A. L. d'Entremont, "Recent advances in continuum modeling of interfacial and transport phenomena in electric double layer capacitors", *Journal of the Electrochemical Society*, vol. 162, no. 5, pp. A5158–A5178, 2015.

[150] H.-L. Girard, H. Wang, A. L. d'Entremont, and L. Pilon, "Physical interpretation of cyclic voltammetry for hybrid pseudocapacitors", *The Journal of Physical Chemistry C*, vol. 119, no. 21, pp. 11349–11361, 2015.

[151] H. Yoon, H.-J. Kim, J. J. Yoo, C.-Y. Yoo, J. H. Park, Y. A. Lee, W. K. Cho, Y.-K. Han, and D. H. Kim, "Pseudocapacitive slurry electrodes using redox-active quinone for high-performance flow capacitors: an atomic-level understanding of pore texture and capacitance enhancement", *Journal of Materials Chemistry A*, vol. 3, no. 46, pp. 23323–23332, 2015.

[152] Y. Liu, B. Weng, J. M. Razal, Q. Xu, C. Zhao, Y. Hou, S. Seyedin, R. Jalili, G. G. Wallace, and J. Chen, "High-performance flexible all-solid-state supercapacitor from large free-standing graphene-PEDOT/PSS films", *Scientific Reports*, vol. 5, pp. 17045, 2015.

[153] G. Wang, H. Wang, X. Lu, Y. Ling, M. Yu, T. Zhai, Y. Tong, and Y. Li, "Solid-state supercapacitor based on activated carbon cloths exhibits excellent rate capability", *Advanced materials*, vol. 26, no. 17, pp. 2676–2682, 2014.

[154] A. J. Bard and L. R. Faulkner, *Electrochemical Methods: Fundamentals and Applications*, John Wiley & Sons, New York, NY, 2001.

[155] A. L. d'Entremont, H.-L. Girard, H. Wang, and L. Pilon, "Electrochemical transport phenomena in hybrid pseudocapacitors under galvanostatic cycling", *Journal of the Electrochemical Society*, vol. 163, no. 2, pp. A229–A243, 2016.

[156] P. Yang, K. Liu, Q. Chen, X. Mo, Y. Zhou, S. Li, G. Feng, and J. Zhou, "Wearable thermocells based on gel electrolytes for the utilization of body heat", *Angewandte Chemie International Edition*, vol. 55, no. 39, pp. 12050–12053, 2016.

[157] A. Kundu and T. S. Fisher, "Harnessing the thermogalvanic effect of the ferro/ferricyanide redox couple in a thermally chargeable supercapacitor", *Electrochimica Acta*, 2018.

[158] K. K. Lian, C. Li, R. H. Jung, and J. G. Kincs, "Electrochemical cell having symmetric inorganic electrodes", Dec. 24 1996, US Patent 5,587,872.

[159] S. T. Senthilkumar, R. K. Selvan, and J. S. Melo, "Redox additive/active electrolytes: a novel approach to enhance the performance of supercapacitors", *Journal of Materials Chemistry A*, vol. 1, no. 40, pp. 12386–12394, 2013.

[160] M. Elimelech, W. H. Chen, and J. J. Waypa, "Measuring the zeta (electrokinetic) potential of reverse osmosis membranes by a streaming potential analyzer", *Desalination*, vol. 95, no. 3, pp. 269–286, 1994.

[161] Y. Tian, J. Yan, R. Xue, and B. Yi, "Capacitive properties of activated carbon in $K_4Fe\ (CN)_6$", *Journal of The Electrochemical Society*, vol. 158, no. 7, pp. A818–A821, 2011.

[162] J. Lee, S. Choudhury, D. Weingarth, D. Kim, and V. Presser, "High performance hybrid energy storage with potassium ferricyanide redox electrolyte", *ACS Applied Materials & Interfaces*, vol. 8, no. 36, pp. 23676–23687, 2016.

[163] B. Korth, T. Maskow, C. Picioreanu, and F. Harnisch, "The microbial electrochemical peltier heat: an energetic burden and engineering chance for primary microbial electrochemical technologies", *Energy & Environmental Science*, vol. 9, no. 8, pp. 2539–2544, 2016.

[164] P. Boudeville and A. Tallec, "Electrochemistry and calorimetry coupling: IV. determination of electrochemical peltier heat", *Thermochimica Acta*, vol. 126, pp. 221–234, 1988.

[165] Y. Maeda and T. Kumagai, "Electrochemical peltier heat in the polypyrrole-electrolyte system", *Thermochimica Acta*, vol. 267, pp. 139–148, 1995.

[166] S. Murakami, S. Kato, and J. Zeng, "Combined simulation of airflow, radiation and moisture transport for heat release from a human body", *Building and Environment*, vol. 35, no. 6, pp. 489–500, 2000.